A study of the relaxation dynamics of local vibrational modes associated with hydrogen in diamond

by

Daniel John Luke Coxon

A thesis submitted in partial fulfilment of the requirements for the
degree of
Doctor of Philosophy in Physics

University of Warwick, Department of Physics

January 2022


Ultrafast
Diamond
Time
Infrared
Hydrogen
Transmission
Defect
Vibration
Transient
Spectroscopy
Spectrum
Lifetime
Pump
Bend
Absorption
Stretch
Natural
Synthetic
Probe
Quantification
Wavenumber
Ground state
Excited state
Phonon
Argyle
Decay
Pulse
CVD
Photon
Model
FTIR
Emission
Laser
Symmetry
Population
Acoustic
Voigt
Nitrogen
Transition
Optical
Resolution
Visible
Time-resolved
Cryogenic
Concentration
Picosecond
Time constant
Dynamics
Feature
Ultraviolet
TVAS
UV/Vis

Table of Contents

Acknowledgements

I do not think I could possibly thank all the people who have helped me during the 5 years of my Masters and subsequent PhD (to say nothing of the 4 years of undergraduate that preceded it), but I will do my best.

I am eternally grateful to my supervisors, Vasilios Stavros, James Lloyd-Hughes and Mark Newton, for their advice and encouragement during my PhD, particularly early on when I was struggling with it. I thank De Beers and the EPSRC for providing funding, and the DTC Research Centre for their collaboration on my project. I thank Ed Greenough and Mick Staniforth for training me up on the ultrafast setup that I used, and the latter especially for supporting me both academically and with regards to my mental health. I thank Ben Breeze for training me up on the steady-state measurements.

Many thanks to the Stavros Group for their excellent camaraderie – in particular my laser buddy Jack for teaching me to always let the dog see the rabbit, Matt for his fantastic renditions of classic songs, Emily for her ‘very dry’ sense of humour and Konstantina for being absolutely lovely despite randomly hating on Moana. I thank the Centre for Doctoral Training in Diamond Science and Technology, particularly Cohort 3 who I will always feel I share a bond with.

I thank the people of Warwick Latin and Ballroom for providing me a space to learn to dance, something which now gives me great joy even in the most difficult moments and helped me massively to get through my PhD. I am particularly thankful to Rosie, Ella, Deannah, Harry, Emma, Gemma, Matt, Peter, Chris, Becca, Abi, Calvin and Sophie for their friendship, encouragement and countless fun at all our competitions, to our coach Mark for believing that we can be a threat, and to Lizz for being the best dance partner I could ever wish for.

I am deeply grateful for the support of the people at Emmanuel Church, Leamington Spa, for their hospitality and kindness to me over the years I spent at Warwick. I want to particularly

mention Pete and Pauline Dillon, who took a special interest in me from day one and always looked out for me, and the Alexander family for many a fun time playing board games. I thank my therapist, Tracey, for helping me to stay motivated throughout the last year of writing up.

I thank Ethan, Danny, Josh, Jonathan, James, Miriam, Raymond and Stephen for being the best group of friends throughout my PhD. Thank you all for supporting me in your own ways, Ethan for being the other half of My Chemical Bromance, Danny for our trip to Denmark and for teaching me to handle the defence (of my thesis – hopefully), Josh for always saving my things and putting them in the Whoopsie Chest, Jonathan for our summer trips to the cricket which have now become an institution, James for our regular lunches and for bearing the diamond PhD burden with me, Miriam for fun times spent baking the Splattenberg and listening to your poetry, Raymond for being RAYMOND, and Stephen who managed to maintain my friendship despite breaking my favourite mug, me constantly singing his theme song and our many debates over whether food really is just food (it's not).

I thank my family for their constant support throughout my education. Thank you especially to my parents, Paul and Sue, for always believing in me and encouraging me to pursue studies beyond my age, for sacrificing so much to educate myself and my siblings, and for bringing me up in my faith. I dedicate this thesis to you, as I know it would not have been possible without all that you have done for me. I thank my grandparents, George and Alma, and Alastair and June, two of whom sadly passed away during my PhD, for always believing in me. I thank my older brother Joshua for being my best friend ever since I was born, and always being someone who I know I can reach out to (sorry for occasionally waking you up when you've been working nights at the hospital). Thanks to my younger siblings Joel, Esther and Micah for also being incredibly fun – I always have a great time when I am with you guys.

Most of all, I thank God for His mercies that are new every morning. I know that it is Him who has graciously given me the necessary skills, time and work ethic to complete this PhD.

Declarations

I declare that everything detailed in this thesis is my own work, unless explicitly stated otherwise. Additionally, I declare that all the data presented in Chapters 3 through 5 was collected between October 2017 and November 2020, under the supervision of Professor Vasilios Stavros, Dr James Lloyd-Hughes and Professor Mark Newton. None of this research has been submitted in any form to another academic institution. However, some segments have been published either as a research paper, a conference presentation. Each of these instances are given below:

Research paper

- D. J. L. Coxon, M. Staniforth, B. G. Breeze, S. E. Greenough, J. P. Goss, M. Monti, J. Lloyd-Hughes, V. G. Stavros, M. E. Newton, *J. Phys. Chem. Lett.* **2020**, *11*, 6677–6683.

Conference presentations

- D. J. L. Coxon, M. Staniforth, B. G. Breeze, S. E. Greenough, J. Lloyd-Hughes, V. G. Stavros, M. E. Newton, "Are diamonds forever? Time-resolved experiments on hydrogen defects", 2018, poster presentation at the 69th Diamond Conference, Coventry, UK.
- D. J. L. Coxon, M. Staniforth, B. G. Breeze, S. E. Greenough, J. P. Goss, J. Lloyd-Hughes, V. G. Stavros, M. E. Newton, "Relaxation dynamics of local vibrational modes associated with hydrogen in diamond", 2019, poster presentation at the 70th Diamond Conference, Coventry, UK.

- D. J. L. Coxon, M. Staniforth, B. G. Breeze, S. E. Greenough, J. P. Goss, M. Monti, J. Lloyd-Hughes, V. G. Stavros, M. E. Newton, “An ultrafast shakedown reveals the energy landscape, relaxation dynamics and concentration of N_3VH^0 defects in diamond”, 2020, oral presentation at the Spectroscopy and Dynamics Group Annual Meeting, Coventry, UK.
- D. J. L. Coxon, M. Staniforth, B. G. Breeze, J. Lloyd-Hughes, V. G. Stavros, M. E. Newton, “Whodunnit? Towards solving the puzzle of the 3237 cm^{-1} feature in diamond”, 2020, poster presentation at the Spectroscopy and Dynamics Group Annual Meeting, Coventry, UK.
- D. J. L. Coxon, M. Staniforth, B. G. Breeze, J. Lloyd-Hughes, V. G. Stavros, M. E. Newton, “An ultrafast shakedown reveals the energy landscape, relaxation dynamics and concentration of hydrogen related modes in diamond”, 2020, poster presentation at the Diamond Science and Technology Poster Session, held online.
- D. J. L. Coxon, M. Staniforth, B. G. Breeze, J. Lloyd-Hughes, V. G. Stavros, M. E. Newton, “An ultrafast, ultraviolet shakedown: probing the effect of electronic excitation on hydrogen-related modes in type IaB diamond”, 2021, oral presentation at the 71st Diamond Conference, held online.

Abstract

Atomic-scale defects can control the exploitable optoelectronic performance of crystalline materials, and several point defects in diamond are emerging functional components for a range of quantum technologies. Nitrogen and hydrogen are common impurities incorporated into diamond, and there is a family of defects that includes both. The N_3VH^0 defect is a lattice vacancy where three nearest neighbor carbon atoms are replaced with nitrogen atoms and a hydrogen is bonded to the remaining carbon. It is regularly observed in natural and high-temperature annealed synthetic diamond and gives rise to prominent absorption features in the mid-infrared, the strongest of these being its C–H stretch mode at 3107 cm^{-1}. Often, it is observed alongside another feature at 3237 cm^{-1}. This feature is presently unidentified, but speculated to belong to an N–H stretch. Here, we combine time- and spectrally resolved infrared absorption spectroscopy to yield unprecedented insight into the vibrational dynamics of both of these defects, following both infrared and ultraviolet excitation of the C–H stretch. In doing so, we gain fundamental information about the energies of quantized vibrational states and corroborate our results with theory. We map out, for the first time, energy relaxation pathways, which include multiphonon relaxation processes and, in the case of N_3VH^0, anharmonic coupling to the bend modes. These advances provide a new route to probe and quantify atomic-scale defects in diamond.

1 Introduction

1.1 Introduction to diamond

1.1.1 Diamond in history

Throughout history, diamond has been revered as a precious stone of great value. Many translations of the Book of Exodus refer to diamond as one of the twelve gemstones set in the priestly breastplate [**1**]. In Chapter XI of the Arthra-Sastra, details are given regarding both the source and value of diamonds, in addition to regulations involved in the diamond trade [**2**]. The word 'diamond' has its root in the Greek 'ἀδάμας' or 'adamas', meaning 'invincible', owing to its extreme hardness. Pliny the Elder describes diamond in glowing terms and refers to its two common uses – as an object of beauty and as a tool for cutting and engraving [**3**].

1.1.2 Diamond in science

Diamond is known to be one of the allotropes of carbon. It exists as a giant covalent lattice, one unit cell of which is shown in Figure 1.1. Each carbon atom is sp^3 bonded to four nearest neighbours, creating a rigid tetrahedral structure. The diamond lattice is based on a face-centred cubic (fcc) lattice arrangement, with an additional two-atom basis filling half of the tetrahedral holes. This regular repeating pattern of strong, short covalent bonds is what gives rise to many of the incredible properties of diamond, such as its extreme hardness (10 on the Mohs scale), high thermal conductivity (up to 2200 $Wm^{-1}K^{-1}$), high refractive index (~2.4) and high optical transparency.

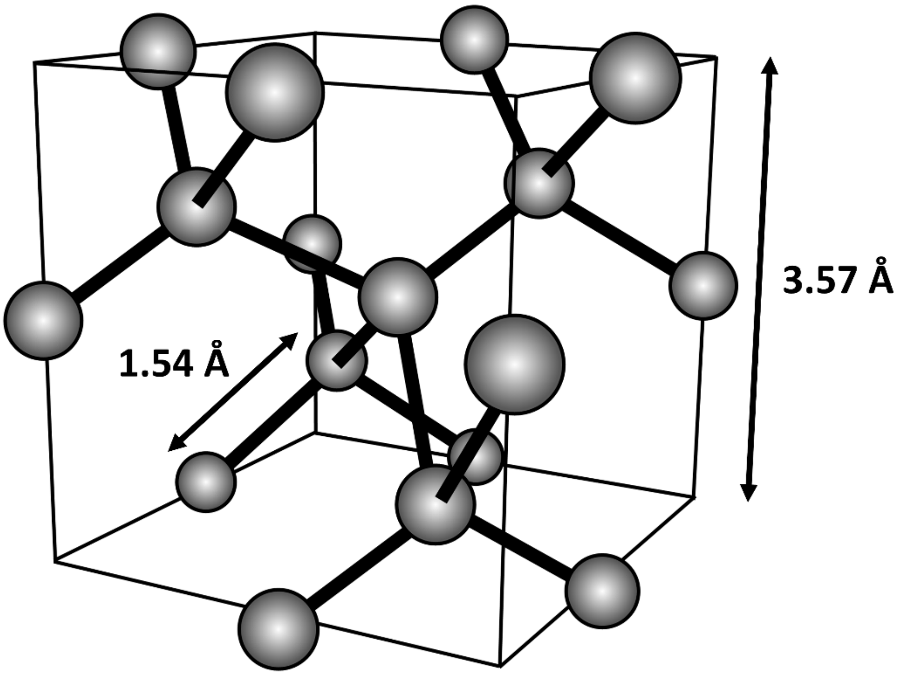

Figure 1.1 One unit cell of the repeating tetrahedral lattice structure of diamond. Each grey circle represents a single carbon atom.

1.2 Formation of diamond

Energetically, diamond is a less stable allotrope than graphite at room temperature and pressure. Conversion between the two structures requires a significant amount of energy. The conditions required for diamond formation typically follow the Simon-Berman line, shown in Figure 1.2, which details the relationship between the pressure, P, in kilobars and the temperature, T, in Kelvin required for equilibrium between diamond and graphite:

$$P(\text{kbar}) = 7.1 + 0.027T(\text{K}) \tag{1.1}$$

This equation was originally extrapolated from thermodynamic calculations, based on the heats of formation of both allotropes, using data recorded at temperatures of up to 1200 K [**4**]. Subsequent equilibrium experiments, using a variety of apparatuses and conditions to form diamond from graphite using metal solvent catalysts, and to directly graphitise diamond without the presence of a catalyst, supported the conclusions from theory [**5**].

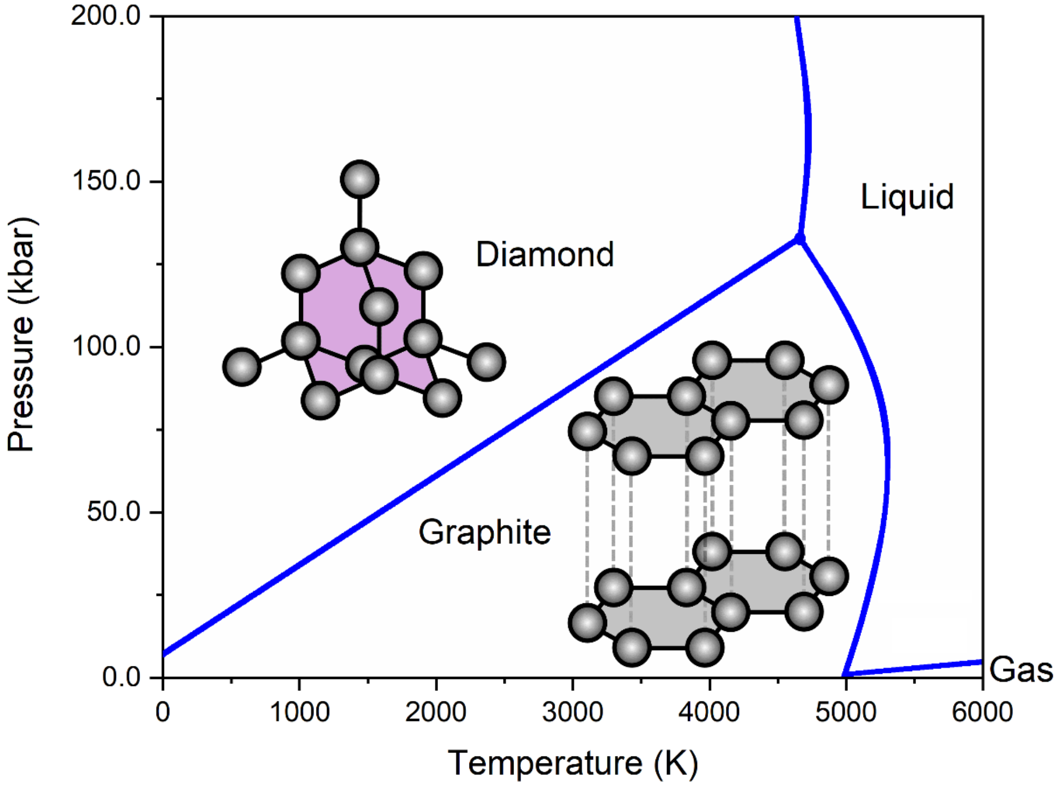

Figure 1.2 The phase diagram of carbon, including the Simon-Berman line and showing the conditions required for the formation of diamond from graphite. If the temperature is too high, liquid or gaseous carbon is formed instead.

Following the Simon-Berman line, diamond may be produced under conditions of high pressure and temperature. In the following sections, 1.2.1 through 1.2.3, we describe the formation of diamond in nature and through the most common synthetic production methods – high pressure, high temperature (HPHT) synthesis and chemical vapour deposition (CVD).

1.2.1 Natural diamond

The majority of the Earth's naturally occurring diamonds are formed deep in the subcratonic regions of the lithospheric mantle, at boundary regions near the asthenosphere [**6-7**]. When the lithosphere and the asthenosphere are at roughly the same depth, roughly 200 km, the cooler temperature of the former allows for a lower pressure requirement for diamond formation, according to the Simon-Berman line. Thus, there is a window in the deep lithosphere where diamond production becomes an energetically favourable process.

Diamond crystals form in melts that are found in this window and precipitate out on substrate rocks. Common substrates for diamond deposition include peridotites, eclogites and websterites [**8**]. Traditional models for diamond formation within the lithospheric mantle invoke either carbonate reduction or methane oxidation, but more recent work suggests that they may form through isochemical cooling of H_2O-rich Carbon-Hydrogen-Oxygen fluids [**9**]. Once formed, diamonds are subsequently taken up towards the Earth's surface through kimberlite pipes [**8,10-11**]. A significantly smaller proportion of natural diamonds are produced below the lithosphere in subduction zones underneath oceanic crust [**12**]. Figure 1.3 shows the regions of the upper mantle where diamond formation can occur.

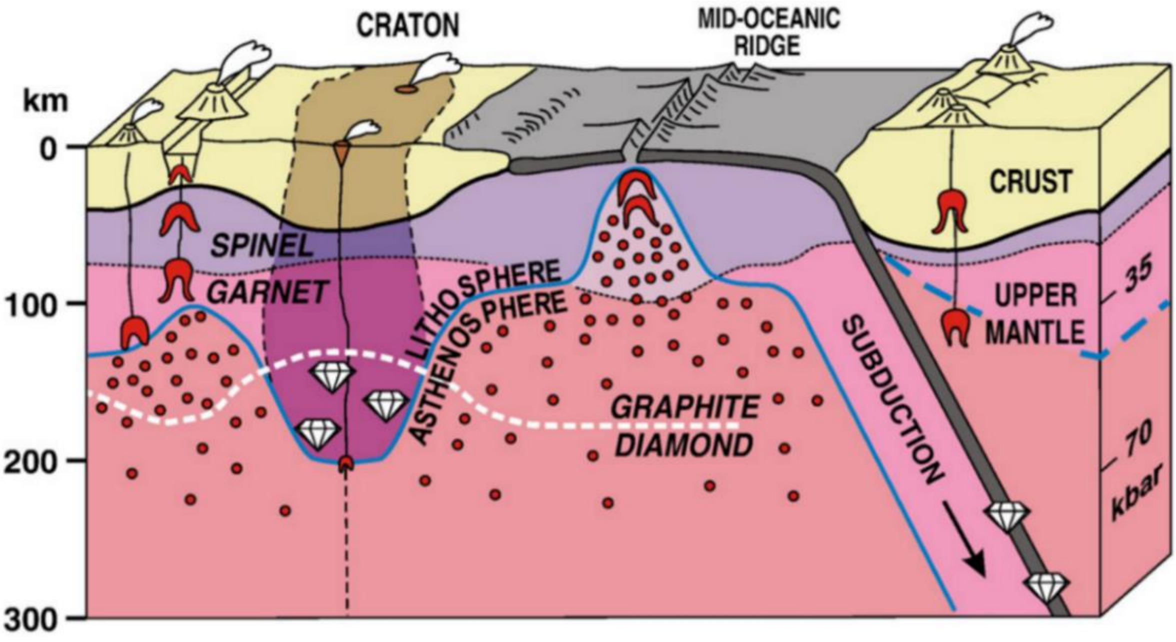

Figure 1.3 Schematic showing a section of the crust and upper mantle of the Earth, including depth below the surface, and pressure (kbar). Regions where diamond formation is energetically favourable are denoted. Diamond is formed in two regions: in the window deep in the subcratonic lithosphere, and in deep subduction zones underneath oceanic crust. Reproduced from [**7**].

Diamond inclusions have also been found to occur in carbon-rich meteorites, known as ureilites, that have crashed into the Earth [**13**]. The origin of these diamonds is not explicitly known – however, there are several suggested explanations for their formation: (1) through energy generated by the impact of a collision [**14**]; (2) through exposure to gases in the solar nebula that are rich in carbon [**15**]; and (3) due to high internal pressure inside the ureilites themselves, which allows diamond formation to become energetically favourable [**16**].

1.2.2 High pressure, high temperature synthesis of diamond

HPHT synthesis aims to replicate the conditions required for the natural formation of diamond [**17-19**]. Carbon-rich sources such as graphite are dissolved in a molten metal solvent, typically a transition metal alloy, and heated at a temperature exceeding 1600 K inside a reaction cell, subjected by a belt [**19**], cubic [**20**] or split-sphere [**21**] press to pressures above 50 kbar. Under these conditions, the carbon-rich sources can spontaneously precipitate out as diamond, creating small crystals which begin to grow over time. Alternatively, the reaction cell may be set up with a temperature gradient. In this case, the upper section of the reaction cell remains at a high temperature, while the lower section exists at a cooler temperature and contains individual diamond seed crystals. The reduction in temperature induces precipitation onto and subsequent growth of the diamond seed crystals. A schematic of the setup required for HPHT diamond synthesis is shown in Figure 1.4.

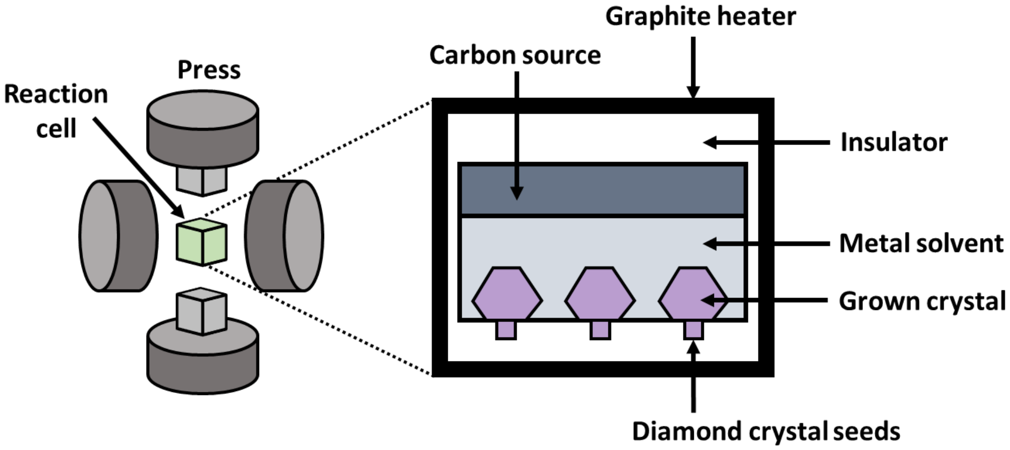

Figure 1.4 Schematic representation of a HPHT diamond press, using the temperature gradient method to grow diamond crystals.

Since nitrogen gas readily enters the presses, the diamonds produced by HPHT synthesis are often yellow in colour. Recent advances in impurity control, such as the introduction of nitrogen-getters (aluminium or titanium) into the synthesis mixture, has enabled the production of colourless HPHT diamonds [**22**]. HPHT processes can also be used to anneal both natural diamonds and those produced by CVD synthesis [**23-24**].

1.2.3 Chemical vapour deposition synthesis of diamond

CVD growth of diamond is achieved by exposure to free radicals. The most common of these are the hydrogen radical, $H^\bullet$, and the methyl radical, $^\bullet CH_3$, which form the basis of the mechanism for CVD growth – abstraction of surface atoms by $H^\bullet$ and subsequent addition of $^\bullet CH_3$ which builds up layers of diamond [**25-26**], as demonstrated in Figure 1.5.

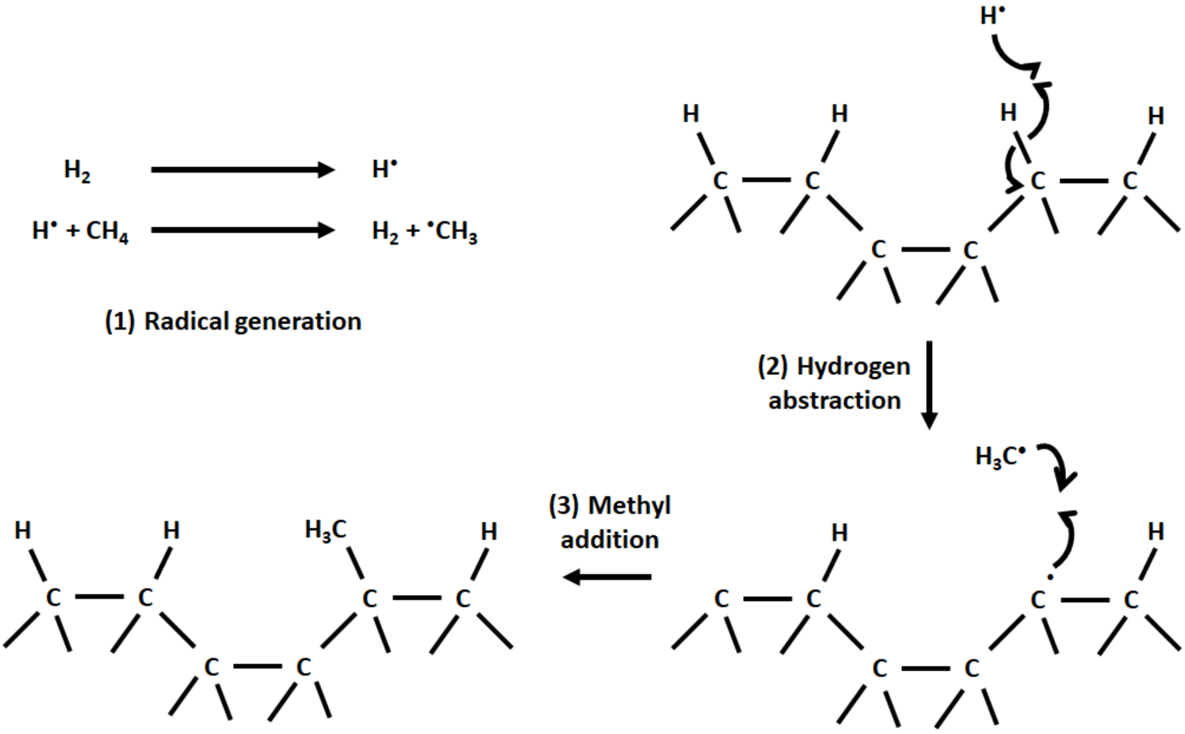

Figure 1.5 Mechanism for growth of diamond by CVD. After radicals are generated, hydrogen abstraction and methyl addition allow for the growth of sp^3 diamond.

Inside a CVD reactor, the synthesis gas mixture is passed through onto a non-diamond substrate seeded with diamond crystals (heteroepitaxial growth) [**27**], or a pre-existing diamond film (homoepitaxial growth) [**28**]. Radicals are generated through thermal activation of the synthesis gas mixture, which may be achieved in different ways depending on the type of reactor. A hot filament CVD (HFCVD) reactor creates a high temperature environment for radical formation [**27**], whilst a microwave plasma CVD (MWCVD) reactor creates a plasma above the substrate surface by microwave irradiation [**29**]. The latter method converts a higher proportion (~30%) of the synthesis gas into $H^\bullet$ radicals. Figure 1.6 shows simplified diagrams of these two reactors, which are those most commonly used for growth of diamond by CVD.

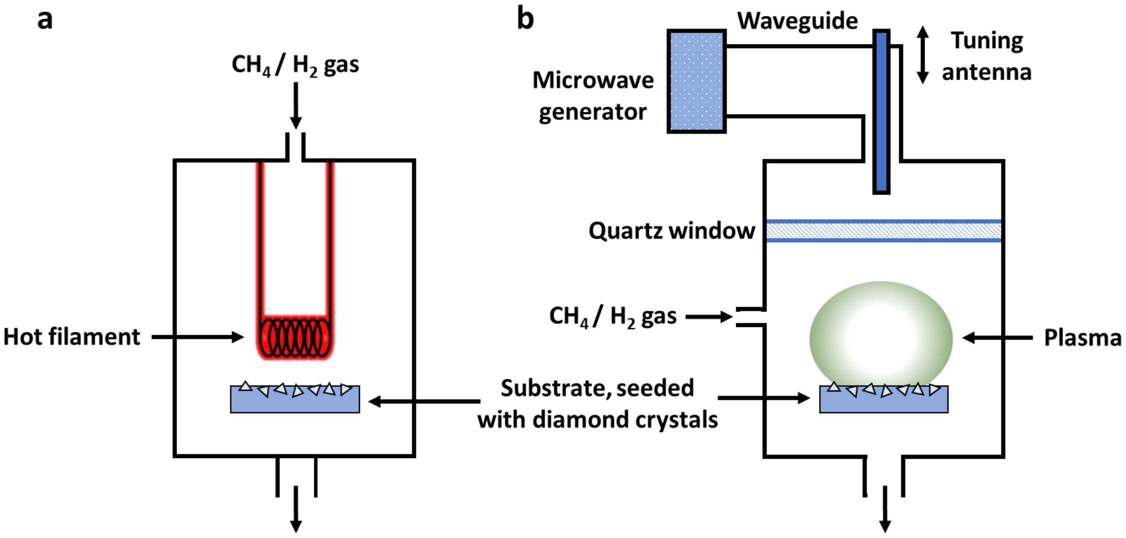

Figure 1.6 Schematic representation of **a,** a HFCVD reactor and **b,** a MWCVD reactor.

The CVD synthesis gas is normally a mixture of 1-5% methane in hydrogen, though other hydrocarbon gases may be used [**30**]. The addition of other gases such as argon [**31**], nitrogen [**32-34**] and oxygen [**35-36**] has been shown to improve either the growth rate or the overall quality of the diamonds produced. However, a high content of hydrogen is almost always required for the formation of the $H^\bullet$ and $^\bullet CH_3$ radical species required for deposition. $H^\bullet$ radicals are also required for the termination of free dangling bonds in the growing diamond to discourage the formation of sp^2 graphitic carbon, and the etching of any sp^2 carbon that does form during growth. $H^\bullet$ thus stabilises the diamond surface, ensuring that it remains sp^3 coordinated and encouraging growth of sp^3 carbon only.

Growth of diamond by CVD can be advantageous over HPHT synthesis. Due to the presence of free radicals, moderate temperatures and significantly lower pressures can be used to form diamond, in regions where graphite would normally be the energetically favourable allotrope [**26**]. Most CVD syntheses use sub-atmospheric pressures, and substrate temperatures in the range of 1000-1400 K. Additionally, being able to control the synthesis gas mixture offers an opportunity to directly influence which impurities are doped into the diamond during its growth. CVD has been used to grow a wide variety of diamonds, ranging from single crystal [**37**] to polycrystalline diamond [**38**], and from high purity, electronic-grade diamond [**39**] to quantum-grade diamond doped with specific defects [**40**]. CVD diamond can also be annealed, either by HPHT or low pressure, high temperature (LPHT) treatment, to alter its optoelectronic properties and defect composition [**23**].

CVD synthesis of diamond does have its shortcomings. In particular, the presence of hydrogen in the synthesis gas mixture often results in the incorporation of hydrogen defects in the diamonds [**41**]. Additionally, though the presence of nitrogen does dramatically increase the growth rate of CVD diamond, it also reduces its overall quality – a higher growth rate also encouraging the incorporation of sp^2 carbon during growth and producing a brown colour [**42**]. When diamond growth is heteroepitaxial, the seed crystals grow into one another, producing polycrystalline diamond (PCD) unless the substrate lattice parameter matches that of diamond, in which case oriented, regular diamond growth is possible. When growth is homoepitaxial, single crystal (SC) diamond may be produced. However the initial growth matter on the substrate edges is irregular and polycrystalline and may have to be cut away from the deposited matter. For the formation of high purity SC diamond, long growth times are typically required.

1.3 Defects in diamond

During the formation and subsequent treatment of both natural and synthetic diamond, defects become incorporated into the lattice. All defects are classified as either intrinsic or extrinsic.

Intrinsic defects occur due to errors in the diamond lattice itself. The simplest example of an intrinsic defect is the vacancy, V, shown in Figure 1.7a, which results from the complete absence of a carbon atom from the lattice [**43**], leaving its four nearest neighbour atoms with dangling bonds. Vacancies can exist in different charge states, and in some cases aggregate together, forming vacancy clusters [**44**]. Another way of altering the diamond lattice structure is by the presence of interstitial sites, where a carbon atom sits outside its normal arrangement. The simplest observed example is the split-interstitial [**45**], shown in Figure 1.7b. Like vacancies, interstitials may also aggregate to form more complex defects [**46**]. More complex intrinsic defects observed in diamond are dislocations [**47**], which are caused by a slip in one plane of the diamond lattice, and platelets [**48**], which are extended planar defects that are thin and flat in their appearance.

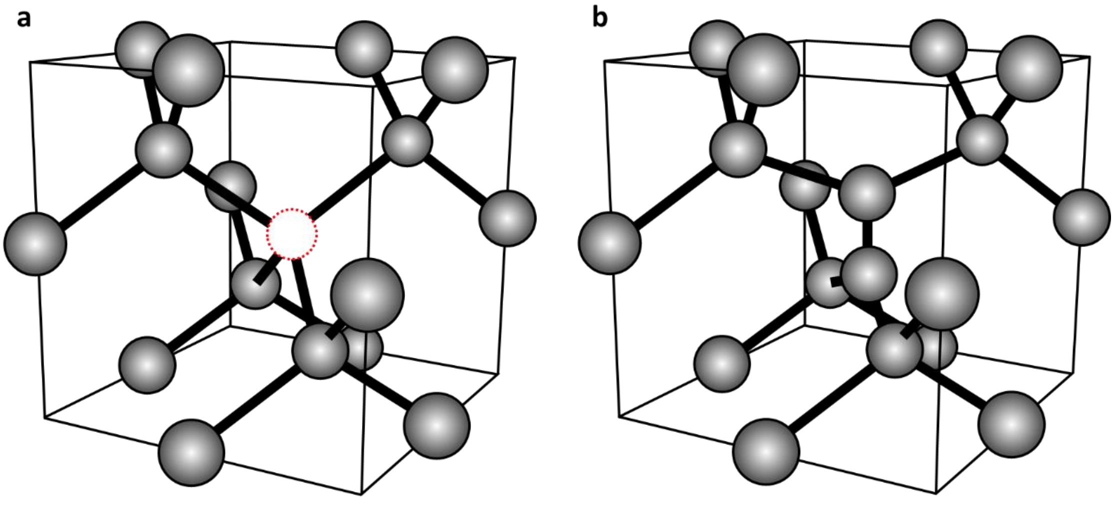

Figure 1.7 A unit cell of the diamond lattice showing **a,** the vacancy **b,** the split-interstitial.

Extrinsic defects appear due to the presence of impurity atoms in diamond. In natural diamond, impurities are omnipresent and can vary from single point defects to larger mineral inclusions [**7,49**]. In the production of synthetic diamond, it is possible to heavily control and limit the presence of defects [**50**]. Impurities can also be deliberately introduced by doping the synthesis mixture [**51-52**]. Defects may also be produced in synthetic diamond by post-processing of the diamond through electron irradiation [**53**], ion implantation [**54**] or laser writing [**55**]. Furthermore, high temperature annealing of diamond may be used to induce the formation of more complex defect sites [**23-24**].

The most common impurities in diamond are boron and nitrogen. Due to their similar size to carbon, they can directly replace an atom in the lattice structure, creating substitutional boron, (B_S) [**56**], or nitrogen, (N_S) [**57**]. More complex defects may form through interaction of multiple defect centres. For example, the migration of a nitrogen atom to a vacancy site in diamond generates a nitrogen-vacancy (NV) centre [**58**]. Impurity atoms that are too large to directly replace a carbon atom usually exist alongside a vacancy, such as the silicon-vacancy centre (SiV) [**59**].

The presence of defects significantly alters the optoelectronic properties of diamond, which is most clearly displayed in the diamond colour that manifests when there is a significant population of a specific defect centre [**60-61**]. Defects produce optical absorption of visible light and thus manifest a colour from reflected visible light. Figure 1.8 demonstrates some common defects in diamond and their associated colours in diamonds where they are the dominant defect. Another example of the change induced by defects is the p-type electrical conductivity exhibited by boron-doped diamond, which acts as a charge acceptor [**56**].

For the work in this thesis, the most important impurities to consider are those associated with nitrogen and hydrogen, which are elaborated upon in Sections 1.3.1 and 1.3.2.

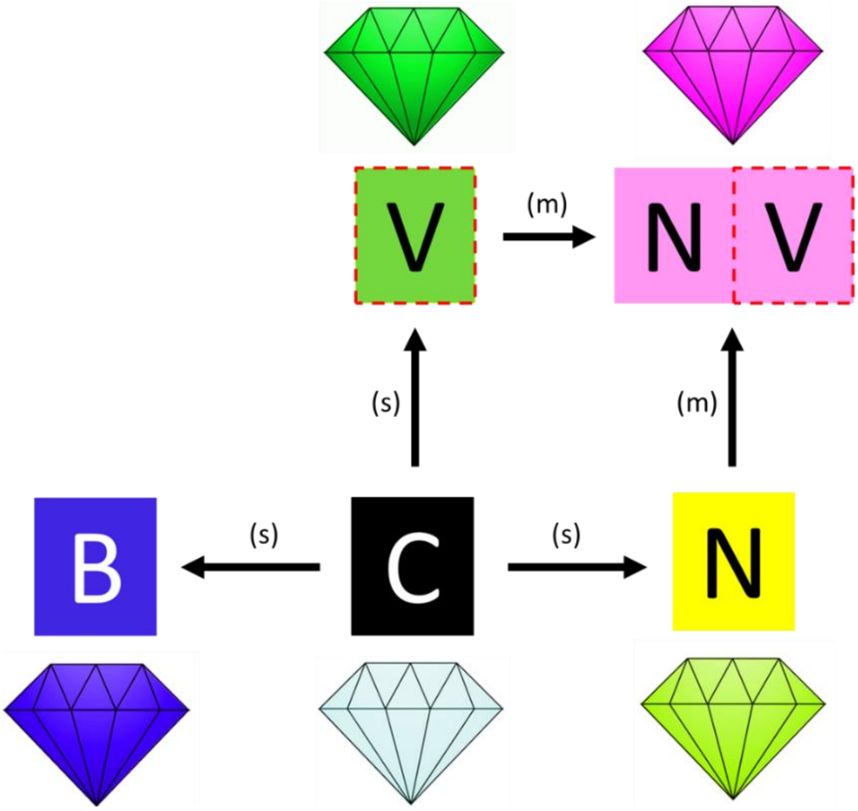

Figure 1.8 Schematic showing the effect of the presence of common point defects found in diamond on the overall diamond colour. The operation (s) refers to a substitution – a direct replacement of a carbon atom with that of another element or a vacancy site, denoted V. The operation (m) refers to a migration, where two non-carbon sites are grown in together.

1.3.1 Nitrogen in diamond

Nitrogen is a ubiquitous impurity in both synthetic and natural diamond [**62**], with most (~98%) natural diamonds typically containing 100-1000 ppm nitrogen. In synthetic diamond, the concentration of nitrogen can be controlled to within less than 1 ppb in the highest purity material [**50**]. The classification of diamond into its different types is predominantly dependent on their concentration of nitrogen, and the form in which it manifests [**63-64**]. Diamonds that contain nitrogen are labelled as type I, while those that do not contain nitrogen are labelled as type II. Figure 1.9 details how the different diamond types are classified.

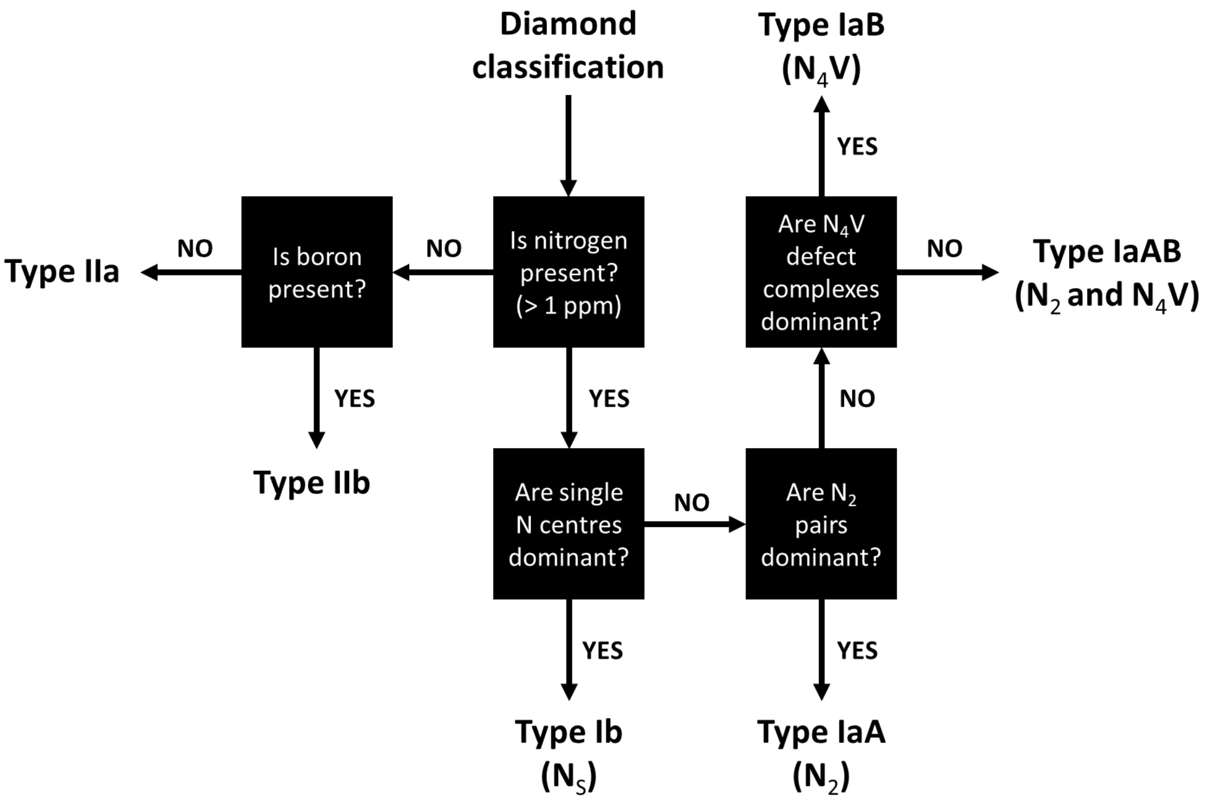

Figure 1.9 Flowchart classifying diamond by its different types. Type I diamond contains a significant concentration of nitrogen, whereas Type II diamond contains negligible nitrogen.

The simplest nitrogen defect is the single substitutional nitrogen centre (N_S), shown in Figure 1.10a, which is the dominant impurity in type Ib diamond. Here, a nitrogen atom directly replaces a carbon atom in the lattice [**57**]. This centre, commonly produced through HPHT synthesis methods, manifests as a yellow colour in diamond. Unlike boron-doped diamond, doping with nitrogen does not induce electrical conductivity, as its donor levels are too deep to facilitate n-type conductivity [**65**]. The migration of point defects, which occurs during diamond growth and annealing, produces more complex defect centres. The most well-studied of these is the $NV^{0/-}$ centre, Figure 1.10b, where a nitrogen atom and a vacancy sit next to each other [**58**]. Due to its optical and spin properties, the negatively-charged nitrogen-vacancy centre (NV^-) has been shown to have great potential in the fields of quantum computing, simulation and sensing [**58,66-67**].

In natural diamond, where synthesis takes place over a considerably long time, nitrogen tends to aggregate and form more complex defect centres. The most common of these are the A-nitrogen centre (N_2^0) [**68**], Figure 1.10c, where two nitrogen atoms exist in a pair, and the B-nitrogen centre (N_4V^0) [**69**], Figure 1.10d, where four nitrogen atoms surround a vacancy. Diamonds containing a high concentration of these defects are known as type IaA and type IaB diamonds, respectively. Diamond containing a high concentration of N_S^0 can be subject to HPHT annealing to produce N_2^0, and, subsequently, N_4V^0 [**68-69**].

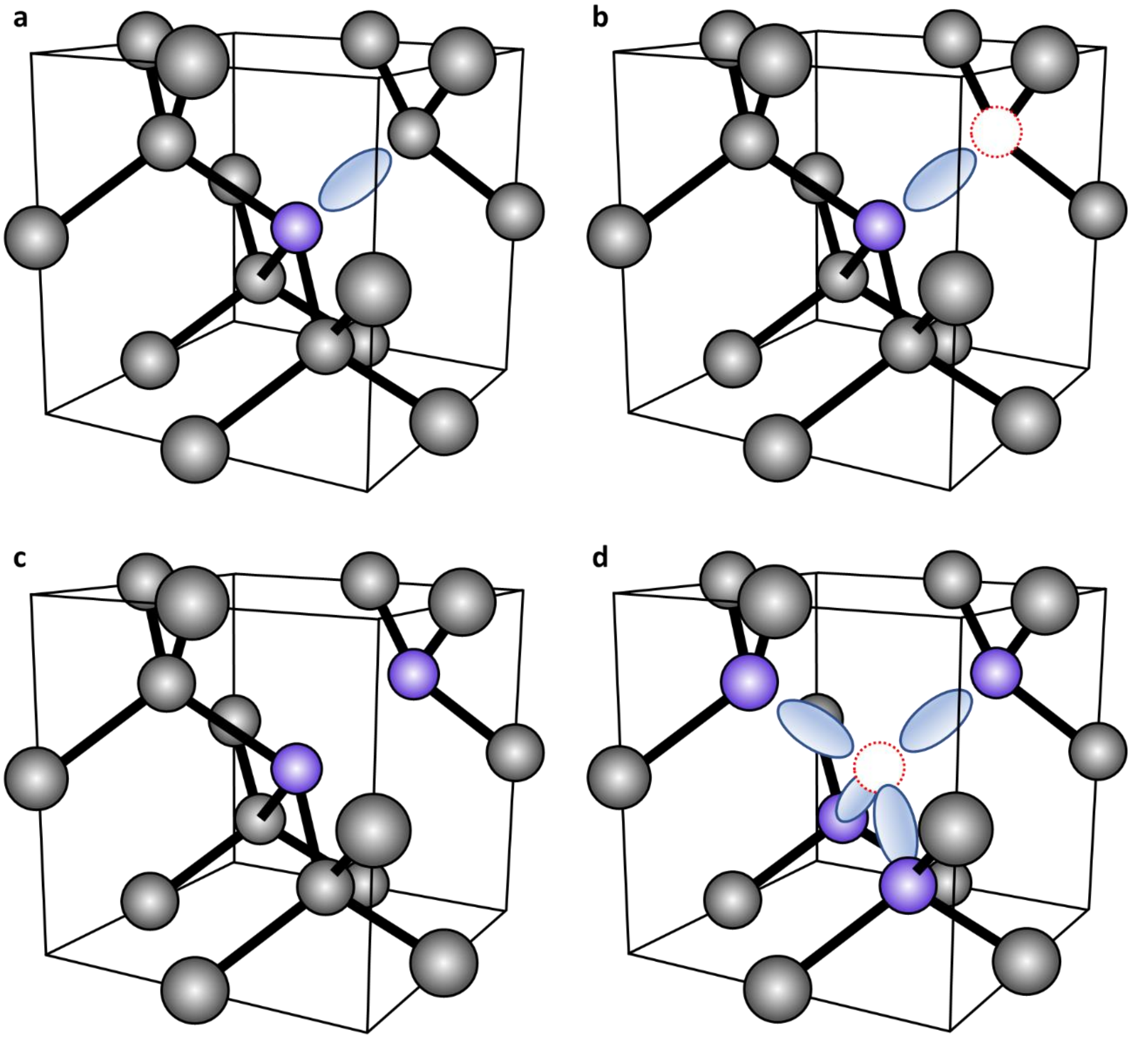

Figure 1.10 Common nitrogen-containing defect centres as they appear inside a unit cell of the diamond lattice. **a,** The substitutional nitrogen (N_S) centre; **b,** The nitrogen-vacancy (NV) centre; **c,** The A-nitrogen centre (N_2^0), **d,** The B-nitrogen centre (N_4V^0).

1.3.2 Hydrogen in diamond

Hydrogen, being the lightest of all the elements and having the smallest size, can be readily incorporated into a lattice structure of a significantly heavier atom. Its ability to interact with intrinsic defects [**70**], impurities [**71**] and surfaces [**72**] to change optoelectronic properties has attracted considerable attention. Hydrogen is known to interact readily with, and passivate, defects with dangling bonds in similar giant covalent structures, such as silicon. With the addition of hydrogen, the nitrogen-vacancy centre, $NV^{0/-}$, is converted into the stable nitrogen-vacancy-hydrogen ($NVH^{0/-}$) defect [**73-74**], shown in Figure 1.11a. When subjected to annealing, further aggregation of defects including hydrogen creates the more complex centres of the N_nVH_m family, where $n + m \leq 4$ [**62**]. One of the most well-studied of these defects is N_3VH^0 [**75**], shown in Figure 1.11b, which is described in further detail in Chapter 3. Due to its passivating nature, it is of crucial importance that hydrogen in diamond can be quantified, and that its incorporation into defects can be identified and controlled.

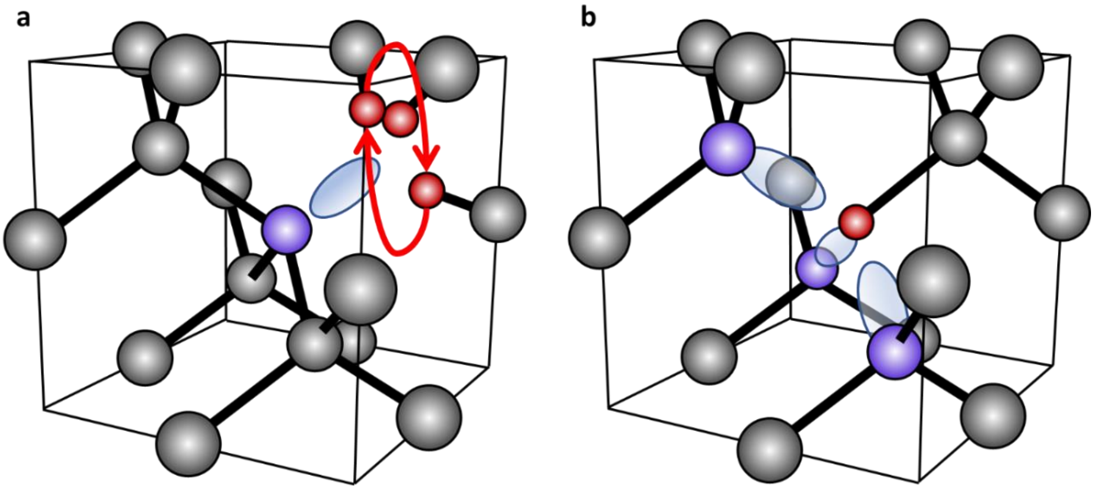

Figure 1.11 The **a,** nitrogen-vacancy-hydrogen ($NVH^{0/-}$) and **b,** N_3VH^0 defects as they appear inside a unit cell of the diamond lattice. In $NVH^{0/-}$, the hydrogen atom (red) tunnels through three different positions.

Hydrogen impurities are often found in CVD diamond, in concentrations up to 50 ppm, due to its presence in the synthesis gas mixture [**41**]. However, the hydrogen concentration can actually be higher in certain natural (up to 1000 ppm) and HPHT diamonds (200-900 ppm) [**76-77**]. Many natural, grey-violet diamonds recovered from the Argyle mine in Australia have been found to contain a high concentration of hydrogen-related defects [**78-79**]. Hydrogen-rich diamonds are most commonly brown in their colour, but can also be yellow, green or violet depending on the type of defect [**61**].

1.4 Optical absorption in diamond

1.4.1 Introduction to optical absorption

Electromagnetic waves cover a wide range of wavelengths, λ, as shown in Figure 1.12. These range from radio waves, $\lambda > 10^2$ m, to gamma waves, $\lambda < 10^{-12}$ m. Only visible light, ranging from 380-740 nm, can be detected by the human eye. The absorption of visible light by matter generates colour, and the absorption of light across the entire range can be detected using a variety of optical spectroscopic techniques. For this work, we only consider light within the infrared (IR) and ultraviolet/visible (UV/Vis) ranges of the electromagnetic spectrum.

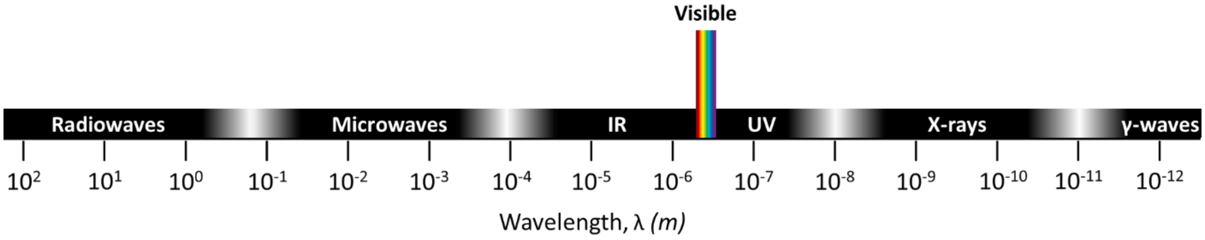

Figure 1.12 The electromagnetic spectrum of light, and its various designated regions, corresponding to their wavelengths, λ.

Many different photons may be incident on a chemical species at any given time. Optical absorption only occurs when the energy of an incident photon is equal to the difference between two discrete energy levels. This being the case, the photon is absorbed, causing a population transfer from the lower to the higher energy level. These energy levels may be characterised as electronic, vibrational or rotational. In the case of a structure such as diamond, there are no rotational degrees of freedom; as such we only consider electronic and vibrational levels.

Detection of the optical absorption of a chemical species can be achieved using a spectrometer, which collects light of a certain wavelength range and produces a plot of either absorption or transmission against those wavelengths, known as an absorption or transmission spectrum. Subtraction of the spectrum before (the background) and after the sample is introduced into the path of the light produces an overall spectrum of its optical absorption or transmission. Provided the spectrum is unsaturated, it can then be compared to known standards to attain information about the makeup, structure and concentration of the chemical species. The simplest example is the Beer-Lambert Law [**80**], which states that the absorbance, A, of a specific wavelength of light by a sample may be related to the concentration, c, of the absorbing species by the following relationship:

$$A = \varepsilon\ (\mathrm{dm^3\ mol^{-1}\ cm^{-1}}) \times c\ (\mathrm{mol\ dm^{-3}}) \times L\ (\mathrm{cm}) \tag{1.2}$$

where ε is the molar absorption coefficient of the absorbing species and L is the overall optical path length of the sample. In principle, this equation can be used to determine the concentration of an absorbing species in a sample, provided that its molar absorption coefficient is known, and the absorption spectrum is not saturated.

Before discussing the observed absorption spectrum of diamond, we first consider its electronic and vibrational structure, which enables us to ascertain the origin of its absorption.

1.4.2 Electronic structure of diamond

An atom of any element contains a set of atomic orbitals (AOs), with corresponding discrete energy levels, which are filled with its electrons starting from the lowest energy 1s orbitals. With six electrons, a single carbon atom includes completely filled 1s and 2s energy levels, alongside partially filled 2p energy levels. The core 1s orbitals can be ignored. In the case of a methane molecule, CH_4, overlap may occur between the 2s and 2p carbon AOs and the 1s orbitals of each individual hydrogen atom, creating molecular orbitals (MOs). These also exist as discrete energy levels, filled by electrons starting from the lowest energy level. MOs are characterised as either bonding, where the electron probability exists in between the atoms, or antibonding, where the electron probability exists outside the atoms. Bonding orbitals are always lower in energy than their associated antibonding orbital. In order to form four equivalent AOs for overlap with the hydrogen 1s AOs, the 2s and partially filled 2p orbitals in the carbon atom interact strongly with each other and hybridise, forming sp^3 orbitals which contain 25% s character and 75% p character. These orbitals require extra energy to be borrowed for their formation, but are overall lower in energy and contribute to a lower energy structure for a CH_4 molecule. Figure 1.13 demonstrates the process of hybridization, while Figure 1.14 shows the MO energy level diagram of a single methane molecule.

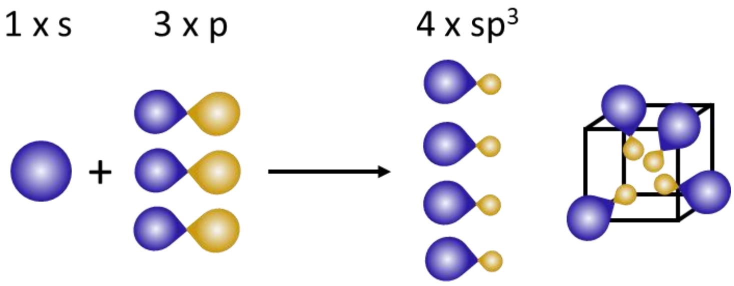

Figure 1.13 Hybridisation of the 2s and 2p carbon AOs to form four identical sp^3 hybrid orbitals, which may bond to each of four nearest neighbours.

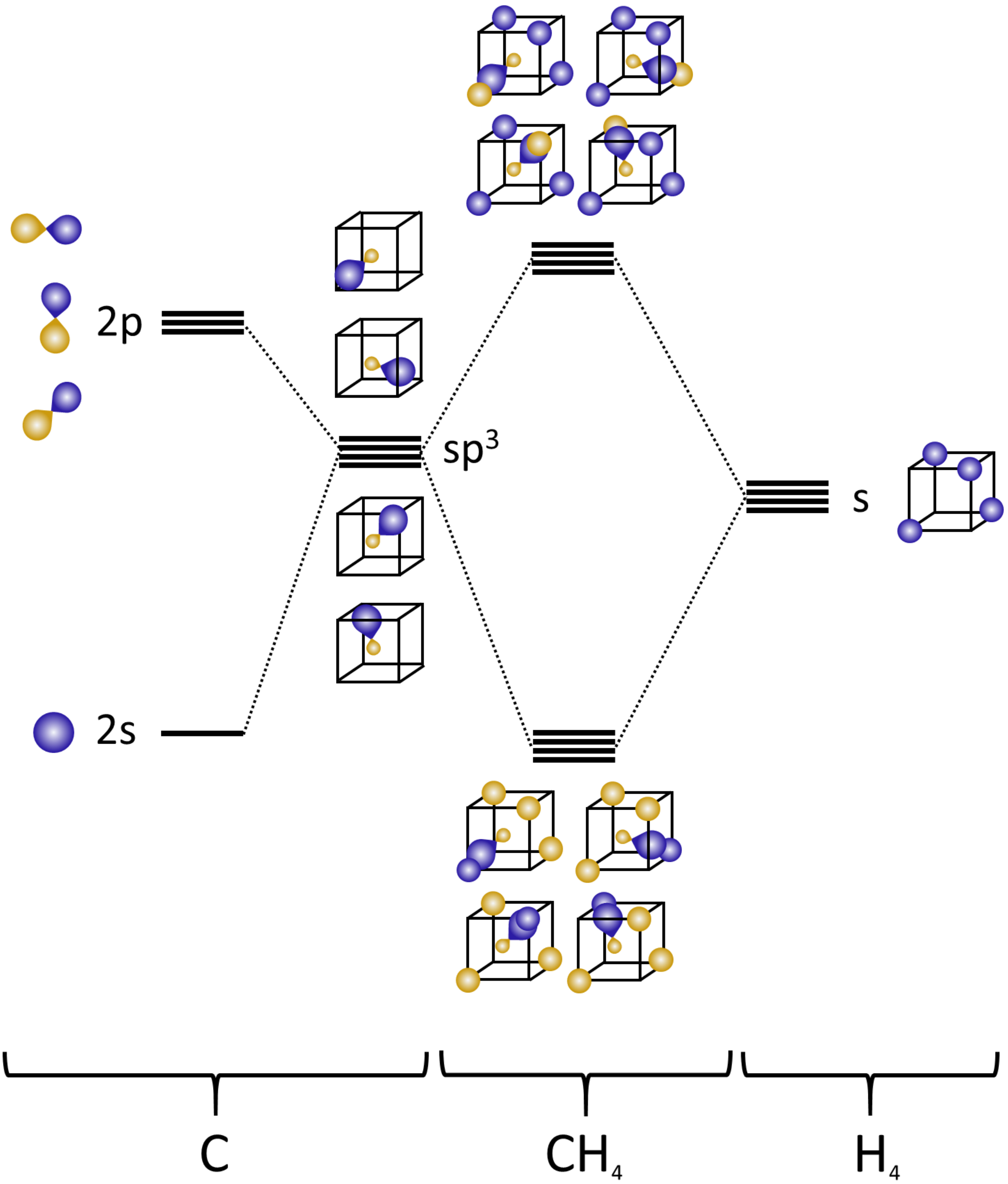

Figure 1.14 MO levels of CH_4, formed from the 2s and 2p AO levels in a carbon atom, which hybridise to form four sp^3 AOs, and the 1s AO levels of four hydrogen atoms. The core 1s carbon AOs are not shown. Blue and orange represent the two different orbital phases.

In the case of diamond, we are only considering bonds between carbon atoms. As with methane, the core 1s orbitals can be ignored, and the carbon 2s and 2p orbitals hybridise to form four sp^3 orbitals. Instead of overlapping with a hydrogen 1s orbital, each sp^3 hybrid orbital interacts with a sp^3 hybrid orbital from one of four nearest neighbour carbon atoms, forming both a bonding and an antibonding MO. Each carbon atom thus interacts with four other carbon atoms, forming a set of four bonding MOs and four antibonding MOs, and creating a large repeating lattice structure, where the number of carbon atoms and thus the number of energy levels tends towards infinity. As the number of energy levels increases, the bonding orbitals grow closer together, as do the antibonding orbitals. Approaching infinity, the spacing between the energy levels becomes negligible, resulting in continuum bands. Two bands are created: a band made up of bonding orbitals, the valence band (VB), and one band made up of antibonding orbitals, the conduction band (CB). These bands are shown in Figure 1.15.

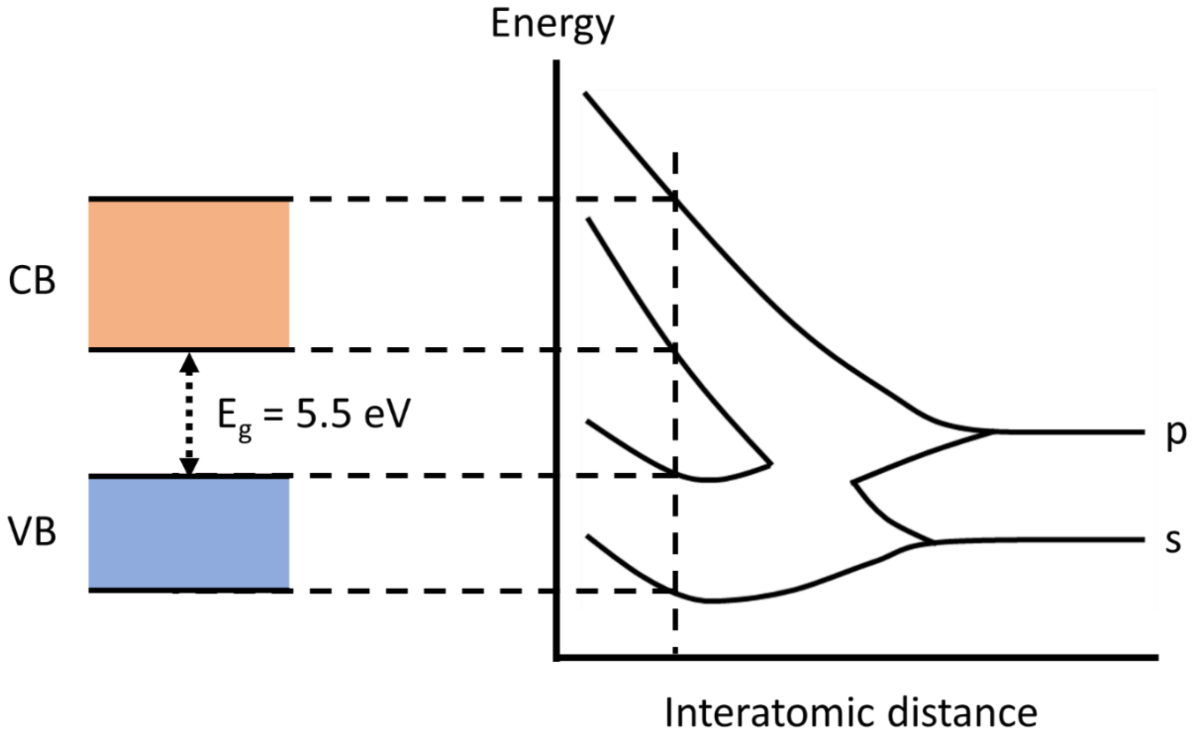

Figure 1.15 Continuum bands in diamond, formed from the 2s and 2p atomic orbital levels in each carbon atom, as the atoms get closer together. The core 1s orbitals are not shown.

Each of these bands may occupy four electrons per carbon atom. As such, the VB is entirely filled, and the CB is entirely unfilled. The energy difference between the top of the VB and the bottom of the CB is known as the band gap, E_g. In diamond, the band gap is equal to 5.5. eV, or roughly 225 nm [**81**]. Due to the high energy requirement for the promotion of free carriers (electrons into the CB, leaving behind holes in the VB), pure diamond acts as an insulator. Furthermore, as it only absorbs UV light of wavelength $\lambda < 225$ nm, it is also colourless. If diamond contains defects, these behave akin to small molecules and thus introduce discrete energy levels inside the band gap, which may act to encourage electrical conductivity, and may absorb light in the visible range, giving the diamond colour.

1.4.3 Vibrational structure of diamond

Vibrational modes produced in a lattice are known as phonons. These arise due to internal displacement of the atoms, collectively oscillating about their equilibrium positions. In cases where there is a difference in polarity between two nearest-neighbour atoms in the lattice, the vibration of a phonon induces a permanent dipole moment and allows the absorption of a photon of equal frequency to the phonon. The energy gained from excitation is lost by vibration – the emission of a number of phonons – to return to equilibrium. Phonons have a resonant frequency, ω, which is dependent on their wavevector, k, being plotted on a dispersion curve (Figure 1.16). There are two categories of phonons: acoustic phonons, where nearest neighbours move parallel to each other, and optical phonons, where the atoms move in opposition to their nearest neighbours. According to the phonon dispersion curve in diamond, the frequency of its phonon bands ranges between 0-1332 cm^{-1} [**82**]. Phonons may have a higher frequency away from zone centres, but the photon does not have sufficient momentum to absorb there.

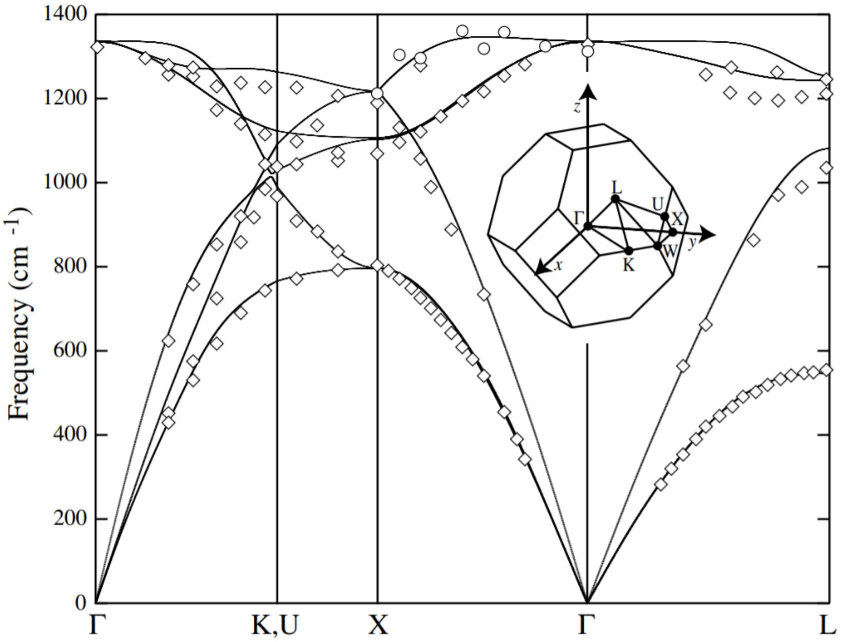

Figure 1.16 The phonon dispersion curve of diamond. Reproduced from [**83**].

1.4.4 Pure diamond absorption

Pure, type IIa diamond reflects roughly only 30% of incident light and thus displays a broad transmission window across the UV, visible and IR spectrum [**84**], shown in Figure 1.17. The observed intrinsic absorption features are: (1) UV absorption at wavelengths < 225 nm; (2) A small reduction to transmission between 225-500 nm; and (3) IR absorption between 1500 and 4000 cm^{-1}. The occurrence of absorption in each of these cases is accounted for below.

The intense UV absorption at wavelengths λ < 225 nm is due to the incoming light being of sufficient energy to exceed the diamond band gap, and thus promote electrons from the VB into the CB. Any light at wavelengths λ > 225 nm is of insufficient energy to excite electrons, and absorption at these wavelengths must be accounted for by an alternative explanation. Additionally, the small reduction in the transmission at wavelengths approaching the diamond band gap, in the range λ = 225-500 nm, is due to Fresnel reflection at the diamond surface, rather than being due to absorption.

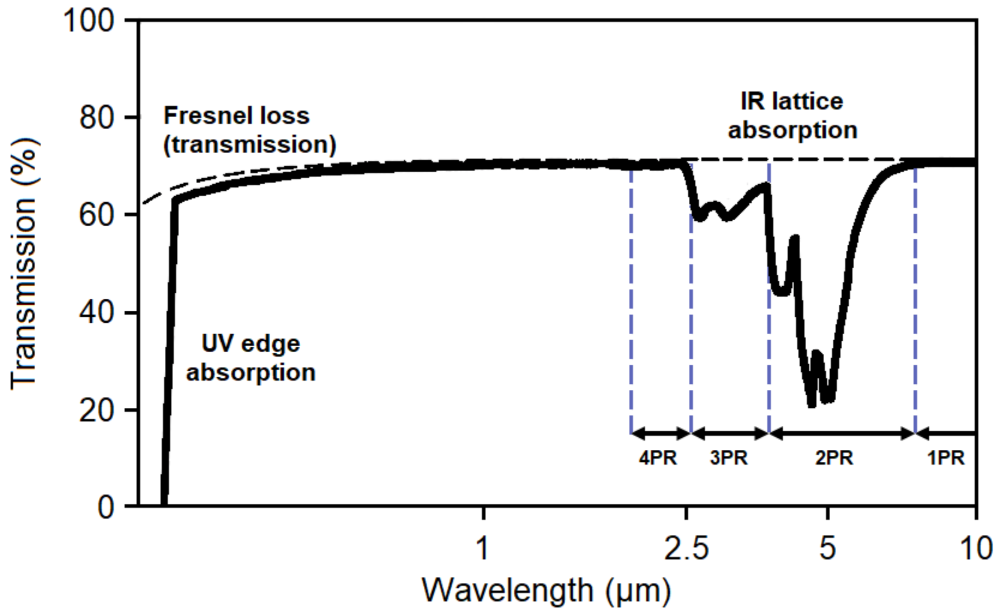

Figure 1.17 Transmission spectrum of pure, type IIa diamond, measured from the UV to the IR and denoting the three regions of intrinsic diamond absorption and each phonon region (PR) of diamond absorption. Adapted from [**84**].

Pure diamond is a highly symmetrical structure and contains only C–C bonds. Therefore, any movement of an atom in the lattice is counteracted by movement of its neighbours, thus cancelling out any changes to the polarity. In this case, a dipole moment cannot be set up, and any incident photon cannot be absorbed. The high transmittance of pure diamond in the IR is therefore not surprising. The IR absorption features that do appear in pure diamond arise due to multiphonon absorption. Here, an incident photon interacts with two or more phonons in the diamond lattice. In this case, one phonon may create the dipole moment in a localized region of the lattice, and one or more additional phonons subsequently vibrate to allow the absorption of a photon. Since the maximum phonon vibrational frequency in diamond is 1332 cm^{-1} [**82**], the absorption between 1500-5500 cm^{-1} can be accounted for by dividing the bands into the two-, three- and four-phonon regions (PRs), as marked out in Figure 1.17. As the number of phonons required increases, the likelihood of interaction of a photon with sufficient phonons reduces, and thus the bands grow weaker in the four-phonon region and beyond.

1.5 Defect-induced absorption in diamond

Both intrinsic and extrinsic defects in diamond can induce absorption, since they create new electronic and vibrational states from and to which absorption may take place. Due to the defect being surrounded by a regular lattice structure, it has no rotational degrees of freedom and thus we do not consider rotational states.

Extra electronic states arise because of the differing overlap of carbon AOs with the AOs belonging to the atoms in the defect. As a defect centre is a localised environment surrounded by the diamond lattice, its electronic states can be treated in the same manner as a small molecule: with discrete MO energy levels formed by the combination of AOs. These often appear inside the diamond band gap, thus allowing UV absorption at longer wavelengths to either fill or empty these new states.

New vibrational states are created due to the break the symmetry of the diamond lattice that occurs when a defect is present. These new vibrational modes can be considered as a bond or interaction between atoms of two different elements, and thus induce the dipole moments required for IR absorption [**85**]. Where the frequency of the mode is less than 1332 cm^{-1}, the one-phonon threshold, it is possible for them to propagate out from the defect and through the diamond lattice. Thus, their lifetime is comparatively short and they produce broad absorption features. Defect-induced modes of frequencies above 1332 cm^{-1} are known as local vibrational modes (LVMs). Where the frequency is below 1332 cm^{-1}, the vibrational modes are localised to the defect itself and cannot propagate. Thus, their lifetime is comparatively long and they produce sharp absorption features.

For this work, we focus on vibrational transitions responsible for absorption in the IR region, particularly the region above 1332 cm^{-1} which corresponds to LVMs of defects. Some electronic transitions associated with defects are considered in our work in Chapter 5.

1.5.1 Local vibrational modes of defects

The LVMs of a defect can be considered to have discrete vibrational states that can be occupied. This can be seen most clearly in extrinsic defects, which contain covalent bonds between atoms of different elements, A–B, that possess a permanent dipole moment.

The electronic potential energy of any bond in a defect centre can be modelled as a function of the distance *r* between the two atoms. The simplest model considers the vibrations in a bond as a harmonic oscillator and produces the potential well shown in Figure 1.18a. This potential well includes discrete, evenly spaced vibrational states which belong to specific LVMs. The gaps between vibrational states after the first excited state are known as overtones. In reality, the harmonic oscillator model is greatly oversimplified and does not take into account the effect of bond breaking. A more accurate representation is an anharmonic potential well, such as that shown in Figure 1.18b, which shows a decrease in the energy level spacing as the energy increases towards the amount required for bond dissociation.

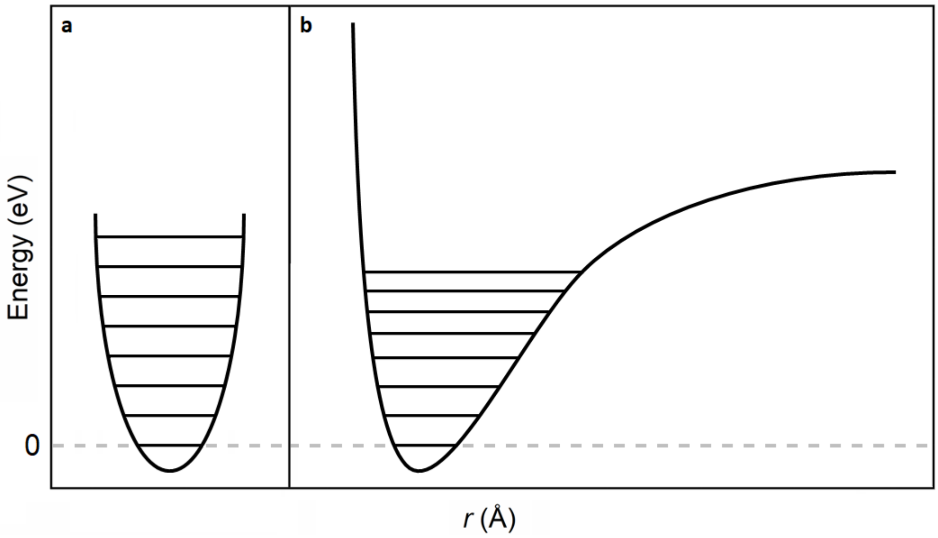

Figure 1.18 a, Harmonic and **b,** anharmonic potential wells of a covalent bond in a diamond defect, A–B, including discrete vibrational states.

When an incident photon is resonant with a LVM of the defect, it is absorbed, exciting the mode into a higher vibrational state. This causes the LVM to vibrate, until it has lost this energy through relaxation back to its vibrational ground state. A LVM may only be IR active if it has a non-zero electric dipole moment. Whether a vibrational mode is IR active or not depends on the structure of the defect site or molecule. For example, in a linear AB_2 molecule, four LVMs, shown in Figure 1.19, are possible: a symmetric stretch, an asymmetric stretch, an in-plane bend and an out-of-plane bend. The symmetric stretch has zero dipole moment and is therefore IR inactive, whereas the other three modes have non-zero dipole moments and are IR active.

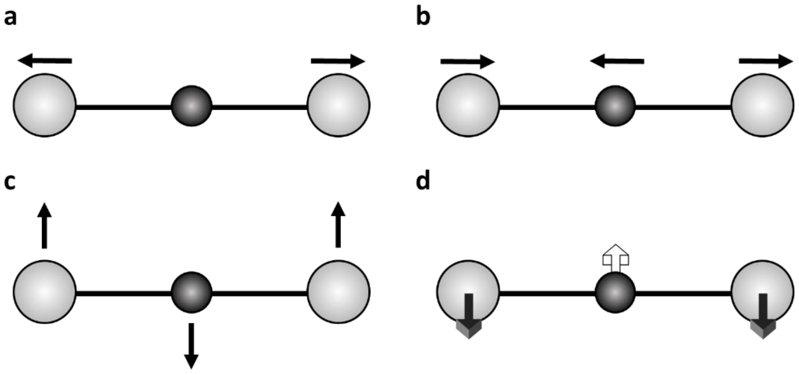

Figure 1.19 Possible LVMs in a linear AB_2 molecule. **a,** symmetric stretch **b,** asymmetric stretch **c,** in-plane bend **d,** out-of-plane bend.

In a nonlinear AB_2 molecule, shown in Figure 1.20, three LVMs are possible: a symmetric stretch, an asymmetric stretch and a bend. In this case, all three LVMs change the overall dipole moment, therefore meaning that all three modes are IR active. As the structure of a defect becomes more complex, the change in dipole moment can become more difficult to determine. This is aided by considering the symmetry elements of the defect.

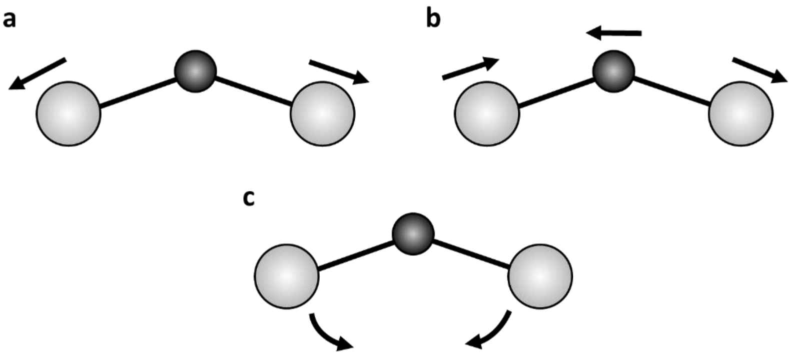

Figure 1.20 Possible LVMs in a non-linear AB_2 molecule. **a,** symmetric stretch **b,** asymmetric stretch **c,** bend.

When the energy of an incoming photon is sufficient to excite it to the higher vibrational states of a higher electronic level, the transition is often given the term vibronic, which groups the electronic and vibrational energies. Transitions of this nature are only considered in Chapter 5.

1.5.2 Examples of defect-induced absorption in diamond

Many of the defects previously discussed in Section 1.3 include C–N or C–H bonds, often surrounded by other impurity atoms. As such, they contain IR active LVMs, the most commonly observed of which are detailed in Table 1.1 [**57,68-69,73-74,86**]. Nitrogen being of similar mass to carbon, the C–N related modes are found in the one-phonon region and thus generally have a complex band structure. Since hydrogen is lighter, the C–H modes are usually located in the two-, three- or four-phonon region and are characteristically sharp features.

Of these features, we draw particular attention to the C–H stretch mode at 3107 cm^{-1}, belonging to the N_3VH^0 defect, and the unknown stretch mode at 3237 cm^{-1}, which will be the focus of our studies in Chapters 3-5. The characteristic absorptions of the A- and B-nitrogen centres, N_2^0 and N_4V^0 will also be important in our discussion during Chapter 4. Figure 1.21 shows the normalised absorption from each of these defects.

Table 1.1 Absorption features associated with nitrogen and hydrogen-related defects in diamond. The wavenumber (ω) of each absorption peak is as reported in the literature [**57,68-69,73-74,86**].

Absorption region	ω (cm^{-1})	Description	Vibrational mode	Defect
One-phonon region	1130	Broad band	C–N band	N_S^0
	1280	Broad band	C–N band	N_4V^0
	1282	Broad band	C–N band	N_2^0
	1332	Sharp, single feature	C–N	N_4V^0
Two-phonon region	1344	Sharp, single feature	C–N	N_S^0
	1405	Sharp, single feature	C–H bend	N_3VH^0
Three-phonon region	3107	Sharp, single feature	C–H stretch	N_3VH^0
	3123	Sharp, single feature	C–H stretch	NVH^0
	3237	Sharp, single feature	Unknown stretch	Unknown

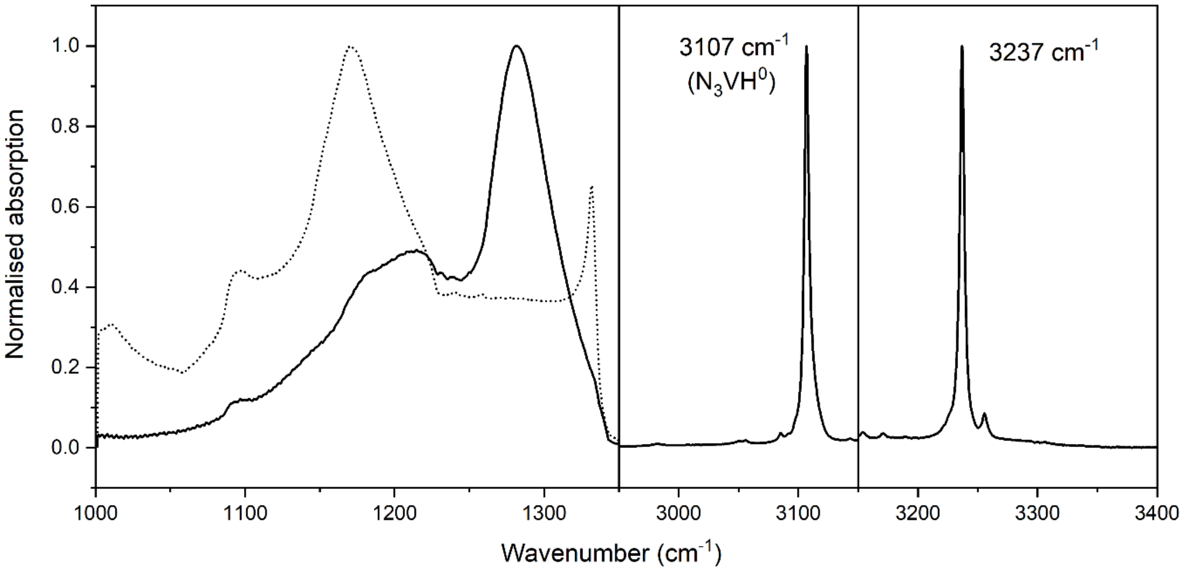

Figure 1.21 Normalised characteristic absorption spectra observed in diamond that contains a high proportion of A- and B-nitrogen centres, N_3VH^0 and the unknown defect associated with the LVM at 3237 cm^{-1}.

1.5.3 Symmetry of local vibrational modes

A determination of the symmetry character of a defect centre provides a gateway to predicting both its energy level structure and its possible relaxation mechanisms. Symmetry is especially important when considering the relaxation of an excited vibrational state, as coupling between vibrational states is only allowed when the two states contain an overlap in their symmetry elements [**87-88**]. Thus, knowledge of the symmetry character of each vibrational level in a system allows each transition between levels to be classified as either allowed, where the symmetry character overlaps, or forbidden, where there is no overlap.

The symmetry character of individual vibrational levels is determined by first considering the symmetry of their associated molecule. Depending on the symmetry operations that can be carried out on a molecule, it may belong to one of a number of point groups. Defect complexes, being surrounded by a regular, repeating lattice, also have specific point groups. For example, the N_3VH^0 defect can be subject to the following symmetry operations: the identity (E) operation, 2 C_3 rotations and 3 σ_V mirror planes. It therefore belongs to the C_{3V} point group, the character table of which is shown in Table 1.2.

Table 1.2 Character table for the C_{3V} point group.

C_{3V}	E	$2C_3\ (z)$	$3\sigma_V$
A_1	+1	+1	+1
A_2	+1	+1	-1
E	+2	-1	0

A character table is used to determine the symmetry of LVMs of defect complexes that belong to its point group, according to the following three rules [**89**]: (1) When a vibrational mode is nondegenerate, the symmetry character of its nth overtone is equal to the nth exponent of the fundamental; (2) When a vibrational mode is degenerate, the symmetry character of its nth overtone is equal to $\chi_E^n(R)$:

$$\chi_E^n(R) = \frac{1}{2}[\chi_E^{n-1}(R)\chi_E(R) + \chi_E(R^n)] \qquad (1.3)$$

where $\chi_E(R^n)$ is the symmetry character of the operation R carried out n consecutive times; and (3) The symmetry character of a combination band is the direct product of the symmetry of the individual levels.

A phonon-mediated transition between two vibrational energy levels in a system is allowed only if the two levels in question contain overlapping symmetry character. In the case of a system in the C_{3V} point group, its 1st excited stretch mode has A_1 symmetry character and its 1st excited bend mode has E symmetry character. As there is no symmetry overlap, population transfer between these two levels is forbidden. Following Equation 1.3, the 2nd excited bend mode is determined to have $A_1 + E$ symmetry character. Since both it and the 1st excited stretch mode contain A_1 symmetry character, population transfer between these two levels is allowed.

1.5.4 Isotopic effects of local vibrational modes

Assuming a harmonic oscillator, the frequency, ω, of a vibration varies according to the following equation:

$$\omega = \sqrt{\frac{k}{\mu}} \qquad (1.4)$$

where k is the spring constant of the oscillator and μ is the reduced mass of the atoms involved in the bond causing the vibration. Thus, the presence of an isotope of an atom in a LVM changes both its mass and its frequency. In nature, the majority of carbon is ^{12}C, with a small but substantial 1.1% being ^{13}C. LVMs that include carbon will always have a smaller accompanying feature that accounts for the presence of ^{13}C, with the ratio of intensity between the two features matching the ratio of ^{13}C:^{12}C in nature. For example, the 3107 cm^{-1} C–H LVM of N_3VH^0 has an accompanying ^{13}C–H mode at 3098 cm^{-1} [**90**]. Checking for an isotopic shift is thus an excellent way of identifying the constituent elements of a LVM. Diamonds can also be specifically grown to have a high proportion of ^{13}C or other isotopes, to observe these shifted features with greater clarity.

1.5.5 Relaxation processes of local vibrational modes

When a LVM vibrates at a frequency resonant to an incoming photon, it absorbs it and moves from its ground state to an excited state, the difference of which is the energy of the photon. Once in this excited state, the LVM does not remain populated indefinitely. Instead, it relaxes back to its ground state, returning the system back to equilibrium. The energy gained through photon absorption is lost through non-radiative emissions, typically the emission of phonons. The lifetime for the overall population relaxation of an excited LVM is known as the excited-state lifetime, T_1. At low temperature, in an otherwise uniform crystal, T_1 can be related to the linewidth Γ, of the characteristic absorption line from a LVM by the following relation:

$$\Gamma = \frac{1}{2\pi T_1} \tag{1.5}$$

There are two additional contributors to this linewidth that must be considered: (1) pure dephasing, whereby elastic scattering of the LVM reduces its phase coherence. The lifetime for recovery from pure dephasing is defined as T_2^*; and (2) Inhomogeneous broadening of the absorption line, which occurs when the defects responsible for the LVM are subjected to localised environments in the diamond lattice that contain slight differences, due to the presence of defects in different positions across the sample. The extent of inhomogeneous broadening tends to be larger when there is a higher concentration of defects in the diamond sample. Effects due to inhomogeneous broadening are termed Γ_{in}.

The overall linewidth, Γ, of the characteristic absorption line from a LVM can thus be determined using the following equation:

$$\Gamma = \frac{1}{T_2} = \frac{1}{2\pi T_1} + \frac{1}{\pi T_2^*} + \Gamma_{\mathrm{in}} \tag{1.6}$$

where T_2 is the overall relaxation time, containing all contributions to the linewidth. Separating out these three components is therefore crucial to the use of the linewidth to estimate for the excited-state lifetime, T_1. One of the primary goals of this thesis is to directly determine T_1 through the use of ultrafast pump-probe spectroscopy, which enables us to comment on the extent of broadening caused by contributions from dephasing and inhomogeneity.

1.6 Thesis outline

In this work, we report that time- and energy-resolved IR absorption spectroscopy can access the potential energy landscape of atomic scale defects and can determine the rate of vibrational coupling to their surroundings. We specifically focus on the 3107 cm^{-1} C–H LVM of the N_3VH^0 defect in diamond and the unknown defect associated with the 3237 cm^{-1} X–H LVM. These two defects were chosen for three reasons: (1) The high intensity of their IR features, especially in comparison to other diamond defects, whose absorption intensity in the FTIR is often below 1 cm^{-1}; (2) The presence of their IR features in a wavenumber range that is easily accessible (2000-6000 cm^{-1}); (3) The relative isolation of their IR features from other features of diamond absorption, and from each other. These factors make these two defects ideal starting points for the first time-resolved IR pump – IR probe measurements on diamond. Successful experiments on these defects will pave the way for further application of the same technique to other defects.

Obtaining information about the vibrational dynamics of these defects following IR excitation of their stretch modes provides information about the energies of quantised vibrational states and allows mapping out of the energy relaxation pathways. These pathways vary, and may include multi-phonon relaxation, or anharmonic coupling to the analogous bend modes. Additionally, the use of UV excitation provides another avenue to probing vibrational states – this time as the system relaxes back down from electronic excitation, which opens up the possibility of observing higher vibrational states of the electronic ground state.

Employment of time-resolved spectroscopy also allows the anharmonicity of the potential wells associated with these defects to be determined. This opens up a new route to quantification of impurities (in this case both nitrogen and hydrogen) incorporated into IR active defects. This is vital to the characterization of diamond and feeds back into an understanding of synthesis, response to treatments and impurity incorporation.

Chapter 2 details both the experimental setups used in this work: Fourier transform infrared (FTIR) spectroscopy, ultraviolet/visible (UV/Vis) spectroscopy and transient vibrational absorption spectroscopy (TVAS). Additionally, we supply details of the diamond samples used for this work, explain how the FTIR linewidths and TVAS lifetimes can be related to draw out the individual components to the linewidth, and detail the model of the Morse potential used in the following Chapters.

Chapter 3 includes our study of the C–H stretch mode belonging to N_3VH^0, observed in the IR at 3107 cm^{-1}. We map out its relaxation dynamics and anharmonicity, account for its observed linewidth in each of our samples and determine a relationship between its intensity in an IR spectrum and its concentration in any given sample.

In Chapter 4, we apply the same methods as in Chapter 3, this time to the X–H stretch mode observed in the IR at 3237 cm^{-1}. This mode is not yet assigned to a defect. As such, we were able to comment on its potential origin and relationship with the B-nitrogen centre.

In Chapter 5, we carry out a study of the behaviour of the two modes at 3107 cm^{-1} and 3237 cm^{-1} when excited with UV light. We compare the effect of a significant concentration of defects on the free carrier relaxation of diamond, and the effect of electronic excitation of a defect on its vibrational states.

In Chapter 6, we detail the conclusions that can be made from our studies, and offer an outlook into the future applications of using ultrafast spectroscopy to study diamond defects.

1.7 References

1. Exodus 28:18, *English Standard Version Bible*, **2001**.

2. R.P. Kangle, *The Kautiliya Arthra-Sastra, Pt. 2*, Delhi: India, **1986**, 98.

3. Pliny the Elder, *Natural History - A Selection*, Penguin Classics: UK, **1991**.

4. R. Berman, F. Simon, *Z. Elektrochem.* **1955**, *59*, 333-338.

5. F. P. Bundy, H. P. Bovenkerk, H. M. Strong, R. H. Wentorf, *J. Chem. Phys.* **1961**, *35*, 383-391.

6. F. R. Boyd, J. J. Gurney, *Science* **1986**, *232*, 472-477.

7. T. Stachel, J. W. Harris, *Ore Geol. Rev.* **2008**, *34*, 5-32.

8. T. Stachel, J. W Harris, *J. Phys. Condens. Matter* **2009**, *21*, 364206.

9. T. Stachel, R.W. Luth, *Lithos* **2015**, *220*, 200-220.

10. J. J. Gurney, R. O. Moore, M. L. Otter, M. B. Kirkley, J. J. Hops, T. E. McCandless, *Magmatism in Extensional Structural Settings*, Springer: USA, **1991**, 495-536.

11. H. Bureau, D. J. Frost, N. Bolfan-Casanova, C. Leroy, I. Esteve, P. Cordier, *Lithos* **2016**, *265*, 4-15.

12. R. Tappert, T. Stachel, J. W. Harris, K. Muehlenbachs, T. Ludwig, G. P. Brey, *Geology* **2005**, *33*, 565-568.

13. M. Miyahara, E. Ohtani, A. El Goresy, Y. Lin, L. Feng, J.-C. Zhang, P. Gillet, T. Nagase, J. Muto, M. Nishijima, *Geochim. Cosmochim. Acta* **2015**, *163*, 14–26.

14. M. E. Lipschutz, *Science* **1964**, *143*, 1431–1434.

15. K. Fukunaga, J. Matsuda, K. Nagao, M. Miyamoto, K. Ito, *Nature* **1987**, *328*, 141–143.

16. H. C. Urey, *Astrophys. J.* **1956**, *124*, 623–637.

17. F. P. Bundy, H. T. Hall, H. M. Strong, R. H. Wentorf, *Nature* **1955**, *176*, 51-55.

18. H. P. Bovenkerk, F. P. Bundy, H. T. Hall, H. M. Strong, R. H. Wentorf, *Nature* **1959**, *184*, 1094-1098.

19. F. P. Bundy, *Science*, **1962**, *137*, 1057-1058.

20. U. F. S. D'Haenens-Johansson, A. Katrusha, K. S. Moe, P. Johnson, W. Wang, *Gems Gemol.* **2015**, *51*, 260-279.

21. R. Abbaschian, H. Zhu, C. Clarke, *Diam. Relat. Mater.* **2005**, *14*, 1916–1919.

22. S. Eaton-Magaña, J. E. Shigley, C. M. Breeding, *Gems Gemol.* **2017**, *53*, 262-284.

23. F. De Weerdt, A. T. Collins, *New Diamond Front. Carbon Technol.* **2007**, *17*, 91-103.

24. Q. Liang, C.-S. Yan, Y. Meng, J. Lai, S. Krasnicki, H.-K. Mao, R. J. Hemley, *Diam. Relat. Mater.* **2009**, *18*, 698–703.

25. M. Frenklach, K. E. Spear, *J. Mater. Res.* **1988**, *3*, 133-140.

26. M. N. R. Ashfold, P. W. May, C. A. Rego, N. M. Everitt, *Chem. Soc. Rev.* **1994**, *23*, 21-30.

27. S. Matsumoto, Y. Sato, M. Tsutsumi, N. Setaka, *J. Mater. Sci.* **1982**, *17*, 3106-3112.

28. B. V. Spitsyn, L. L. Bouilov, B. V. Derjaguin, *J. Cryst. Growth* **1981**, *52*, 219-226.

29. M. Kamo, Y. Sato, S. Matsumoto, N. Setaka, *J. Cryst. Growth* **1983**, *62*, 642-644.

30. P. W. May, N. M. Everitt, C. G. Trevor, M. N. R. Ashfold, K. N. Rosser, *Appl. Surf. Sci.* **1993**, *68*, 299-305.

31. A. Tallaire, C. Rond, F. Bénédic, O. Brinza, J. Achard, F. Silva, A. Gicquel, *Phys. Status Solidi A* **2011**, *208*, 2028-2032.

32. S. Jin, T. D. Moustakas, *Appl. Phys. Lett.* **1994**, *65*, 403-405.

33. S. Bohr, R. Haubner, B. Lux, *Appl. Phys. Lett.* **1996**, *68*, 1075-1077.

34. W. Müller-Sebert, E. Wörner, F. Fuchs, C. Wild, P. Koidl, *Appl. Phys. Lett.* **1996**, *68*, 759-760.

35. M. Frenklach, H.Wang, *Phys. Rev. B* **1991**, *43*, 1520-1545.

36. P. K. Bachmann, D. Leers, H. Lydtin, *Diam. Relat. Mater.* **1991**, *1*, 1-12.

37. M. Schreck, J. Asmussen, S. Shikata, J.-C. Arnault, N. Fujimori, *MRS Bull.* **2014**, *39*, 504-510.

38. P. Bergonzo, A. Brambilla, D. Tromson, C. Mer, B. Guizard, F. Foulon, V. Amosov, *Diam. Relat. Mater.* **2001**, *10*, 631-638.

39. C. J. J. Wort, R. S. Balmer, *Mater. Today* **2008**, *11*, 22-28.

40. J. Achard, V. Jacques, A. Tallaire, *J. Phys. D:Appl. Phys.* **2020**, *53*, 313001.

41. K. M. Rutledge, K.K. Gleason, *Chem. Vap. Depos.* **1996**, *2*, 37-43.

42. A. Secroun, O. Brinza, A. Tardieu, J. Achard, F. Silva, X. Bonnin, K. De Corte, A. Anthonis, M.E. Newton, J. Ristein, P. Geithner, A. Gicquel, *Phys. Status Solidi A* **2007**, *204*, 4298–4304.

43. C. A. Coulson, F. P. Larkins, *J. Phys. Chem. Solids* **1971**, *32*, 2245-2257.

44. V. Avalos, S. Dannefaer, *Physica B: Condens. Matter* **2003**, *340-342*, 76-79.

45. H. E. Smith, G. Davies, M. E. Newton, H. Kanda, *Phys. Rev. B* **2004**, *69*, 045203.

46. J. P. Goss, B. J. Coomer, R. Jones, T. D. Shaw, P. R. Briddon, M. Rayson, S. Öberg, *Phys. Rev. B*, **2001**, *63*, 195208.

47. J. Hornstra, *J. Phys. Chem. Solids* **1958**, *5*, 129-141.

48. P. Humble, J. K. Mackenzie, A. Olsen, *Philos. Mag. A* **1985**, *52*, 605-621.

49. C. S. Erasmus, J. P. F. Sellschop, D. M. Bibby, H. W. Fesq, E. J. D. Kable, R. J. Keddy, D. M. Hawkins, D. W. Mingay, S. E. Rasmussen, M. J. Renan, J. I. W. Watterson, *J. Radioanal. Chem.* **1977**, *38*, 133-146.

50. J. Isberg, J. Hammersberg, E. Johansson, T. Wikström, D. J. Twitchen, A. J. Whitehead, S. E. Coe, G. A. Scarsbrook, *Science* **2002**, *297*, 1670-1672.

51. A. J. Eccles, T. A. Steele, A. Afzal, C. A. Rego, W. Ahmed, P. W. May, S. M. Leeds, *Thin Solid Films* **1999**, *343-344*, 627-631.

52. Z. Z. Liang, X. Jia, H. A. Ma, C. Y. Zang, P. W. Zhu, Q. F. Guan, H. Kanda, *Diam. Relat. Mater.* **2005**, *14*, 1932-1935.

53. C. A. McLellan B. A. Myers, S. Kraemer, K. Ohno, D. D. Awschalom, A. C. Bleszynski Jayich, *Nano. Lett.* **2016**, *16*, 2450–2454.

54. S. Pezzagna, D. Rogalla, H.-W. Becker, I. Jakobi, F. Dolde, B. Naydenov, J. Wrachtrup, F. Jelezko, C. Trautmann, J. Meijer, *Phys. Status Solidi A* **2011**, *208*, 2017–2022.

55. Y.-C. Chen, P. S. Salter, S. Knauer, L. Weng, A. C. Frangeskou, C. J. Stephen, S. N. Ishmael, P. R. Dolan, S. Johnson, B. L. Green, G. W. Morley, M. E. Newton, J. G. Rarity, M. J. Booth, J. M. Smith, *Nat. Photonics* **2017**, *11*, 77–80

56. K. Thonke, *Semicond. Sci. Technol.* **2003**, *18*, S20-S26.

57. W. Kaiser, W. L. Bond, *Phys. Rev.* **1959**, *115*, 857.

58. M W. Doherty, N. B. Manson, P. Delaney, F. Jelezko, J. Wrachtrup, L. C. Hollenberg, *Phys. Rep.* **2013**, *528*, 1–45.

59. J. P. Goss, R. Jones, S. J. Bereuer, P. R. Briddon, S. Öberg, *Phys. Rev. Lett.* **1996**, *77*, 3041-3044.

60. A. T. Collins, *Diam. Relat. Mater.* **2003**, *12*, 1976-1983.

61. J. E. Shigley, C. M. Breeding, *Gems Gemol.* **2013**, *49*, 107-111.

62. M. N. R. Ashfold, J. P. Goss, B. L. Green, P. W. May, M. E. Newton, C. V. Peaker, *Chem. Rev.* **2020**, *120*, 5745-5794.

63. J. Walker, *Rep. Prog. Phys.* **1979**, *42*, 1605-1659.

64. C. M. Breeding, J. E. Shigley, *Gems Gemol.* **2009**, *45*, 96–111.

65. S. A. Kajihara, A. Antonelli, J. Bernholc, R. Car, *Phys. Rev. Lett.* **1991**, *66*, 2010-2013.

66. F. Jelezko, J. Wrachtrup, *Phys. Status Solidi A* **2006**, *203*, 3207–3225.

67. D. D. Awschalom, R. Hanson, J. Wrachtrup, B. B. Zhou, *Nat. Photonics* **2018**, *12*, 516–527.

68. I. Kiflawi, A. E. Mayer, P. M. Spear, J. A. Van Wyk, G. S. Woods, *Philos. Mag. B* **1994**, *69*, 1141-1147.

69. S. R. Boyd, I. Kiflawi, G. S. Woods, *Philos. Mag. B* **1995**, *72*, 351-361.

70. C. Glover, M. E. Newton, P. M. Martineau, S. Quinn, D. J. Twitchen, *Phys. Rev. Lett.* **2004**, *92*, 135502.

71. C. Glover, M. E. Newton, P. M. Martineau, D. J. Twitchen, J. M. Baker, *Phys. Rev. Lett.* **2003**, *90*, 185507.

72. F. Maier, M. Riedel, B. Mantel, J. Ristein, L. Ley, *Phys. Rev. Lett.* **2000**, *85*, 3472-3475.

73. R. U. A. Khan, B. L. Cann, P. M. Martineau, J. Samartseva, J. J. P. Freeth, S. J. Sibley, C. B. Hartland, M. E. Newton, H. K. Dhillon, D. J. Twitchen, *J. Phys. Condens. Matter* **2013**, *25*, 275801.

74. R. U. A. Khan, P. M. Martineau, B. L. Cann, M. E. Newton, D. J. Twitchen, *J. Phys. Condens. Matter* **2009**, *21*, 364214.

75. J. P. Goss, P. R. Briddon, V. Hill, R. Jones, M. J. Rayson, *J. Phys. Condens. Matter* **2014**, *26*, 145801.

76. P. R. W. Hudson, I. S. T. Tsong, *J. Mater. Sci.* **1977**, *12*, 2389−2395.

77. E. Sideras-Haddad, S. E. Connell, J. P. F. Sellschop, I. Z. Machi, D. Rebuli, R. D. Maclear, D. P. Doyle, *Nucl. Instrum. Methods Phys. Res. Sect. B* **2001**, *181*, 419−425.

78. K. Iakoubovskii, G. J. Adriaenssens, *Diam. Relat. Mater.* **2002**, *11*, 125–131.

79. C. Van Der Bogert, C. Smith, T. Hainschwang, S. McClure, *Gems Gemol.* **2009**, 45, 20-79.

80. D. F. Swinehart, *J. Chem. Educ.* **1962**, *39*, 333-335.

81. C. D. Clark, P. J. Dean, P. V. Harris, *Proc. Roy. Soc. Lond. A* **1964**, *277*, 312-329.

82. J. L. Warren, J. L. Yarnell, G. Dolling, R. A. Cowley, *Phys. Rev.* **1967**, *158*, 805-808.

83. X. Gonze, G.-M. Rignanese, R. Caracas, *Z. Kristallogr.* **2005** *220*, 458–472.

84. R. P. Mildren, J. R. Rabeau, *Optical Engineering of Diamond, 1st Edition*, Wiley: USA, **2013**, 1-34.

85. M .D. McCluskey, *J. Appl. Phys.* **2000**, *87*, 3593-3617.

86. J. J. Charette, *Physica* **1959**, *25*, 1303–1312.

87. G. Herzberg, *Molecular Spectra and Molecular Structure. II. Infrared and Raman Spectra of Polyatomic Molecules.* Van Nostrand: USA, **1990**.

88. J.-K. Wang, C.-S. Tsai, C.-E. Lin, J.-C. Lin. *J. Chem. Phys.* **2000**, *113*, 5041-5052.

89. E. B. Wilson, J. C. Decius, P. C. Cross, *Molecular vibrations : the theory of infrared and Raman vibrational spectra*; Dover Publications: USA, **2003**.

90. F. De Weerdt, Y. N. Pal'yanov, A. T. Collins, *J. Phys. Condens. Matter* **2003**, *15*, 3163–3170.

2 Experimental and theoretical method

In this section, the experimental techniques and theoretical models used in this work are detailed, alongside information about each of the diamond samples that were studied.

2.1 Fourier transform infrared (FTIR) spectroscopy

Fourier transform infrared (FTIR) spectroscopy is a steady-state technique used to collect absorption spectra in the infrared (IR) range. IR radiation, usually in the wavenumber range 10-12800 cm^{-1}, is passed through a sample before detection. The resulting spectrum of signal against wavenumber can be analysed for spectral features produced by the absorption of light of specific wavelengths. Since a local vibrational mode (LVM) associated with a solid-state defect has a resonant frequency similar to that of IR light, it absorbs the radiation. This manifests as an absorption feature in the IR spectrum. In reality, these features are measuring the difference between absorption and stimulated emission, where light interacting with a sample causes more light to be emitted. However, in the range we are particularly interested in (1000-6000 cm^{-1}), the level of stimulated emission is low. Additionally, due to the low light intensity used in FTIR measurements, the resulting spectra are usually unsaturated. Absorption features can therefore be used to calibrate between the concentration of a species responsible for a spectral line and the intensity of its line. FTIR spectroscopy has been greatly used in the past to detect the presence of vibrational modes attributed to impurities in diamond [**1-11**].

The key component of an FTIR spectrometer is the Michelson interferometer, shown in Figure 2.1 [**12-13**]. Broadband IR radiation strikes a beamsplitter, where it is split evenly between two paths. Each component is directed towards a mirror at a zero degree angle of incidence. The two beams are both reflected back onto the beamsplitter and recombined before passing through the sample. During this process, one, moveable mirror translates at a constant velocity, changing its position relative to the beamsplitter. This creates an optical path difference (OPD) between the two beams [**14-15**]. As they arrive at the detector, summing the light from each beam together creates an interference pattern for intensity. A plot of this intensity against OPD is known as an interferogram. The intensity peaks at zero path difference (ZPD), where the two beams constructively interfere with one another. As the OPD increases in either direction, the beams begin to destructively interfere, and the intensity reduces. An interferogram is taken once before (the background) and once after the sample is inserted, and each is subsequently Fourier transformed to produce an absorption spectrum. Subtracting the sample spectrum from the background thus yields the overall IR spectrum of the sample.

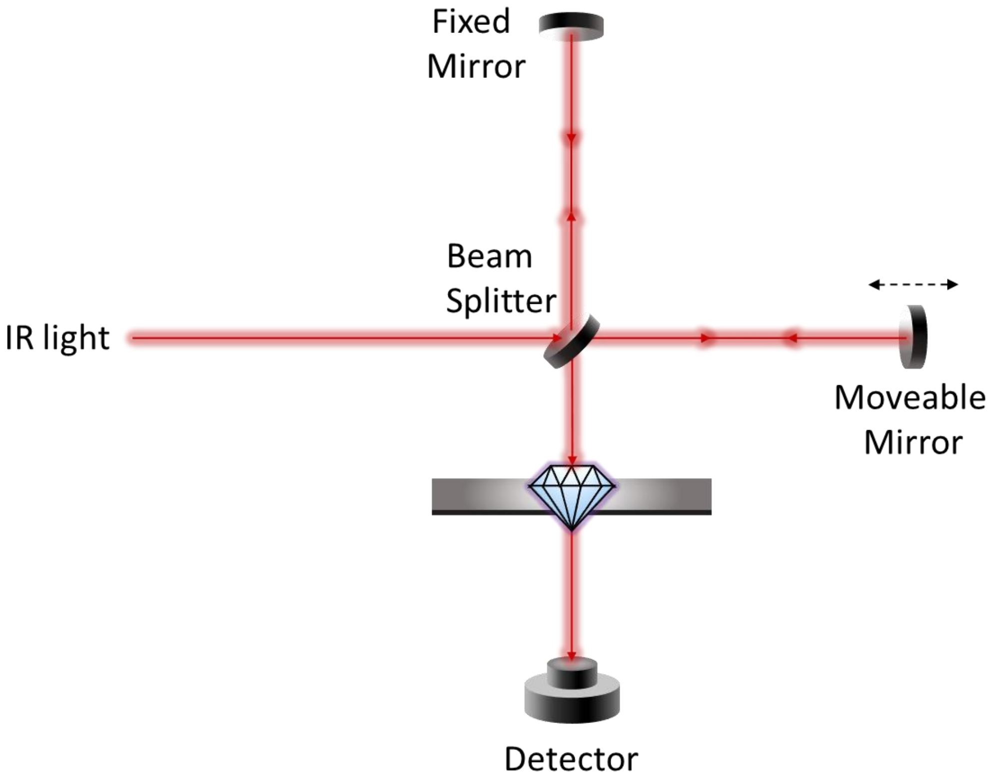

Figure 2.1 Schematic representation of a Michelson interferometer, the primary component of an FTIR spectrometer.

Using an FTIR spectrometer provides advantages over a dispersive IR spectrometer [**16-17**]. These are: (1) The Fellgett or multiplex advantage – all the wavenumbers of light are measured at the same time, which enables a quicker scan time; (2) The Jacquinot or throughput advantage – the lack of slits being used for entrance and exit of the beam means that light has a higher energy throughput, resulting in an improved signal to noise ratio of between 10-100 times, when directly compared with other IR techniques [**18**]; and (3) The precision advantage – the wavenumber scale of the spectrometer is calibrated by using a reference laser beam of known wavenumber, giving improved precision over dispersive spectrometers.

A Perkin Elmer Spectrum GX FTIR spectrometer was used to obtain FTIR spectra at room temperature. For measurements at 100 K and 10 K, a Bruker IFS66 FTIR spectrometer was used instead, so that the samples could be mounted inside an Oxford Instruments MicroStatHe, subsequently placed in the sample compartment. For these cryogenic measurements, temperature control was achieved using an Oxford Instruments ITC503. For both FTIR spectrometers, the spectral resolution was set to 0.25 cm^{-1}. Calibration of the signal to an absorption coefficient value was achieved by setting the absorption coefficient of diamond at a wavenumber of 2000 cm^{-1} to its known literature value (12.3 cm^{-1}) [**19**]. The room temperature FTIR spectra scanned a wavenumber range between 370 and 7800 cm^{-1}. Absorption of the crystalline quartz windows of the MicroStatHe limited the spectral window to the 3000–3500 cm^{-1} range for the cryogenic experiments. Detection of light was achieved using a conventional deuterated triglycine sulfate (DGTS) detector.

2.2 Ultraviolet/visible (UV/Vis) spectroscopy

Ultraviolet/visible (UV/Vis) spectroscopy is a steady-state technique, used to obtain spectra of samples in the ultraviolet (UV) or visible (Vis) range, 100-700 nm or 12800-100000 cm^{-1}. Many diamond defects produce features in this region, as their electronic states exist in the diamond band gap (above 225 nm) [**9, 20-25**]. The operation of a dispersive UV spectrophotometer can be simplified to the following key components, shown in Figure 2.2 [**26**]. Broadband light, sourced from a lamp, is diverted into a monochromator, which collects and spreads out light using a diffraction grating. A specific wavelength is selected for using a slit that adjusts during the scan, allowing data to be collected for each wavelength in turn. Light then proceeds to the sample compartment, to be absorbed or transmitted by the sample, before detection. Signal is recorded for each wavelength and the data is compiled together to create an overall spectrum.

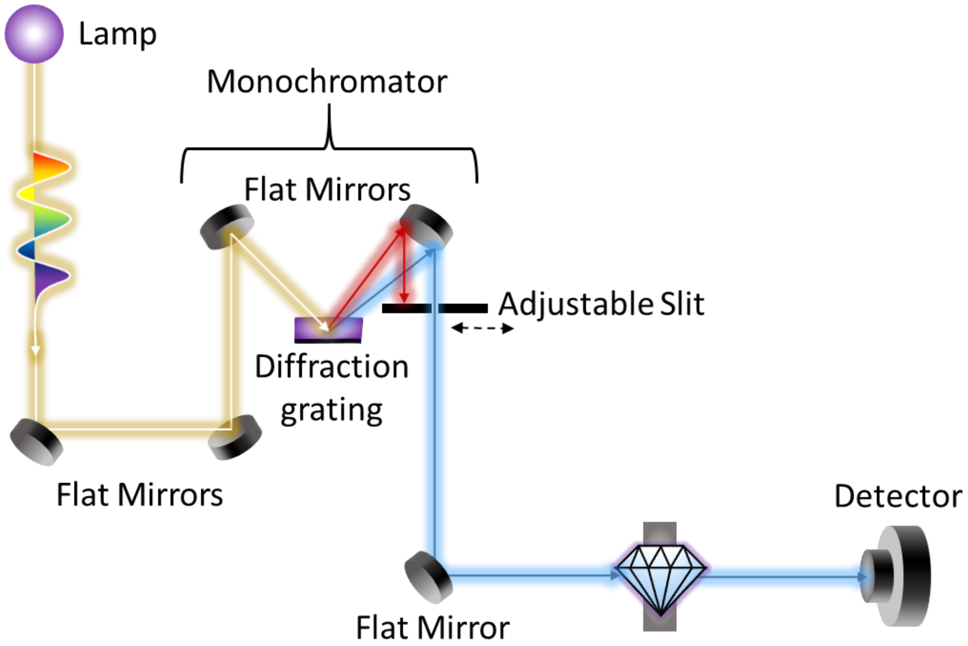

Figure 2.2 Schematic representation of the key components of a dispersive UV/Vis spectrophotometer.

A Perkin Elmer Lambda 1050 spectrophotometer was used to record spectra in the wavelength range λ = 200-850 nm, at a spectral resolution of 0.5 nm. This spectrophotometer included several extra optics that increase both its overall performance and the quality of spectra it generates. It contained a second monochromator to ensure minimalisation of stray light reaching through to the sample compartment. Additionally, a common beam depolariser corrected for depolarisation inherent to the instrument itself, and a common beam mask was used for precise adjustment of the beam height relative to samples of different sizes. An indium gallium arsenide (InGaAs) detector received the light after it had passed through the sample.

2.3 Transient vibrational absorption spectroscopy (TVAS)

Transient vibrational absorption spectroscopy (TVAS) is an ultrafast pump-probe technique that detects the differences in vibrational absorption created following IR photoexcitation, at different snapshots in time [**27**]. Two beams, the pump and probe, are required for a TVAS experiment. The travel distance of the probe beam is varied for each measurement, allowing snapshots to be taken of the system at various times (typically in steps of 100 fs close to the time-zero, and longer timesteps thereafter up to times ~1000 ps) after excitation. The appearance and subsequent relaxation of absorption features is observed, allowing lifetimes to be recorded, and the dynamics of corresponding vibrational modes to be mapped out. TVAS has previously been employed for the study of solid-state defects [**28-33**].

For TVAS, the individual pump and probe beams were firstly created from the originating laser pulses. A MKS Newport-SpectraPhysics MaiTai SP Ti:sapphire laser was used to produce a pulse train of wavelength λ = 800 nm (84 MHz repetition rate, average power >400 mW), with horizontal polarisation. One pulse in every 84000 was subsequently amplified (the repetition rate of the main, amplified output at 1 kHz, see below) by two regenerative amplification stages within a Spitfire ACE. Each amplification stage is pumped by an Ascend laser (527 nm light, 1 kHz repetition rate, average power $P > 35$ W). This produced 800 nm laser pulses, at a repetition rate of 1 kHz and a pulse duration of < 40 fs, and an average power P of > 13 W. Two portions of this beam were used to pump two tuneable optical parametric amplification systems (TOPASs), creating IR pulses with peak wavenumber ω tuneable in the range 700-10000 cm^{-1}, and a pulse spectral bandwidth of roughly 500 cm^{-1}. A third portion was used to pump another TOPAS to create UV pulses with peak wavenumber tuneable in the spectral range 235–1600 nm. These different pulses are then fed into the TVAS experimental setup.

The IR pump pulse ($\lambda = 3219$ or 3090 nm, $\omega = 3107$ or 3237 cm^{-1}, $P = 1.56$ mW, diameter of beam at focus = 370 µm, fluence = 1.44 mJ cm^{-2}) first enters a homebuilt pulse shaper to be spectrally narrowed. The pulse shaper setup spreads out the IR pump pulse using a diffraction grating (3.5 µm blaze, 300 lines mm^{-1} resolution). Light is then collimated through an adjustable slit onto a flat mirror. This reflects light back down the optical line into the lens, which refocuses light back onto the grating, to be re-collimated. The overall effect of the pulse shaper is to spectrally narrow the IR pump to a reduced bandwidth. This has the consequence of broadening out the pulse in time. As such, there is a tradeoff between reducing the bandwidth and keeping the pulse duration sufficiently short. Figure 2.3 shows how signal growth and decay are affected by a reduced bandwidth. A spectral bandwidth of 250 cm^{-1} is selected to ensure that the pulse is sufficiently short in time to capture the dynamics, whilst only photoexciting one vibrational mode associated with a single defect.

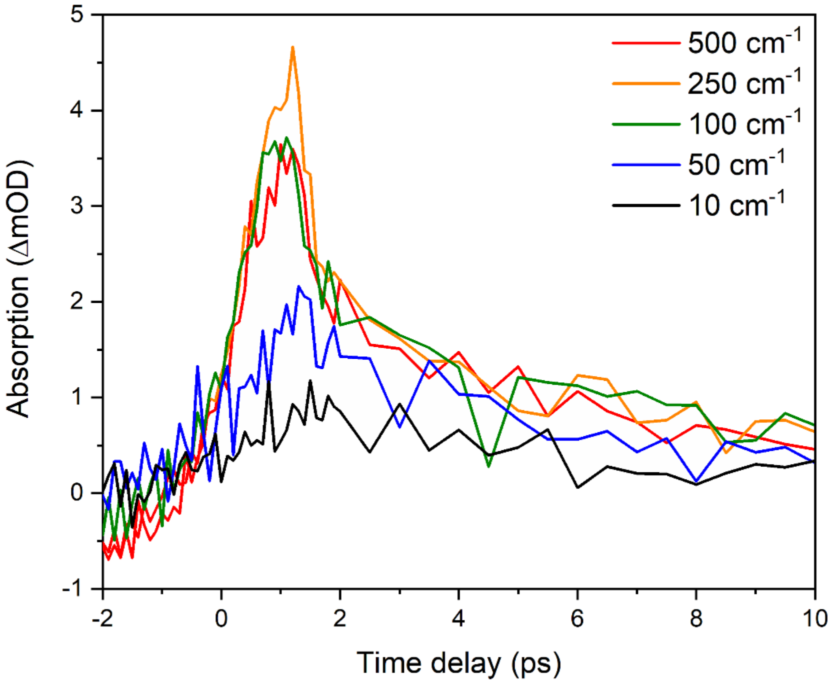

Figure 2.3 Transient fits of TVAS data, pumping and probing at 3107 cm^{-1}, showing how the data changes as the bandwidth of the IR pump pulse is varied by narrowing the pulse shaper. The absorption difference is measured at the wavenumber of the peak maximum of the feature.

The UV pump pulse (λ = 240 nm, ω = 40,000 cm^{-1}, P = 3.0 mW, diameter of beam at focus = 560 µm, fluence = 1.22 mJ cm^{-2}) is passed through a neutral density filter to reduce its intensity and focused onto the sample by a lens. The spot size of the UV pulse is significantly larger than that of the IR pump in order to produce a similar overall fluence. The UV pulse has a spectral bandwidth of roughly 3 nm.

Before reaching the sample, the pump pulse passes through an optical chopper, rotating at 500 Hz to block every other pulse, allowing a direct comparison between signal detection of pumped and unpumped sample.

The IR probe pulse (λ = 3067-3425 nm,ω = 2920-3260 cm^{-1}, P = 0.78 mW, beam diameter at focus = 360 µm, fluence = 0.77 mJ cm^{-2}) is polarised at 90° to the pump to minimize interference between the two beams. A gold retro-reflector in the probe line is mounted on a moveable stage, in order to vary the time delay, Δt, between the two pulses over a 3.3 ns window, with a time resolution of 17 fs. The pulse is partitioned equally by a CaF_2 beamsplitter to a reference pulse and a probe pulse. The reference pulse does not pass through the sample. It is detected to subtract shot-to-shot laser noise. The probe pulse is focused down onto the sample using an off-axis parabolic (OAP) mirror and is subsequently recollimated using a second OAP mirror. For detection, probe light enters a HORIBA iHR320 imaging spectrometer, where it is dispersed by a diffraction grating (unless otherwise stated, a 4 µm blaze, 300 lines mm^{-1} resolution grating) onto a Mercury Cadmium Telluride (MCT) detector array. This detector (contained within an IR Systems Development FPAS-0144) contains two vertically offset 64-pixel linear arrays – one each for the probe and reference pulses. It is cooled using liquid nitrogen to eliminate thermal contributions. A Perkin Elmer mid-IR polystyrene reference card was used to calibrate pixel number to wavenumber.

A TVAS spectrum represents a difference in optical density (ΔOD) between pump-off, $I_{pr}(\lambda, \infty)$, and pump-on signal, $I_{pr}(\lambda, \Delta t)$, at time Δt [**34**]. This change in optical density is measured as:

$$\Delta OD = \log_{10}\left(\frac{I_{pr}(\lambda, \infty)}{I_{pr}(\lambda, \Delta t)} \frac{I_{ref}(\lambda, \Delta t)}{I_{ref}(\lambda, \infty)}\right) \tag{2.1}$$

where $I_{ref}(\lambda, \infty)$ denotes the reference signal measured during pump-off and $I_{ref}(\lambda, \Delta t)$ is the reference signal measured during pump-on, at time Δt. The most common causes of a change in optical density arise due to: (1) A reduction in the ground state population, meaning less light resonant with transitions from the ground state is now absorbed. This manifests as a negative feature, known as a ground state bleach (GSB); (2) A new population in an excited state, meaning light resonant with transitions from this state can now be absorbed. This manifests as an excited state absorption (ESA). As each measurement is a snapshot of the state of the system Δt before or after pump excitation, the appearance of these features can be observed, along with their decay as the system relaxes back to equilibrium at long times after excitation.

The TVAS experimental setup is shown in Figure 2.4. The UV and IR pump beams are both shown alongside the IR probe, though the two pump beams are never used simultaneously.

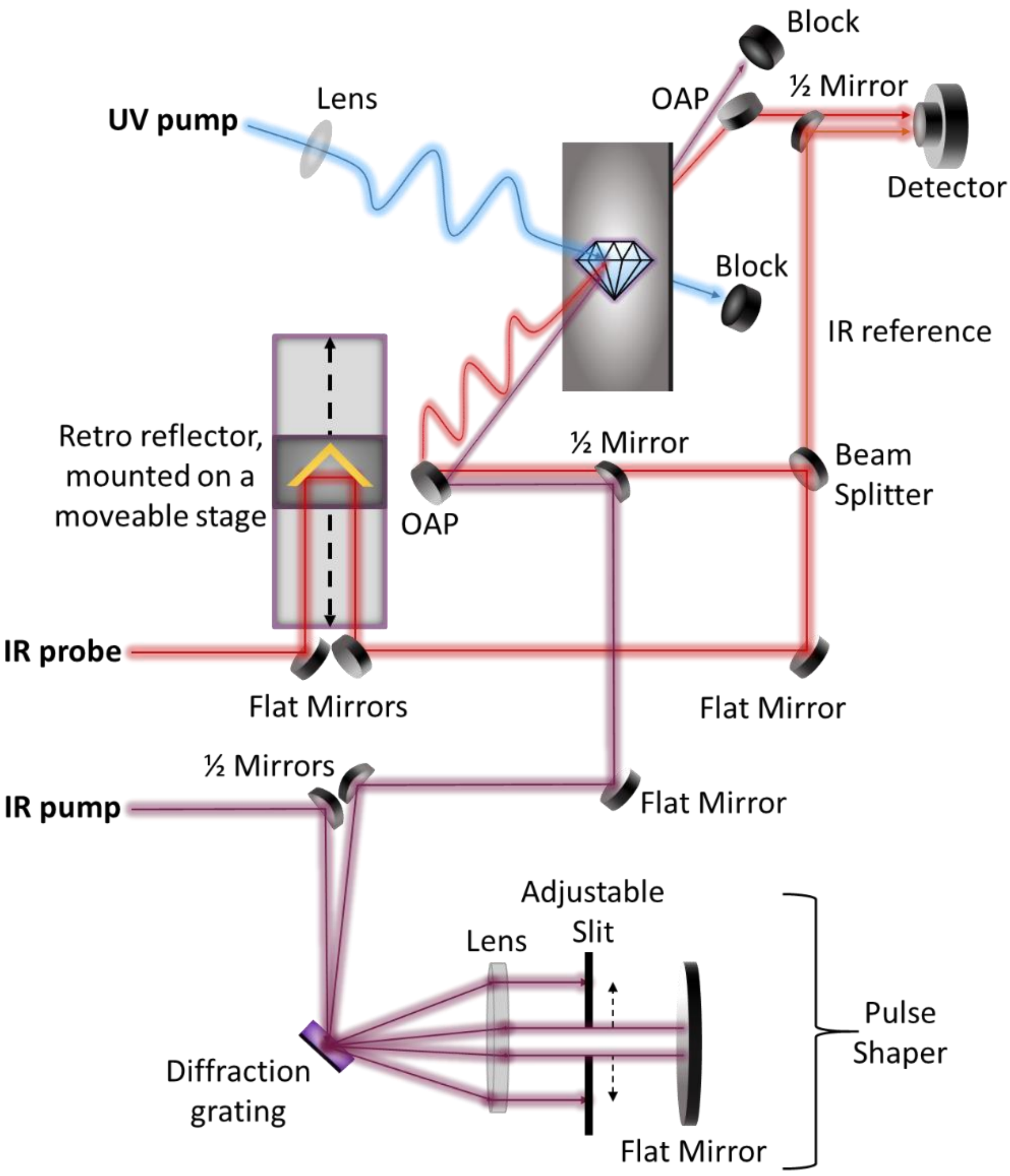

Figure 2.4 Schematic representation of the TVAS experimental setup, including the IR pump, UV pump and IR probe beams.

2.4 Sample details

Several different diamond samples, shown in Figure 2.5, were used throughout these studies. Each of these samples were chosen for their high intensity IR features. Their monikers, N or S, denote their origin, natural or synthetic. Natural samples N1, N2 and N3 originated from the Argyle mine in Australia, where diamonds are typically rich in N_3VH^0 [**35**]. Samples N2 and N3 showed a violet coloration, which is commonly associated with diamonds high in hydrogen content found in this region. Natural samples N4 and N5 were supplied by De Beers Group Technology. N4 had been subjected to annealing at 2000 °C to grow in N_3VH^0. Synthetic sample S1, obtained from the MIT Lincoln Laboratory, was initially grown by CVD and subsequently HPHT annealed for 30 minutes at a temperature of 2200 °C and a pressure of 6.6 GPa**.** It forms part of a series of annealed samples, showing the growing in of N_3VH^0 through its IR feature at 3107 cm^{-1} (see Figure 2.6).

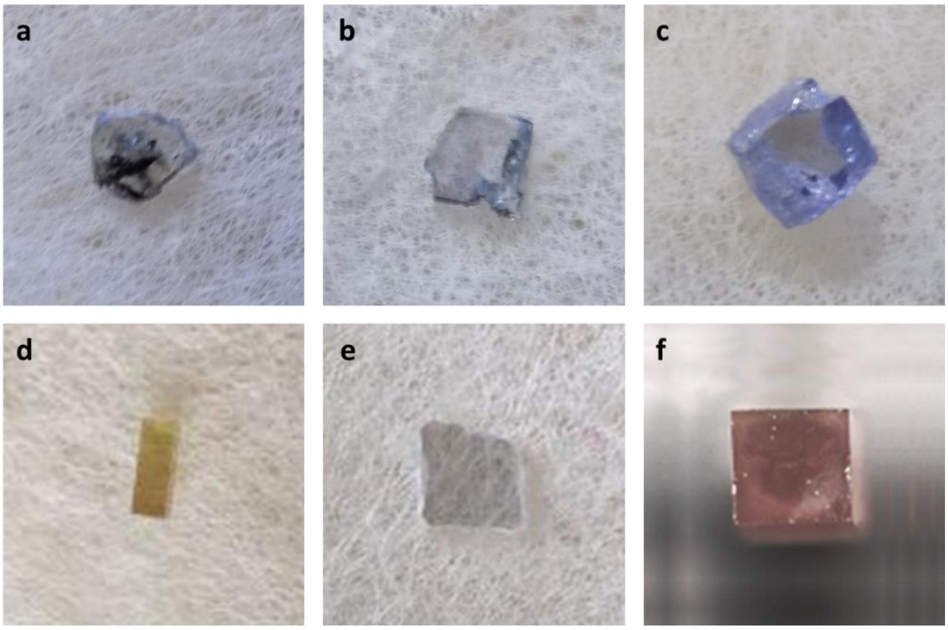

Figure 2.5 Not-to-scale images of the diamond samples **a,** N1 **b,** N2 **c,** N3 **d,** N4 **e,** N5 **f,** S1.

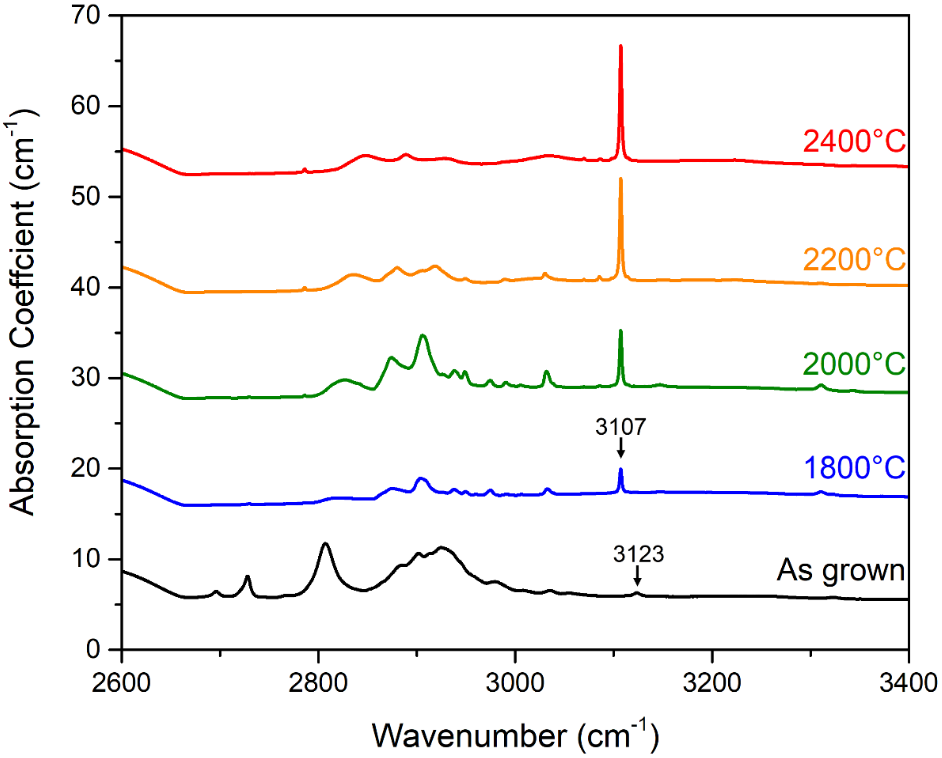

Figure 2.6 IR spectra of the C–H stretch region for a suite of CVD grown samples, from which sample S1 (annealed at 2200°C) was taken. Each diamond, except for the as grown sample, was subjected to 30 minutes of HPHT annealing, at 6.6 GPa and its denoted temperature. The spectra were taken at room temperature and are offset for clarity.

In the setup, a sample is mounted over a small hole in a metal plate, which slides into a mount attached a stage with X, Y and Z control. A simplified version of the sample compartment is shown in Figure 2.7. The sample is oriented with the overlapping pump and probe beams perpendicular to the (100) face, facilitating absorption from both the stretch and bend modes.

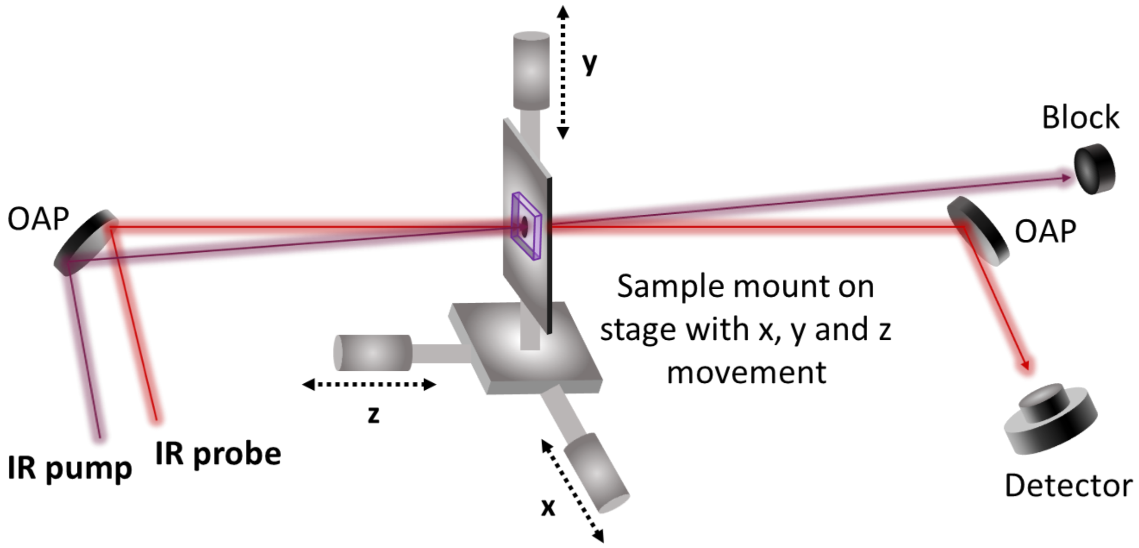

Figure 2.7 Schematic representation of the sample compartment as used for IR pump – IR probe TVAS experiments, showing the X, Y and Z control and the orientation of the diamond sample with respect to the pump and probe beams.

Each sample contained different concentrations of defects. Those most prevalent include the A- and B-nitrogen centres, which manifest features in the region of 500-1500 cm^{-1}. Known calibrations between the absorption intensity and shape of features in the FTIR were used to determine concentrations, $[\mathrm{N}]_A$ and $[\mathrm{N}]_B$, for both defects in each diamond sample [**36-38**]:

$$[\mathrm{N}]_A\ (\mathrm{ppb}) = (16.5 \pm 1) \times I_{1282}(\mathrm{cm}^{-2}) \tag{2.2}$$

$$[\mathrm{N}]_B\ (\mathrm{ppb}) = (79.4 \pm 8) \times I_{1280}(\mathrm{cm}^{-2}) \tag{2.3}$$

The results are shown in Table 2.1. Also included is the total nitrogen concentration from both defects, $[\mathrm{N}]_{A+B}$. This estimate for the total nitrogen concentration does not account for nitrogen present in other features, such as N_3VH^0, but does give a good indication of the amount of nitrogen present in each sample.

Table 2.1 The A- and B-nitrogen centre concentrations, $[\mathrm{N}]_A$ and $[\mathrm{N}]_B$, and their sum, $[\mathrm{N}]_{A+B}$, in each diamond sample, determined using known calibrations between FTIR peak intensity and defect concentration.

Sample	$[\mathbf{N}]_{\boldsymbol{A}}$ **(ppm)**	$[\mathbf{N}]_{\boldsymbol{B}}$ **(ppm)**	$[\mathbf{N}]_{\boldsymbol{A+B}}$ **(ppm)**
N1	11	42	53
N2	–	3106	3106
N3	–	2504	2504
N4	249	844	1093
N5	1300	–	1300
S1	–	–	–

2.5 Relating FTIR linewidth to TVAS lifetime

The FTIR linewidth, Γ, of an individual absorption peak provides some information about the excited state lifetime for population relaxation, T_1, since the following relationship exists between Γ and the total dephasing lifetime, T_2, which includes T_1:

$$\Gamma = \frac{1}{T_2} = \frac{1}{2\pi T_1} + \frac{1}{\pi T_2^*} + \Gamma_{\mathrm{in}} \tag{2.4}$$

This linewidth also contains contributions from pure dephasing, T_2^*, and inhomogeneous broadening, Γ_{in}; hence T_1 is difficult to extract from an FTIR spectrum. A Voigt fit of an individual absorption feature in FTIR may be used to separate the homogeneous linewidth, $\Gamma_{Lorentz}$, which is the Lorentzian component of the fit, from the inhomogeneous linewidth, Γ_{in}:

$$\Gamma = \Gamma_{Lorentz} + \Gamma_{\text{in}} \tag{2.5}$$

However, contributions from both T_1 and T_2^* are still present in $\Gamma_{Lorentz}$. Using the excited state lifetime for population relaxation, T_1, as derived from TVAS, an estimate can be derived for the FTIR linewidth of an individual absorption peak. This value, Γ_{TVAS}, only considers contributions from T_1. This enables a comparison with the Lorentzian component of the linewidth, $\Gamma_{Lorentz}$, for the LVM, which includes components from T_1 and T_2^*, and demonstrates the amount of pure dephasing taking place:

$$\Gamma_{Lorentz} = \Gamma_{TVAS} + \frac{1}{\pi T_2^*} \tag{2.6}$$

By determining $\Gamma_{Lorentz}$ and Γ_{TVAS}, all three components of the total FTIR linewidth, Γ, can be isolated. To derive Γ_{TVAS}, a weighted-average estimate of the excited state lifetime, T_{av}, is taken, using the lifetimes obtained from a multi-exponential fit of the ESA feature corresponding to the LVM. Example fits can be seen in Figures 3.4 and 4.4, and their data is recorded in Tables 3.2 and 4.1. Γ_{TVAS} is thus determined according to the following equation:

$$T_{av} = \frac{A_1\tau_1 + A_2\tau_2 + \dots A_{\text{n}}\tau_{\text{n}}}{(A_1 + A_2 + \dots A_{\text{n}})} \tag{2.7}$$

where A_X represents the amplitude, and τ_X the lifetime, of the exponential fit *X*. Subsequent derivation of Γ_{TVAS} is achieved using the following equation:

$$\Gamma_{TVAS} = \frac{1}{2\pi T_{av}} \tag{2.8}$$

2.6 Morse potential modelling

The potential energy surface of a LVM, such as a C–H bond, can be modelled analytically by solving the Schrödinger equation for each vibrational state. In the case of an anharmonic potential energy function, $V(r)$, the Morse potential can be adopted [**39**]. It follows that:

$$V(r) = D_e(1 - e^{-a(r-r_e)})^2 \tag{2.9}$$

where D_e is the depth of the potential well, a is the inverse width of the well, r is the distance between the two atoms involved in the bond responsible for the LVM, and r_e is the equilibrium position. The solution to the Schrödinger equation for the vibrational states $n = 0, 1, 2$ ... gives the following quantised energy levels:

$$E_n = E_0(n + 1/2) - \frac{E_0^2(n + 1/2)^2}{4D_e} \tag{2.10}$$

where E_0 is the zero-point energy, the energy of the ground vibrational state. D_e and a can be calculated from the experimentally determined spacing between energy levels using the following equations:

$$D_e = \frac{(2E_{10} - E_{21})^2}{2(E_{10} - E_{21})} \tag{2.11}$$

$$a = \frac{E_0}{\hbar}\sqrt{\frac{\mu}{2D_e}} \tag{2.12}$$

where μ is the reduced mass of the atoms involved in the bonding in the LVM and E_{ij} is the energy difference between the i^{th} and j^{th} energy levels.

The solution of the Schrödinger equation determines the wavefunctions, ψ_n, of each of the vibrational states. These can be expressed with the following dimensionless coordinates, z:

$$z = 2\lambda e^{-(x-x_e)} \tag{2.13}$$

where $x = ar$, $x_e = ar_e$ and $\lambda = \sqrt{2\mu D_e}/(a\hbar)$. For each of the vibrational states, increasing from $n = 0, 1, 2 \ldots [\lambda -]$, the wavefunctions can be defined as:

$$\psi_n(z) = N_n z^{\alpha/2} e^{-z/2} L_n^{(\alpha)}(z) \tag{2.14}$$

where $\alpha = 2\lambda - 2n - 1$, $L_n^{(\alpha)}(z)$ are the generalised Laguerre polynomials, and N_n is a normalisation constant:

$$L_n^{(\alpha)}(z) = \frac{z^{-\alpha} e^{z}}{n!} \frac{\partial n}{\partial z^n} (z^{n+\alpha} e^{-z}) \tag{2.15}$$

$$N_n = \left(\frac{n!\, \alpha}{(2\lambda - n - 1)!} \right)^{1/2} \tag{2.16}$$

The wavefunctions, in terms of r, being normalised such that $\int_0^\infty \psi_n^*(r)\psi_n(r)dr = 1$, can be determined from:

$$\psi_n(r) = \sqrt{a}\psi_n(z) \tag{2.17}$$

The transition rate from the i^{th} to the j^{th} energy level was determined from Fermi's golden rule in the electric dipole approximation. It is proportional to D_{ij}^2, where:

$$D_{ij} = e\langle\psi_j|x|\psi_i\rangle/a \tag{2.18}$$

and the matrix element was determined analytically from

$$\langle\psi_j|x|\psi_i\rangle = \frac{2(-1)^{j-i+1}}{(j-i)(2N-i-j)}\sqrt{\frac{(N-i)(N-j)(2N-j+1)!\,j!}{(2N-i+1)!\,i!}} \tag{2.19}$$

where $j > i$ and $N = \lambda - \frac{1}{2}$.

For a two-level system, the absorption coefficient $a_{01}(\omega)$ for an optical transition from the ground state ($n = 0$) to the first excited state ($n = 1$), is [**40**]:

$$a_{01}(\omega) = \frac{D_{01}^2\omega}{n_{op}\hbar c\varepsilon_0}\frac{1/T_2}{(\omega-\omega_{01})^2 + (1/T_2)^2}(N_0 - N_1) \tag{2.20}$$

where D_{01} is the dipole matrix element for the 0th to 1st energy level transition, ω is the wavenumber of light, $(N_0 - N_1)$ is the population difference between the $n = 0$ and $n = 1$ energy levels, n_{op} is the refractive index of the optical medium, c is the speed of light, ε_0 is the vacuum permittivity, and ω_{01} is the angular frequency associated with an $n = 0$ to $n = 1$ transition. In equilibrium, the ground state concentration is the defect concentration, as thermal excitation of the 1st energy level is negligible. Thus, $N_0 = N_d$ and $N_1 = 0$. Using the yielded matrix element for D_{01} from the Morse potential model, this equation is fitted to the experimental absorption coefficient, yielding N_d, T_2 and ω_{01}. For the transient absorption case, the populations (N_0, N_1, N_2) for the three lowest states change from $(N_d, 0, 0)$ before photoexcitation has occurred to $(N_d - \delta N, \delta N, 0)$ immediately after photoexcitation. Therefore, the following amplitudes can be predicted for the absorption change in different levels:

$$\Delta\alpha_{01} = \alpha_{01}^{pump\ on} - \alpha_{01}^{pump\ off} \propto -2\ \delta N\ D_{01}^2 \tag{2.21}$$

$$\Delta\alpha_{12} \propto \delta N\ D_{12}^2 \tag{2.22}$$

Thus, the expected ratio of the amplitude of an ESA feature as it is observed in the TVAS spectrum ($\Delta\alpha_{12}$) can directly be compared to that of its related GSB ($\Delta\alpha_{01}$):

$$\frac{\Delta\alpha_{12}}{\Delta\alpha_{01}} = -\frac{D_{12}^2}{2\ D_{01}^2} \tag{2.23}$$

In a case where the matrix element D_{12} is a factor of $\sqrt{2}$ greater than D_{01}, $\frac{\Delta\alpha_{12}}{\Delta\alpha_{01}} = -1$. In other words, we would expect the ESA and GSB features of such a LVM to have the same amplitude of absorption. We apply this equation directly by comparing TVAS data to computed matrix elements in Sections 3.6 and 4.6.

2.7 References

1. J. J. Charette, *Physica* **1959**, *25*, 1303–1312.

2. W. Kaiser, W. L. Bond, *Phys. Rev.* **1959**, *115*, 857.

3. J. J. Charette, *J. Chem. Phys.* **1962**, *37*, 3014.

4. G. S. Woods, A. T. Collins, *J. Phys. Chem. Solids* **1983**, *44*, 471–475.

5. G. S. Woods, *Philos. Mag. B* **1984**, *50*, 673-688.

6. G. Davies, A. T. Collins, P. Spear, *Solid State Commun.* **1984**, *49*, 433–436.

7. K. M. McNamara, B. E. Williams, K. K. Gleason, B. E. Scruggs, *J. Appl. Phys*. **1994**, 76, 2466.

8. B. Rondeau, E. Fritsch, M. Guiraud, J. P. Chalain, F. Notari, *Diam. Relat. Mater.* **2004**, *13*, 1658–1673.

9. T. Hainschwang, F. Notari, E. Fritsch, L. Massi, *Diam. Relat. Mater.* **2006**, *15*, 1555–1564.

10. E. Fritsch, T. Hainschwang, L. Massi, B. Rondeau, *New Diam. Front. Carbon Technol.* **2007**, *17*, 63–89.

11. S. C. Kohn, L. Speich, C. B. Smith, G. P. Bulanova, *Lithos* **2016**, *265*, 148–158.

12. A. A. Michelson, *Philos. Mag.* **1891**, *31*, 256.

13. A. A. Michelson, *Light Waves and Their Uses*, University of Chicago Press: USA, **1902**.

14. P. R. Griffiths, J. A. de Haseth, *Fourier Transform Infrared Spectrometry, 2nd Edition*, Wiley: USA, **2007**, 19-26.

15. B. C. Smith, *Fundamentals of Fourier Transform Infrared Spectroscopy, 2nd Edition*, CRC Press, USA, **2011**, 19-36.

16. P. R. Griffiths, J. A. de Haseth, *Fourier Transform Infrared Spectrometry, 2nd Edition*, Wiley: USA, **2007**, 171-175.

17. B. C. Smith, *Fundamentals of Fourier Transform Infrared Spectroscopy, 2nd Edition*, CRC Press: USA, **2011**, 12-17.

18. P. R. Griffiths, H. J. Sloane, R. W. Hannah, *Appl. Spectrosc.* **1977**, *31*, 485.

19. E. D. Palik, *Handbook of Optical Constant of Solids*, Academic Press: USA, **1985**.

20. A. M. Zaitsev, *Phys. Rev. B* **1999**, *61*, 12909-12922.

21. A. T. Collins, *Diam. Relat. Mater.* **2003**, *12*, 1976–1983.

22. P. M. Martineau, S. C. Lawson, A. J. Taylor, S. J. Quinn, D. J. F. Evans, M. J. Crowder, *Gems Gemol.* **2004**, *40*, 2-25.

23. J. E. Shigley, C. M. Breeding, A. H. Shen, *Gems Gemol.* **2004**, *40*, 303-313.

24. S. Eaton-Magaña, J. E. Post, P. J. Heaney, R. A. Walters, C. M. Breeding, J. E. Butler, *Gems Gemol.* **2007**, *43*, 332-351.

25. E. Deljanin, A. De Stefano, *Diam. Relat. Mater.* **2008**, *17*, 1169-1178.

26. H. H. Perkampus, *UV-Vis Spectroscopy and Its Applications*, Springer: Germany, **1992**, 10-25.

27. R. Berera, R. van Grondelle, J. T. M. Kennis, *Photosynth. Res.* **2009**, *101*, 105-118.

28. M. Budde, G. Lüpke, C. Parks Cheney, N. H. Tolk, L. C. Feldman, *Phys. Rev. Lett.* **2000**, *85*, 1452–1455.

29. M. Budde, G. Lüpke, E. Chen, X. Zhang, N. H. Tolk, L. C. Feldman, E. Tarhan, A. K. Ramdas, M. Stavola, *Phys. Rev. Lett.* **2001**, *87*, 145501.

30. G. Lüpke, N. H. Tolk, L. C. Feldman, *J. Appl. Phys.* **2003**, *93*, 2317–2336.

31. R. Ulbricht, S. T. van der Post, J. P. Goss, P. R. Briddon, R. Jones, R. U. A. Khan, M. Bonn, *Phys. Rev. B* **2011**, *84*, 165202.

32. R. Ulbricht, S. Dong, A. Gali, S. Meng, Z.-H. Loh, *Phys. Rev. B* **2018**, *97*, 220302.

33. R. Ulbricht, Z.-H. Loh, *Phys. Rev. B* **2018**, *98*, 094309.

34. A. Maciejewski, R. Naskrecki, M. Lorenc, M. Ziolek, J. Karolczak, J. Kubicki, M. Matysiak, M. Szymanski, *J. Mol. Struct.* **2000**, *555*, 1-13.

35. K. Iakoubovskii, G. J. Adriaenssens, *Diam. Relat. Mater.* **2002**, *11*, 125–131.

36. S. R. Boyd, I. Kiflawi, G. S. Woods, *Philos. Mag. B* **1995**, *72*, 351-361.

37. I. Kiflawi, A. E. Mayer, P. M. Spear, J. A. Van Wyk, G. S. Woods, *Philos. Mag. B* **1994**, *69*, 1141-1147.

38. S. R. Boyd, I. Kiflawi, G. S. Woods, *Philos. Mag. B* **1994**, *69*, 1149-1153.

39. P. M. Morse, *Phys. Rev.* **1929**, *34*, 57-64.

40. E. Rosencher, B. Vinter, *Optoelectronics*, Cambridge University Press: UK, **2002**.

3 N_3VH^0 – the absorption feature at 3107 cm^{-1}

The work detailed in this chapter was presented in *J. Phys. Chem. Lett.* in July 2020 [**1**].

3.1 Background

The N_3VH^0 defect in diamond, shown in Figure 3.1, consists of a neutral vacancy where three nearest neighbour carbon atoms have been replaced with nitrogen and a hydrogen is bonded to the remaining carbon neighbour [**2**]. N_3VH^0 has C_{3V} symmetry, is charge neutral (there is no negatively charged acceptor state version, as all molecular orbitals are full) and has zero spin.

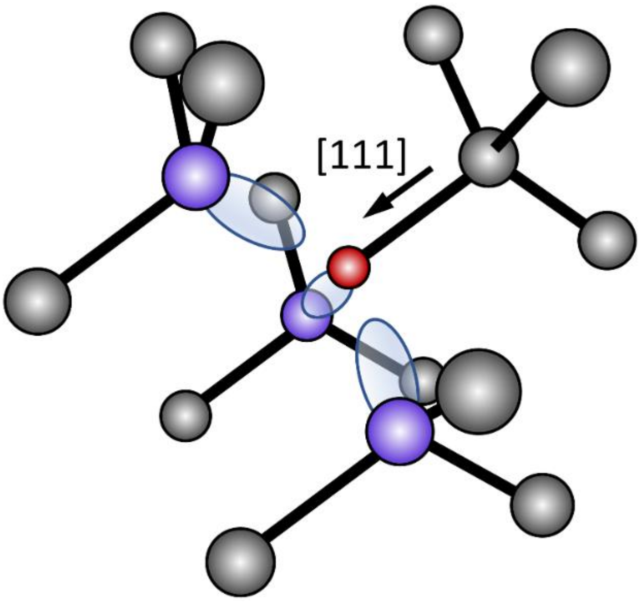

Figure 3.1 Structure of the N_3VH^0 defect. The C–H stretch is along the [111] direction. Grey, blue and red spheres represent C, N and H atoms, respectively.

N_3VH^0 is common in natural, type Ia diamond, where the intensity of the C–H stretch mode can exceed the intrinsic multi-phonon absorption in so called "hydrogen-rich" diamonds [**3**,**4**].

It is an excellent candidate for studying the growth history of natural diamonds [**5,6**]. N_3VH^0 can also be produced in both natural diamond and nitrogen doped laboratory-grown diamond by high pressure, high temperature (HPHT) annealing [**7-9**], even in material where no C–H stretch absorption was observed prior to annealing. N_3VH^0 is very stable and appears to be the end product of the defect aggregation process in nitrogen doped diamond grown by chemical vapour deposition (CVD). It may account for a substantial fraction of the total incorporated nitrogen and hydrogen in HPHT-annealed CVD diamond and thus its quantification is important for determining both the nitrogen and hydrogen concentrations in such material.

Due to the strength of its absorption features, N_3VH^0 has already been studied in detail in the frequency domain, which probes the time-averaged optical response. Many of its family of features were initially identified in the infrared (IR) spectra of natural diamonds by Charette [**10**]. Davies *et al.* subsequently found these features to correlate with each other and assigned many of them to stretch and bend modes of a C–H bond, and overtones and combinations thereof [**11,12**]. Studies on HPHT diamond grown from ^{13}C observed an isotopic shift of the stretch mode, confirming that the bond included carbon [**13**]. More recent theoretical studies have enabled a firm assignment of these features to the N_3VH^0 structure [**14,15**].

However, knowledge of the timescales or mechanisms for relaxation of the associated local vibrational modes (LVMs) of N_3VH^0 is sparse. The ultrafast “shakedown” of this defect’s vibrational dynamics following IR excitation of the C–H stretch mode (v_S = 3107 cm^{-1}) provides information about the energies of quantised vibrational states, and allows mapping out of the energy relaxation pathways, which include multi-phonon relaxation and anharmonic coupling to the C–H bend mode (v_B = 1405 cm^{-1}). Employment of this method offers a new route to quantification of impurities (in this case both nitrogen and hydrogen) incorporated into IR active defects, which is vital to the characterisation of diamond and feeds back into an understanding of synthesis, response to heat and pressure, and the incorporation of impurities.

3.2 Absorption in equilibrium

Different peaks in the IR absorbance spectra of hydrogen-rich diamonds, such as evident in Figure 3.2, have been attributed in the literature to different overtones and combinations of the stretch and bend modes of N_3VH^0 (Table 3.1) [**12,16**]. These modes have weak (but non-zero) matrix elements as a result of the anharmonicity of the potential energy. However, unique assignments of the rich vibrational spectra is challenging – in particular, it is difficult to isolate the overtones of C–H stretches when different defects are present. This is particularly clear in the 1000-1500 cm^{-1} range, which is dominated by nitrogen-related defect modes, specifically the B-nitrogen centre (N_4V^0).

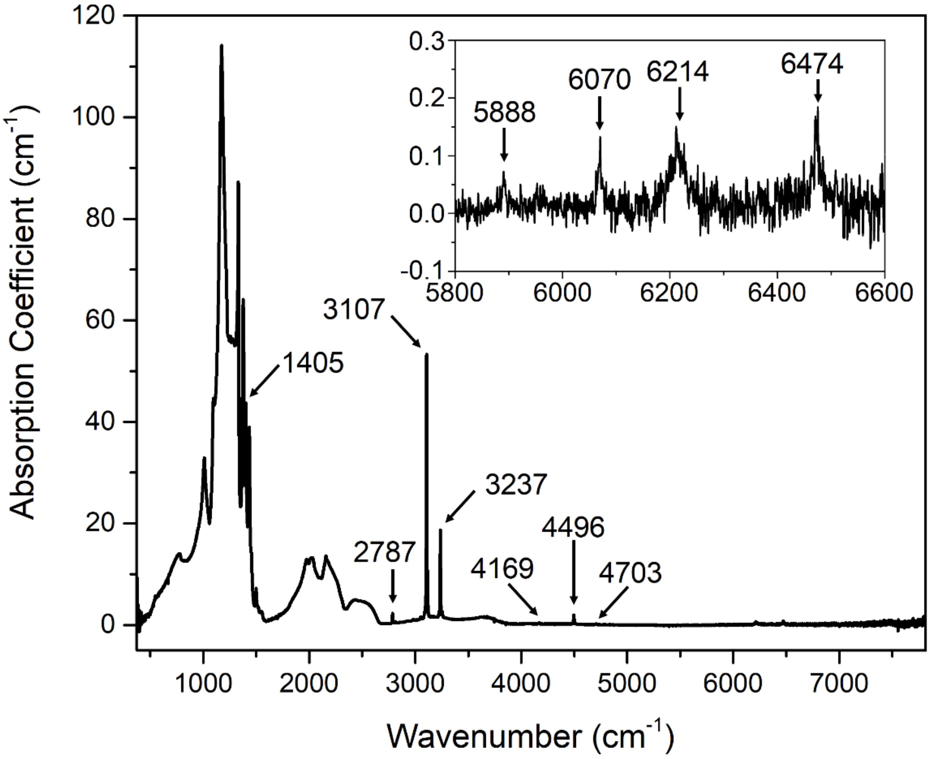

Figure 3.2 Fourier transform IR absorbance spectrum of N2, a hydrogen-rich natural diamond. Peaks at 6214 cm^{-1} and 6474 cm^{-1} (double 3107 cm^{-1} and 3237 cm^{-1}) correspond to photons that interacted with two defects in sequence. 3237 cm^{-1} is not associated with N_3VH^0.

Table 3.1 Vibrational features relating to N_3VH^0 observed in N2. The wavenumber of our observed IR absorption peaks ($\boldsymbol{\omega_{obs}}$) is compared to literature values ($\boldsymbol{\omega_{ref}}$) from [**9-13**].

N_3V:H mode	ω_{obs} (cm^{-1})	ω_{ref} (cm^{-1})	Symmetry Character
$\boldsymbol{v_B}$	1405	1405	E
$\boldsymbol{v_{2B}}$	2787	2786	$A_1 + E$
$\boldsymbol{v_S}$	3107	3107	A_1
$\boldsymbol{v_{3B}}$	4169	4169	$A_1 + A_2 + E$
$\boldsymbol{v_{S+B}}$	4496	4499	E
$\boldsymbol{v_{4B}}$	N/A	5555	$A_1 + 2E$
$\boldsymbol{v_{S+2B}}$	5888	5889	$A_1 + E$
$\boldsymbol{v_{2S}}$	6070	6070	A_1

We determined the symmetry character of each level according to the rules that were previously detailed in Section 1.5.3. The results are listed in Table 3.1. The symmetry character of each mode is important considering the excitation and relaxation dynamics, since coupling between two LVMs is only allowed if they have equivalent symmetry character. [**17-19**] The assignment to particular N_3VH^0 stretch and bend modes, and their combinations and overtones, are based on our IR absorption and transient absorption spectra, which will be discussed in the following section.

3.3 Transient absorption

To investigate the excited state dynamics of N_3VH^0, we used transient vibrational absorption spectroscopy (TVAS), a pump-probe technique that detects the differences in vibrational absorption created following IR photoexcitation. The photoexcitation pulse was resonant to the 3107 cm^{-1} (υ_S) LVM, with a spectral bandwidth that was narrowed (see Section 2.3) to avoid overlap with the nearby 3237 cm^{-1} LVM. The broadband probe was tuned either resonantly to υ_S or set to probe other spectral ranges (υ_{probe} = 2800-3300 cm^{-1}). The transient absorption spectra from sample N2 (see Section 2.4 for more details) are presented in Figure 3.3 at different pump-probe time delays, Δt.

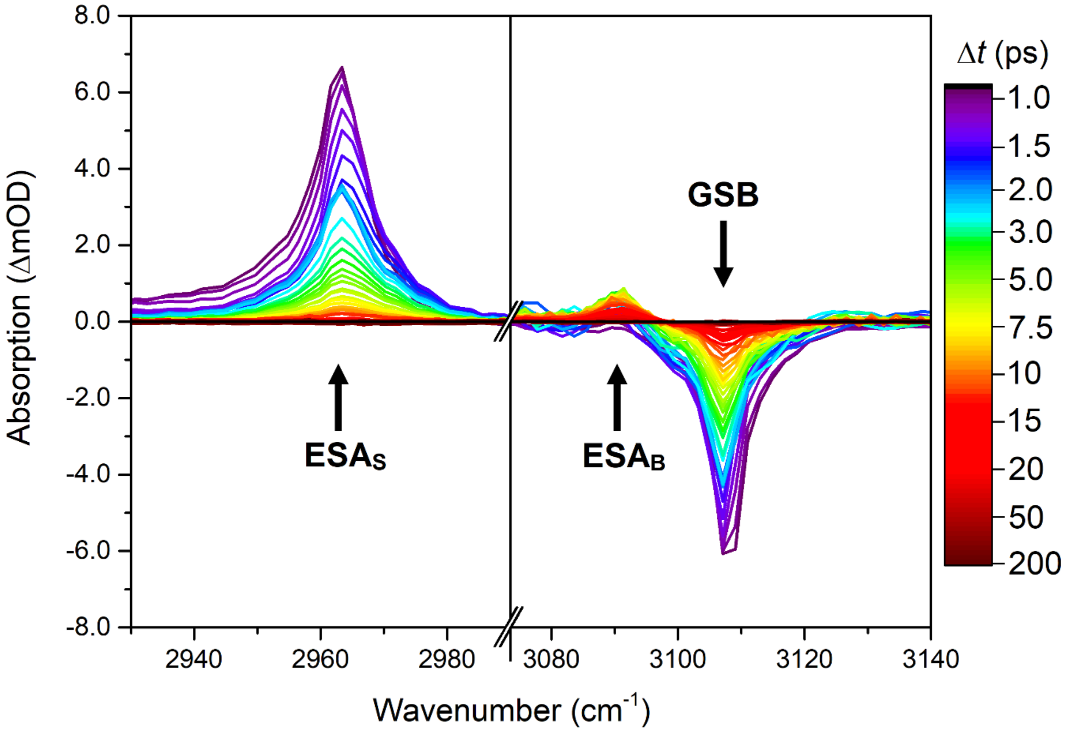

Figure 3.3 TVAS results for natural diamond N2. Transient absorption spectra for pump-probe delays 1 ps < Δt < 200 ps, for pump excitation centred at 3107 cm^{-1} and probed either around 2960 cm^{-1} (left) or 3107 cm^{-1} (right).

A ground state bleach (GSB) is clearly evident in the degenerate pump-probe spectrum (υ_{pump} = υ_{probe} = 3107 cm^{-1}), Figure 3.3 right. Centered at 3107 cm^{-1}, its negative sign indicates a reduction in the ground state population, N_0. A non-degenerate probe (Figure 3.3 left) reveals a strong excited state absorption (ESA) feature at 2963 cm^{-1}, labelled ESA$_S$. After the 3107 cm^{-1} pump pulse excites the stretch mode from the ground state to v_S, electric dipole-allowed absorption of the probe can occur from v_S to v_{2S}. The ESA$_S$ feature is observed at a reduced wavenumber when compared to the GSB. This is because the potential energy function along the C–H stretch is anharmonic. The quantised vibrational states have energies E_n, where $n = 0, 1, 2$ ..., and have a progressively smaller separation in energy between adjacent levels. The direct observation of ESA$_S$ between vibrational states 1 and 2 further allows the weak IR absorption feature at 6070 cm^{-1} (= 3107 + 2963) cm^{-1} (see Figure 3.2) to be uniquely assigned to the $n = 2 \leftarrow n = 0$ transition. The low absorption strength for this $\Delta n = 2$ transition is a direct consequence of its small matrix element, which is electric-dipole-forbidden for a harmonic potential. Thus $v_{2S} - v_S$ is measured as 2963 cm^{-1}.

Turning now to the vibrational dynamics, Figure 3.4a reports the modulus of the absorption change for the GSB and ESA$_S$ features versus pump-probe delay, as seen in natural diamond N2. The GSB transient shows a multi-component decay – an initial rapid decay followed by a second slower decay – with associated time-constants τ_1 and τ_2. A fuller treatment of this data, to extract time-constants for individual processes, is detailed in Section 3.7 below. Briefly, however, we attribute τ_1 to a fast energy transfer via the LVMs of the nitrogen atoms, or into the diamond lattice itself [**16**]. Notably, the dynamics evident in Figure 3.4a show that the decay lifetime of the ESA$_S$ feature (τ_2 = 3.3 ± 0.2 ps), indicative of the rate at which $n = 1$ is depopulated, is markedly shorter than the lifetime of the GSB (τ_2 = 6.2 ± 0.2 ps), which tracks the recovery of $n = 0$ (the ground-state absorption). This suggests that rather than a single decay channel from $n = 1$, a more complex decay pathway is required to understand the vibrational dynamics, involving at least one additional state coupled to $n = 1$. The presence of a weak excited state absorption feature at 3090 cm^{-1}, labelled ESA$_{B}$ in Figure 3.3, provides further evidence of an intermediate state that is critically involved in the relaxation pathway of the C–H stretch. Figure 3.4b shows that absorbance at ESA$_{B}$ is delayed (*cf.* ESA$_{S}$ which decays from Δt = 0), indicating an excited state that is populated from the initially populated v_S.

We note that the ESA$_{B}$ feature is unrelated to the ^{13}C–H isotope of the stretch mode. This is because: (1) ESA$_{B}$ is too intense in comparison to the GSB feature already reported; (2) We would expect to see a bleach rather than an absorption if it were an isotopic feature; (3) The ESA$_{B}$ feature appears later in time than the other features.

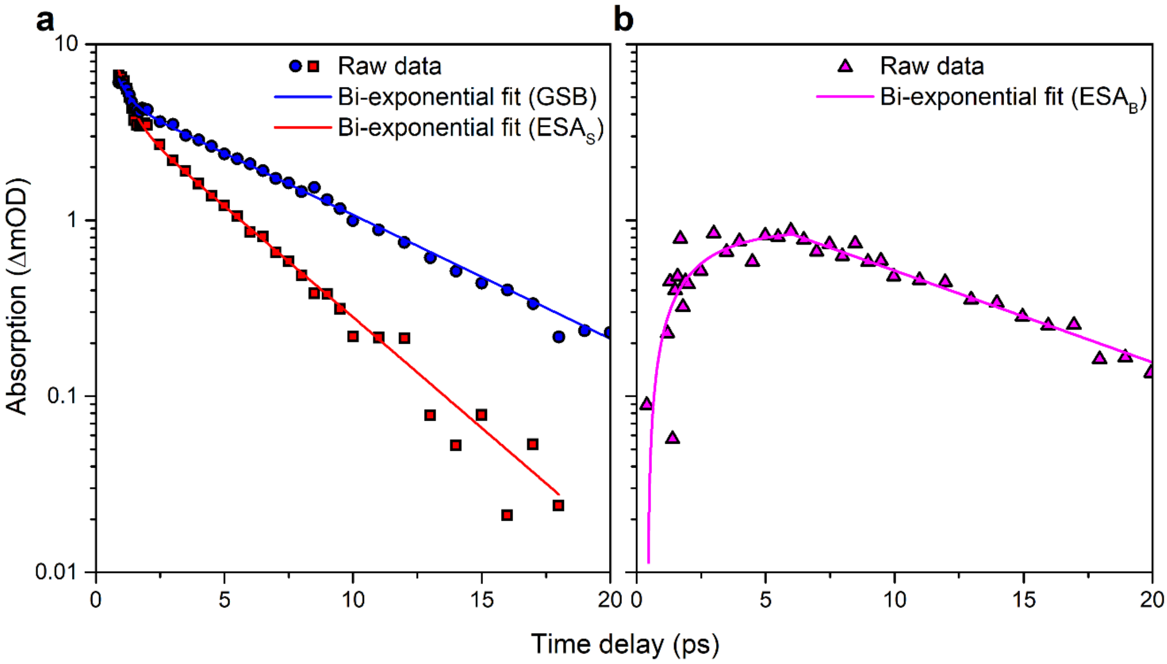

Figure 3.4 TVAS for natural diamond N2. **a,** Modulus of absorption difference for GSB (blue circles) and ESA$_{S}$ (red squares), measured at the wavenumber of their peak maxima, and bi-exponential fits (solid lines). **b,** Modulus of absorption difference for ESA$_{B}$ (magenta triangles), measured at the wavenumber of its peak maximum, and a bi-exponential fit (solid line).

Table 3.2 Decay lifetimes from peak height transient fits of data from the natural sample N2. All errors are standard errors, scaled by the square root of the reduced chi-squared value.

	$\boldsymbol{\omega}(\mathbf{cm^{-1}})$	A_1	$\boldsymbol{\tau_1}(\mathbf{ps})$	A_2	$\boldsymbol{\tau_2}(\mathbf{ps})$
GSB, 298 K	3107	1.6 (± 0.2)	0.44 (± 0.09)	4.7 (± 0.1)	6.2 (± 0.2)
$\mathbf{ESA_S}$, 298 K	2963	2.6 (± 0.2)	0.33 (± 0.06)	4.1 (± 0.2)	3.3 (± 0.2)
$\mathbf{ESA_B}$, 298 K	3090	–	–	0.8 (± 0.1)	8.4 (± 1.6)
GSB, 100 K	3107	1.0 (± 0.1)	0.76 (± 0.18)	1.1 (± 0.1)	12.2 (± 2.2)
$\mathbf{ESA_S}$, 100 K	2963	2.1 (± 0.3)	0.49 (± 0.11)	2.5 (± 0.3)	4.1 (± 0.5)
$\mathbf{ESA_B}$, 100K	3090	0.6 (± 0.2)	1.7 (± 1.4)	0.5 (± 0.1)	13.1 (± 3.1)

For comparison, Figure 3.5 shows identical transient plots of the integrated area of the three absorption features for each time delay. The data recorded from these integrated area plots is given in Table 3.3. There is no significant difference between the data based on peak height and that based on peak area. The lifetimes from both datasets are all within error of each other, and the absolute values of absorption are lower in the integrated area plots due to the inclusion of data over the whole peak, rather than taking the most intense wavenumber. The remainder of our fits were carried out using peak height, rather than integrated peak area.

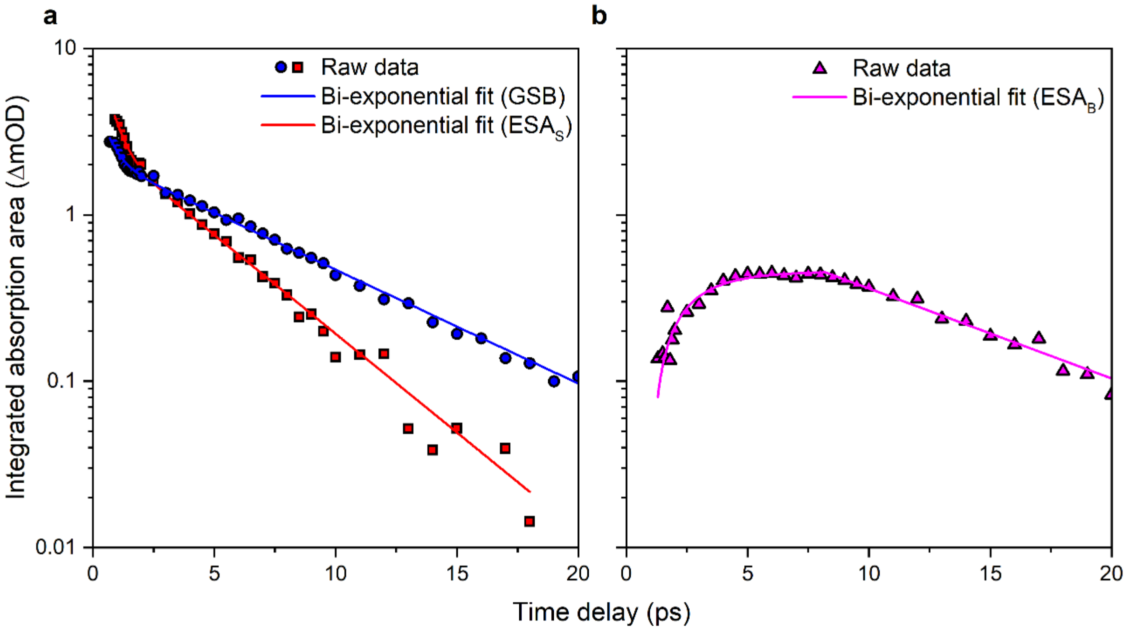

Figure 3.5 TVAS for natural diamond N2. **a,** The integrated absorption peak area for GSB (blue circles) and ESA$_S$ (red squares), and bi-exponential fits (solid lines). **b,** The integrated absorption peak area for ESA$_B$ (magenta triangles), and a bi-exponential fit (solid line).

Table 3.3 Decay lifetimes from integrated area transient fits of data from the natural sample N2. All errors are standard errors, scaled by the square root of the reduced chi-squared value.

	$\omega(\mathrm{cm}^{-1})$	A_1	$\tau_1(\mathrm{ps})$	A_2	$\tau_2(\mathrm{ps})$
GSB, 298 K	3107	0.9 (± 0.1)	0.50 (± 0.09)	2.0 (± 0.1)	6.4 (± 0.3)
ESA$_S$, 298 K	2963	1.6 (± 0.2)	0.48 (± 0.08)	2.3 (± 0.2)	3.6 (± 0.2)
ESA$_B$, 298 K	3090	–	–	0.4 (± 0.1)	8.0 (± 0.8)

Similar spectra were recorded for samples N4 and S1 (Figure 3.6). Despite the vast difference between N2, N4 and S1, in terms of sample origin, concentrations of N_3VH^0 and nitrogen in total (see further details in Section 2.4), we obtained similar population relaxation times for all three diamond samples. All the τ_2 lifetimes are within one standard error of each other.

However, there is a large disparity between their relative amplitudes, particularly between the natural and synthetic samples. This could be due to the higher concentration of N_3VH^0 present in the natural samples, as evidenced by their more intense 3107 cm^{-1} features in the FTIR. Typically, a higher concentration of N_3VH^0 in a sample leads to a stronger signal as more absorbance of the pump and probe light is possible.

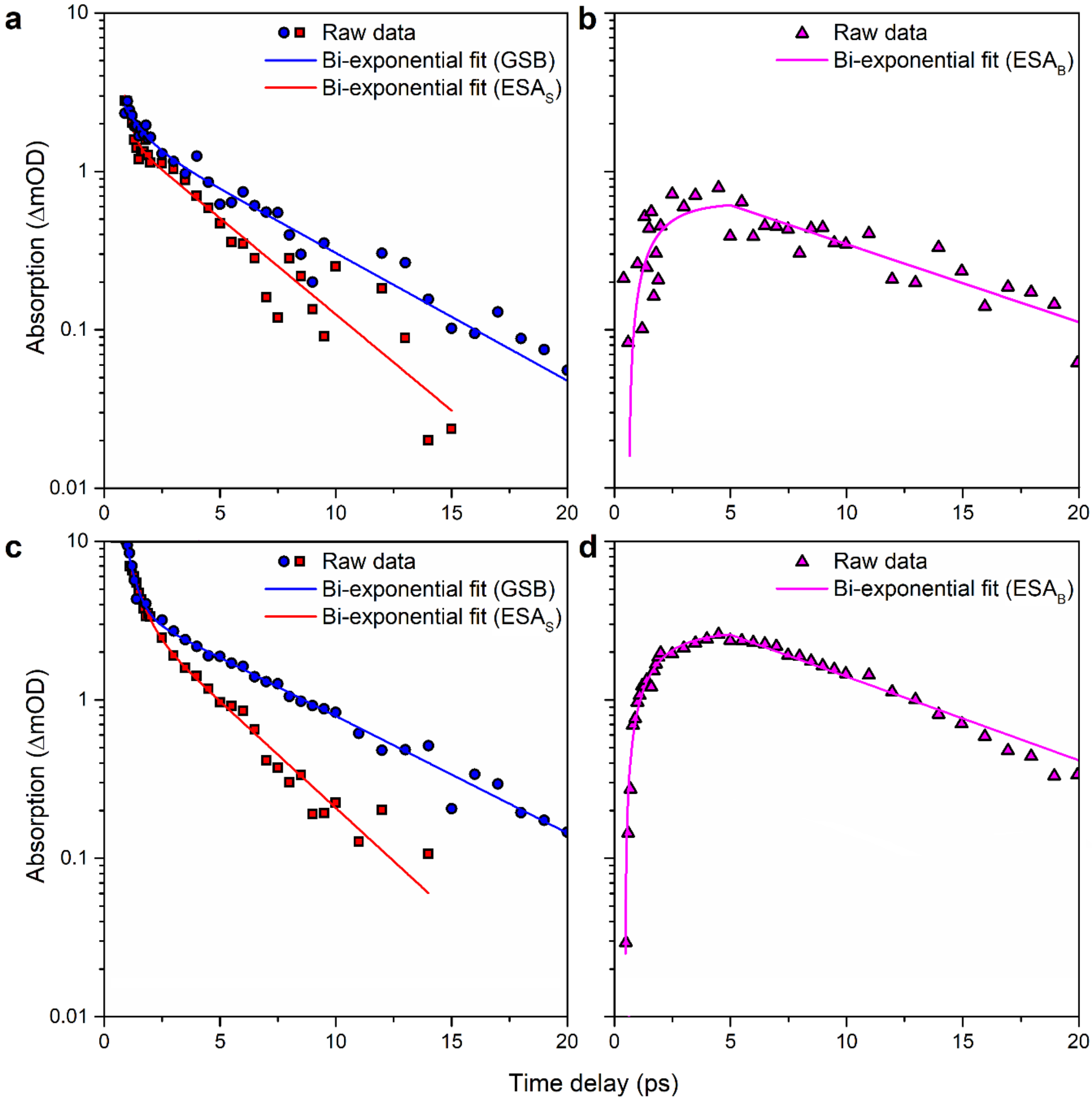

Figure 3.6 Absolute value transient fits of data from samples S1 and N4. **a,** GSB and ESA$_S$ (S1). **b,** ESA$_B$ (S1). **c,** GSB and ESA$_S$ (N4). **d,** ESA$_B$ (N4). These results are comparable to those reported for N2. Thus all samples have comparable energy relaxation dynamics.

Table 3.4 Decay lifetimes from transient fits of data from the synthetic sample S1 and natural sample N4. All measurements were taken at 298 K. The errors are standard errors, scaled by the square root of the reduced chi-squared value.

Sample	**Feature**	$\boldsymbol{\omega}(\mathbf{cm^{-1}})$	$\boldsymbol{A_1}$	$\boldsymbol{\tau_1}(\mathbf{ps})$	$\boldsymbol{A_2}$	$\boldsymbol{\tau_2}(\mathbf{ps})$
S1	**GSB**	3107	0.7 (± 0.2)	0.69 (± 0.25)	1.6 (± 0.2)	5.4 (± 0.7)
	$\mathbf{ESA_S}$	2963	1.2 (± 0.2)	0.29 (± 0.08)	1.8 (± 0.2)	3.3 (± 0.4)
	$\mathbf{ESA_B}$	3090	–	–	0.6 (± 0.1)	8.9 (± 2.2)
N4	**GSB**	3107	5.6 (± 0.2)	0.61 (± 0.04)	3.6 (± 0.2)	5.9 (± 0.3)
	$\mathbf{ESA_S}$	2963	4.0 (± 0.3)	0.54 (± 0.06)	3.3 (± 0.4)	3.2 (± 0.3)
	$\mathbf{ESA_B}$	3090	–	–	2.6 (± 0.1)	8.2 (± 0.3)

To test the relationship between the GSB of N_3VH^0 and the two absorption features ESA_S and ESA_B, we cooled the system from room temperature to 100 K and repeated our TVAS measurements. Figure 3.7 shows the effect of the reduction in temperature on the transients of each feature in N2. The recovery lifetime of the GSB exhibits a significant increase, almost doubling. No analogous change is observed for the decay lifetime of ESA_S. However, the lifetime for decay of ESA_B is seen to increase significantly. The observation of different temperature dependencies between the GSB and ESA_S, and the match between the GSB and ESA_B, offers further credence to the argument that two competing processes are occurring during relaxation.

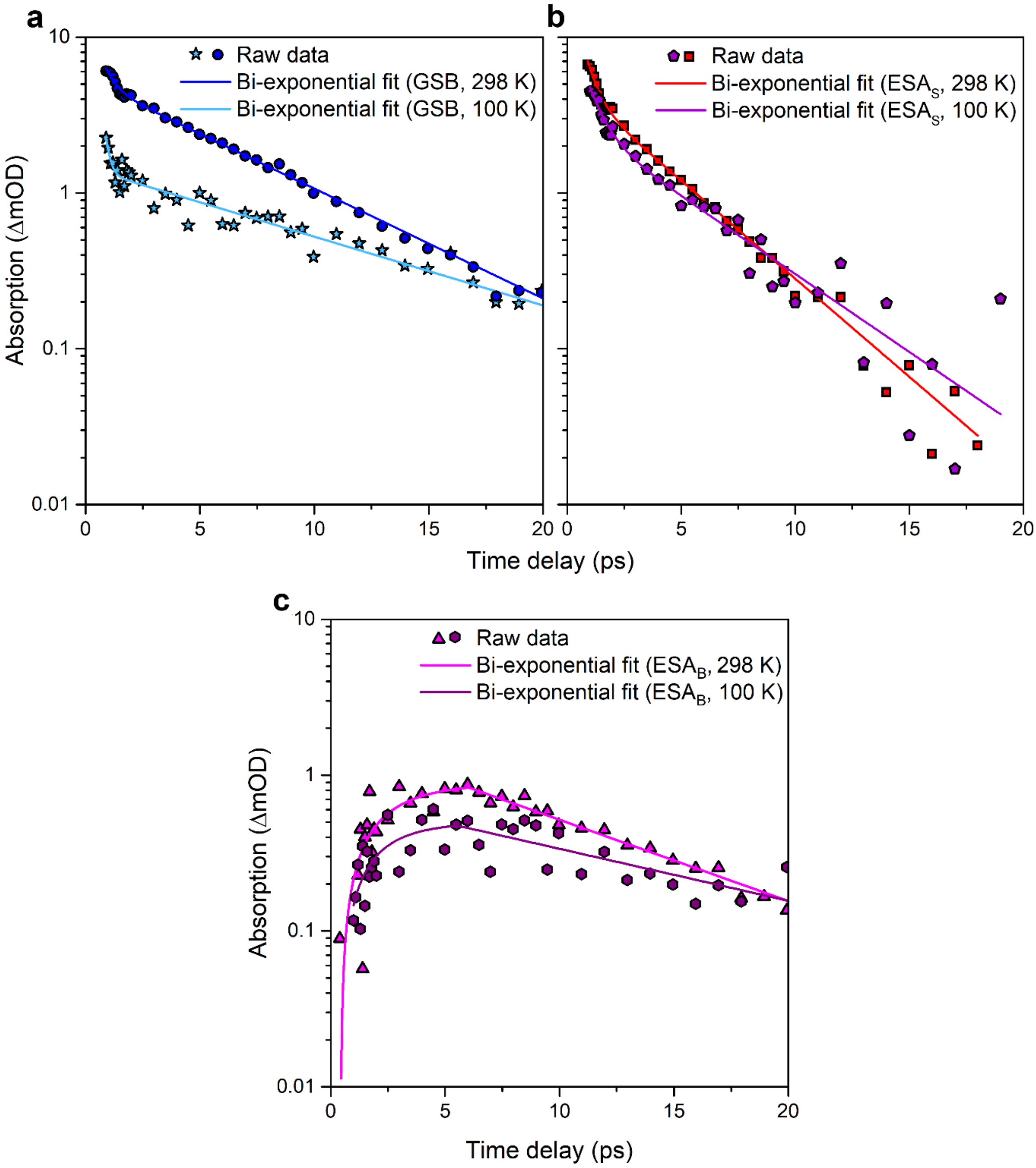

Figure 3.7 Transient absorption difference for N2 at: **a,** peak of GSB, for sample temperatures of 298 K (circles) and 100 K (stars); **b,** ESA$_S$, 298 K (squares) and 100 K (pentagons); **c,** ESA$_B$, 298 K (triangles) and 100 K (hexagons).

3.4 Relaxation mechanism

Based on our results, we propose the following mechanism for the vibrational excitation and decay of the 3107 cm^{-1} C–H stretch, schematically illustrated in Figure 3.8.

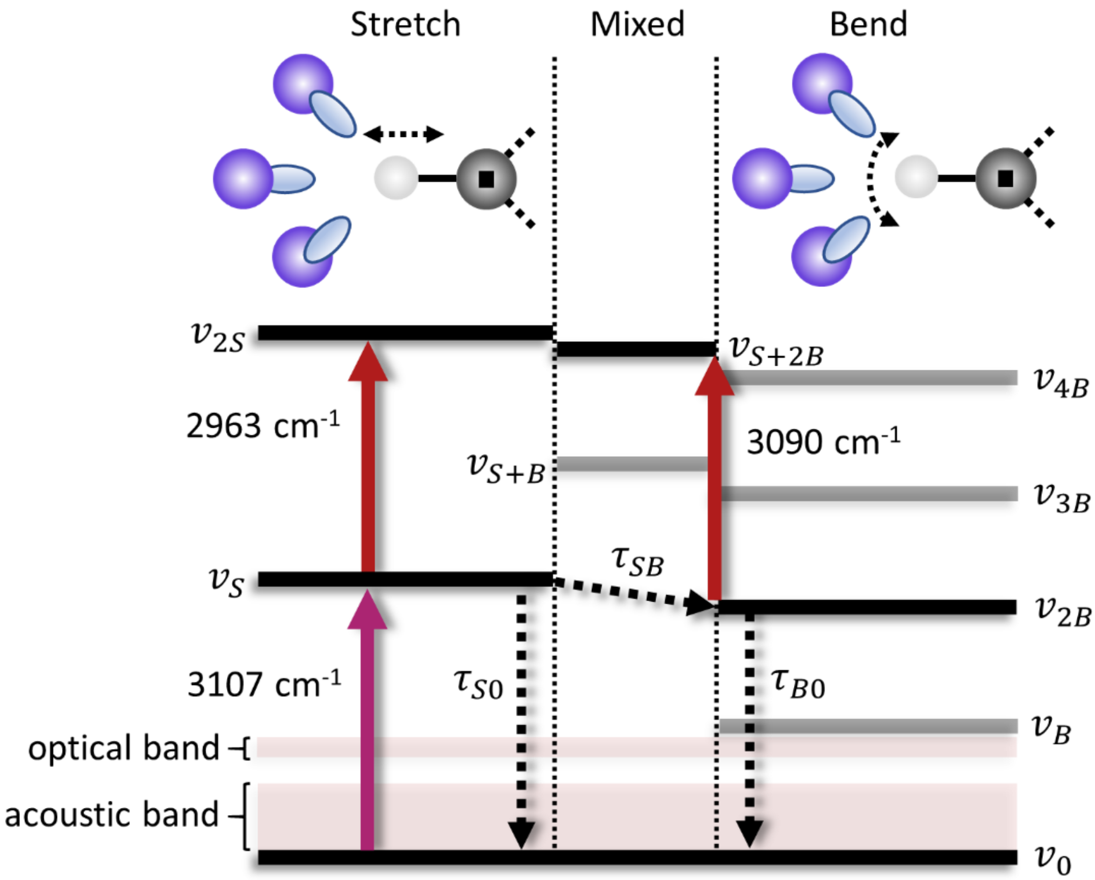

Figure 3.8 Energy level diagram of the vibrational structure of N$_3$VH^0. After the C–H stretch is photoexcited from v_0 to v_S, absorption of the probe pulse occurs at 2963 cm^{-1} from v_S to v_{2S}. Anharmonic coupling to the bend modes provides population in the v_{2B} state, evidenced by excited state absorption at 3090 cm^{-1} which promotes population into the v_{S+2B} state.

The pump pulse, centered at 3107 cm^{-1}, photoexcites the v_S state. This leads to the appearance of the GSB feature at 3107 cm^{-1}, as shown in Figure 3.3. The population now in v_S creates additional absorption into v_{2S} for the probe pulse (at 2963 cm^{-1}), producing ESA$_S$. Decay from v_S occurs either (1) directly (to v_0) or (2) indirectly via the first overtone of the bend mode, v_{2B}. These two processes proceed synchronously but occur at different rates, creating a difference between the decay times of GSB and ESA$_S$ features. The direct pathway (i.e. $v_0 \leftarrow v_S$) likely proceeds through a non-radiative multi-phonon relaxation involving emission of two optical phonons and one acoustic phonon, *cf.* analogous experiments carried out on hydrogen-related modes in the silicon lattice [**20-22**].

We suggest that ESA$_B$ at 3090 cm^{-1} corresponds to excitation from v_{2B} to the combination band v_{S+2B}; the doubly excited bend mode having been populated from decay of the initially populated stretch mode, v_S, as pictured in Figure 3.8 (*i.e.* the indirect pathway). Confidence in this assignment is based on: (1) the IR absorbance features (see Table 3.1), from which we predict that $v_{S+2B} - v_{2B}$ = 3101 cm^{-1}, within error of the wavenumber of ESA$_B$; (2) Symmetry analysis (see Table 3.1), which reveals that anharmonic cross-coupling from v_S to v_{2B} is allowed by symmetry, as both modes include A_1 symmetry character, whereas the transition from v_S to v_B is symmetry-forbidden as two modes, being of A_1 and E symmetry character respectively, do not contain overlapping symmetry elements; and (3) Energy conservation: emission of a single acoustic phonon can provide the energy change required to transfer to the v_{2B} state, whereas at least two phonons would be required to access v_B. One-phonon emission is expected to occur faster than higher order reactions requiring two or more phonons. We cannot however rule out the possibility that ESA$_B$ is due to excitation from v_B to v_{S+B}, which would be a better numerical match to its wavenumber (from the IR, $v_{S+B} - v_B$ = 3091 cm^{-1}) but goes against both the symmetry and energy arguments. A number of multi-phonon processes are possible for non-radiative decay from v_{2B}, some including relaxation via v_B.

To account for the temperature-dependent results, the increase in lifetime of the GSB and $\mathrm{ESA_B}$ upon cooling, we suggest that only the proposed indirect pathway (relaxation via the bend modes) is temperature dependent. It is possible that this pathway is mediated by acoustic phonons, whose population is reduced at lower temperatures. If this was the case, a slower GSB recovery would result without any change to the lifetime for decay of $\mathrm{ESA_S}$, as observed.

3.5 Relating FTIR linewidth to TVAS lifetime

As stated in Section 2.5, the total FTIR linewidth, Γ, of an individual absorption peak is defined:

$$\Gamma = \frac{1}{T_2} = \frac{1}{2\pi T_1} + \frac{1}{\pi T_2^*} + \Gamma_{\mathrm{in}} \tag{3.2}$$

where T_2 is the total dephasing lifetime, which includes contributions from the excited state lifetime for population relaxation, T_1, the lifetime for pure dephasing, T_2^*, and inhomogeneous broadening, Γ_{in}. These three components can be isolated by determination of (1) The homogeneous component of the FTIR linewidth, $\Gamma_{Lorentz}$, which includes contributions from T_1 and T_2^*. It is determined by taking the Lorentzian component of a Voigt fit of the absorption feature, remainder of the linewidth being due to inhomogeneous broadening; (2) The contribution of T_1 to the linewidth, Γ_{TVAS}, which can be predicted from multi-exponential fits of the TVAS data of ESA features using Equations 2.7 and 2.8. The total FTIR linewidth may then be separated into its individual components using the following equation:

$$\Gamma = \Gamma_{Lorentz} + \Gamma_{\mathrm{in}} = \Gamma_{TVAS} + \frac{1}{\pi T_2^*} + \Gamma_{\mathrm{in}} \tag{3.3}$$

Comparison of the observed FTIR linewidths, Γ, their Lorentzian components, $\Gamma_{Lorentz}$, and the linewidths determined from lifetimes measured using TVAS, Γ_{TVAS}, thus reveals the amount of pure dephasing and inhomogeneous broadening taking place in each sample. For N2, $\Gamma_{Lorentz}$ = 2.4 cm^{-1} and Γ_{TVAS} = 2.5 cm^{-1}, and similar agreement was found for N4 and S1 (Table 3.4). Therefore, the population relaxation rate accounts for the homogeneous linewidth in equilibrium, and pure dephasing does not contribute substantially, as reported for hydrogen defects in silicon [**20-22**]. As contributions from pure dephasing are temperature-dependent, the lack of temperature dependence of the 3107 cm^{-1} stretch mode in FTIR further corroborates this conclusion [**23**].

Linewidths obtained from the TVAS experiments are shown in Table 3.5, alongside the total linewidth determined from a Voigt fit of the absorption feature at 3107 cm^{-1}, and the Lorentzian component thereof. The 3107 cm^{-1} LVM in the natural samples N2 and N4 are inhomogeneously broadened, while in the synthetic sample S1 the lineshape was purely Lorentzian, and hence was homogeneously broadened. Inhomogeneous broadening in the natural samples largely results from the close proximity of additional defects that can alter the C–H bond strength by the strain fields that they create. Using known relationships between absorption coefficient and concentration for FTIR modes in the region of 1000-2000 cm^{-1}, in particular A- and B-centres, revealed that the total nitrogen concentration in N2 and N4 to be over 3000 ppm and 1000 ppm respectively. Conversely, in S1 N_3VH^0 was the dominant impurity present, resulting in very little absorption in the 1000-2000 cm^{-1} region and no inhomogeneous broadening.

Table 3.5 Linewidths of the 3107 cm^{-1} feature in each sample, determined from FTIR spectroscopy, compared to those calculated from the lifetimes obtained from transient absorption dynamics.

Sample	$\mathbf{\Gamma}$ $(\mathbf{cm^{-1}})$	$\mathbf{\Gamma_{\mathit{Lorentz}}}$ $(\mathbf{cm^{-1}})$	$\mathbf{\Gamma_{\mathit{TVAS}}}$ $(\mathbf{cm^{-1}})$
N2	4.0	2.4	2.5
N4	4.9	2.7	3.0
S1	2.1	2.1	2.5

To analyse the time- and frequency-dependent transient absorption in more detail, Figure 3.9 shows the linewidth of the spectra of N2 and S1 at room temperature versus time, while Figure 3.9 shows the time constants obtained using fits to "slices" of the transient absorption at different wavenumbers. The FWHM of the GSB is independent of time and can be compared with the total linewidth from FTIR spectroscopy. For S1, with purely homogeneous broadening, the FWHM of the GSB (~3 cm^{-1}), is comparable to the linewidth in equilibrium (2.1 cm^{-1}). The poorer spectral resolution of the spectrometer used in the transient experiment accounts for the difference. In N2, the GSB is broader than in S1, as a result of inhomogeneous broadening. In Figure 3.3, the linewidth of ESA$_S$ can be seen to be broader than the linewidth of the GSB, which we speculate reflects the contribution to the linewidth from energy relaxation from the v_{2S} level. This assertion is based on the observation that the expression for the FWHM linewidth, Γ_{ij}, for an optical transition between state *i* and state *j,* with respective population decay lifetimes τ_i and τ_j, is $\Gamma_{ij} = \frac{1}{2\pi}\left(\frac{1}{\tau_i} + \frac{1}{\tau_j}\right)$ [**24**]. Hence the linewidth for the ESA associated with the *n* = 1 to *n* = 2 vibrational transition is larger than that for the *n* = 0 to *n* = 1 (as the population lifetime for the ground state is infinite). Pure dephasing may also contribute more substantially to the linewidth for ESA$_S$.

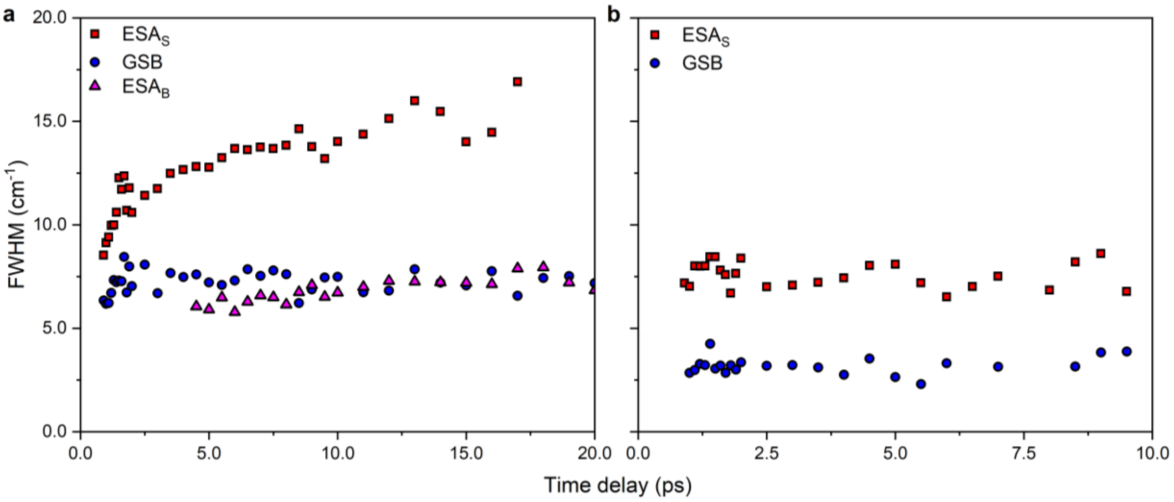

Figure 3.9 Full-width at half-maximum (FWHM) of the GSB (circles), ESA$_S$ (squares) and ESA$_B$ (triangles) features in the transient absorption spectra of **a,** sample N2, and **b,** sample S1, at room temperature.

From Figure 3.10, we can see that the dynamics of the GSB, ESA$_S$ and ESA$_B$ are largely independent of wavenumber. The weak trend in τ_2 for the GSB of sample N2 may indicate subtle changes to the relaxation dynamics for defects in a more strained environment.

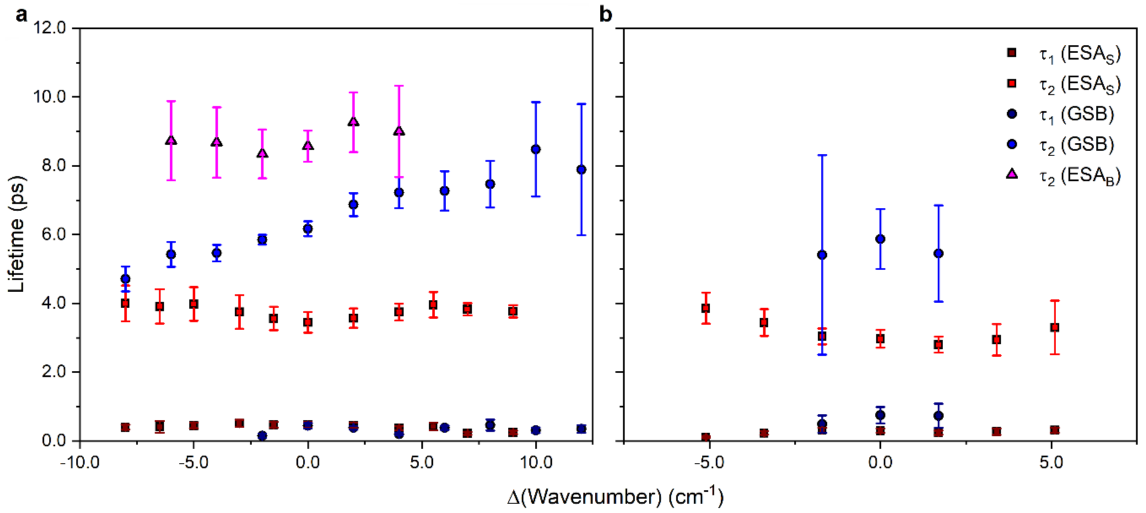

Figure 3.10 Lifetimes τ_1 and τ_2, and their standard errors, obtained from biexponential fits to the transient absorption at different wavenumbers relative to the centers of the GSB, ESA$_S$ and ESA$_B$ features, for: **a,** sample N2 and **b,** sample S1.

3.6 Determination of concentration from the Morse potential

Prior to this work, the relationship between the optical absorption coefficient of the N_3VH^0 defect and its concentration was uncertain. At best, it was estimated using known standards (such as that of the NVH^0 defect) and concentration assays during different stages of the annealing process, of which N_3VH^0 is the end product. The energy spacings, 3107 cm^{-1} and 2963 cm^{-1}, directly obtained from TVAS now allow simulation of the Morse potential to approximate the anharmonic potential energy, $V(r)$, of the N_3VH^0 stretch mode along the direction of the C–H bond, according to the following equation:

$$V(r) = D_e(1 - e^{-a(r-r_e)})^2 \tag{3.4}$$

where D_e is the depth of the potential well, a is the inverse width of the well, r is the distance between the two atoms involved in the bonding of the vibrational mode, and r_e is the equilibrium position. The individual vibrational energy states inside the potential energy well are determined by solving the Schrödinger equation for each state, further details of which are included in Section 2.6. Figure 3.11 shows the computed anharmonic potential energy well, including the individual vibrational states.

From our simulation, we determined the following parameters for the Morse potential: well depth $D_e = 4.54$ eV and inverse width $a = 1.99 \times 10^{10}\ \mathrm{m}^{-1}$. The importance of the Morse potential is that it allows the matrix elements D_{ij}, and hence the absorption coefficient, to be calculated directly with the defect concentration as the only free parameter. Through this method, we predict dimensionless matrix elements of $\langle \psi_1 | x | \psi_0 \rangle = 0.150$ for the $v_S \leftarrow v_0$ transition and $\langle \psi_2 | x | \psi_1 \rangle = 0.215$ for the $v_{2S} \leftarrow v_S$ transition. As the probe light shines onto the (100) surface of the diamond, it is not parallel to the [111] direction of the C–H bond in

N_3VH^0. This can be accounted for by a reduction of the matrix element by a factor of $\sqrt{3}$, to $\langle\psi_1|x|\psi_0\rangle = 0.087$ and $\langle\psi_2|x|\psi_1\rangle = 0.124$. Substituting these matrix elements into Equation 2.22, we determine the ratio of the amplitude of the ESAs ($\Delta\alpha_{12}$) and GSB ($\Delta\alpha_{01}$) features: the Morse potential model predicts $\frac{\Delta\alpha_{12}}{\Delta\alpha_{01}} = -1.03$. The experimental transient absorption spectra of N2 yield $\frac{\Delta\alpha_{12}}{\Delta\alpha_{01}} = -1.13$, corroborating with the theory.

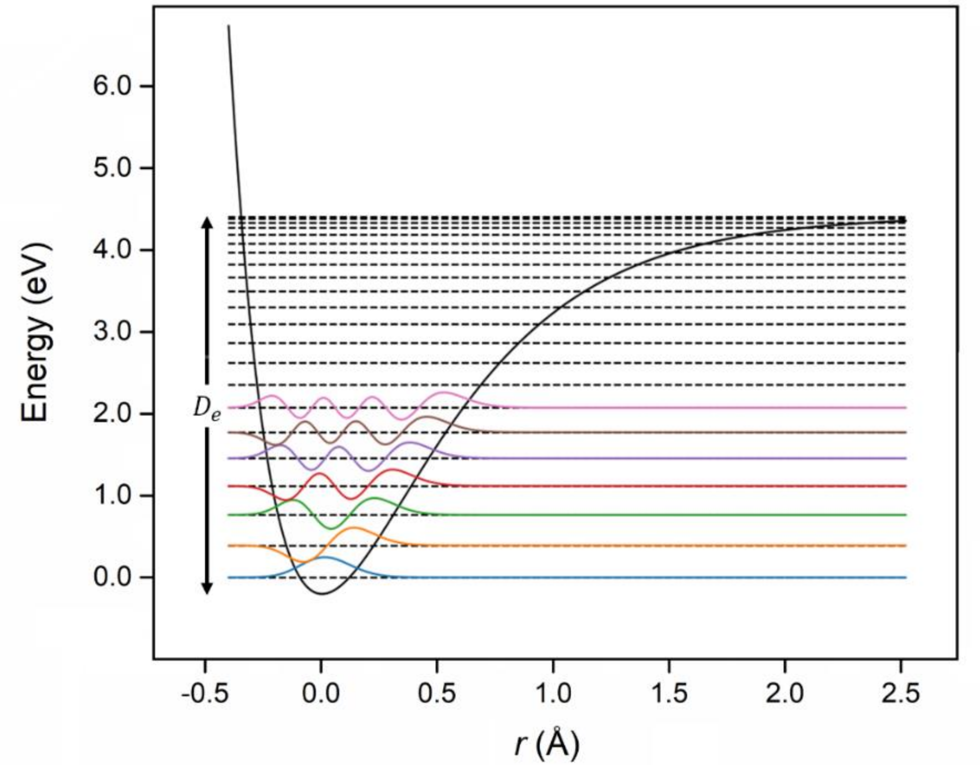

Figure 3.11 Anharmonic Morse potential energy well of the C–H stretch as a function of r, the distortion from equilibrium geometry, showing the vibrational structure.

By using the measured FTIR absorption and the matrix elements from the Morse potential model, we can determine the concentration of N_3VH^0, assuming optical absorption occurs between two quantum states with a Lorentzian lineshape. This condition is straightforwardly satisfied for sample S1, which exhibited a Lorentzian absorption spectrum around 3107 cm^{-1}, and for which we estimate a N_3VH^0 concentration of 4.2 ppm. Relating this estimate to the integrated area of the 3107 cm^{-1} peak, I_{3107}, in FTIR provides the following calibration factor: $[\mathrm{N_3VH^0}](\mathrm{ppb}) = (110 \pm 10) \times I_{3107}(\mathrm{cm^{-2}})$, which can be used to estimate the N_3VH^0 concentration from the FTIR data. The natural diamonds, which exhibited inhomogeneous line broadening caused by strain induced by the high number of point defects, we instead use the Lorentzian component of a Voigt fit and can similarly estimate [N_3VH^0]. These numbers are shown in Table 3.6.

To verify the estimate of the N_3VH^0 concentration from our method, we used two approaches: (1) Using the known relationship between absorption strength and concentration for the NVH^0 defect [**25**], $[\mathrm{NVH^0}](\mathrm{ppb}) = (200 \pm 20) \times I_{3123}(\mathrm{cm^{-2}})$ the predicted concentration of N_3VH^0 in sample S1 is 7.6 ± 0.8 ppm. This is similar in magnitude to the value of 4.2 ppm obtained using the Morse potential and the linewidth and seems reasonable given the assumptions used in both methods. (2) Estimating the upper limit of [N_3VH^0] from the total nitrogen concentration (in all different forms) in the as-grown CVD diamond sample, and that which cannot be accounted for in defects other than N_3VH^0 after HPHT annealing. In this way, we estimate that the maximum concentration of N_3VH^0 is less than 10 ppm in S1. Both methods yield values that are consistent with our value for N_3VH^0 concentration in S1 (~4 ppm) obtained from the TVAS, giving confidence to our calibration equation for deriving N_3VH^0 concentration from integrated peak area.

Table 3.6 N_3VH^0 concentrations determined using the Morse potential model, compared to those predicted from the NVH^0 relation.

Sample	$[\mathbf{N_3VH^0}]_{Morse}(\mathbf{ppm})$	$[\mathbf{N_3VH^0}]_{NVH^0}(\mathbf{ppm})$
N2	21.8 ± 2.0	40.1 ± 4.0
N4	3.9 ± 0.4	10.0 ± 1.0
S1	4.2 ± 0.4	7.6 ± 0.8

3.7 Kinetic model of 3-level system

To match our energy level system to experimental observations, we created a rate-equation kinetic model comprised of rate equations based on the processes shown in Figure 3.11. This model incorporated v_S, v_{2B} and v_0 and included the dynamics of the GSB, ESA$_S$ and ESA$_B$ together. We defined the populations N_S, N_B and N_0 of each level to change according to the rate equations:

$$\frac{\partial N_S}{\partial t} = -\frac{N_S}{\tau_{S0}} - \frac{N_S}{\tau_{SB}} \tag{3.5}$$

$$\frac{\partial N_B}{\partial t} = \frac{N_S}{\tau_{SB}} - \frac{N_B}{\tau_{B0}} \tag{3.6}$$

$$\frac{\partial N_0}{\partial t} = \frac{N_S}{\tau_{S0}} + \frac{N_B}{\tau_{B0}} \tag{3.7}$$

We define the following time-constants for decay from one level to another: τ_{S0} for the transition $v_0 \leftarrow v_S$, τ_{SB} for the transition $v_{2B} \leftarrow v_S$ and τ_{B0} for the transition $v_0 \leftarrow v_{2B}$. We used these equations to determine functions for the decay of the ESAs and recovery of the GSB, which we fit to the data obtained from TVAS. To fit the fast τ_1 component from our data, we added a fixed decay / recovery with a time-constant of 0.4 ps to the functions for the GSB and ESA$_S$.

The fit to data from N2, shown in Figure 3.12, gives estimate time-constants for each of the three processes: τ_{S0} = 6.9 ± 0.2 ps, τ_{SB} = 6.4 ± 0.2 ps and τ_{B0} = 5.6 ± 0.4 ps. The similarity in these values allows for competition between the direct and indirect decays, leading to the disparity in lifetime between ESA$_S$ and the GSB. Through our fitting, we estimated the dimensionless matrix element for the transition $v_{S+2B} \leftarrow v_{2B}$ to be 0.157. This number fits reasonably well with our derived values from the Morse potential calculations, 0.150 for the excitation $v_S \leftarrow v_0$ and 0.215 for the transition $v_{2S} \leftarrow v_S$, which gives credence to our assignment of ESA$_B$ to a transition associated with the C–H stretch. We repeated these fits for samples N4 and S1. All the results of our kinetic model fits are detailed in Table 3.7.

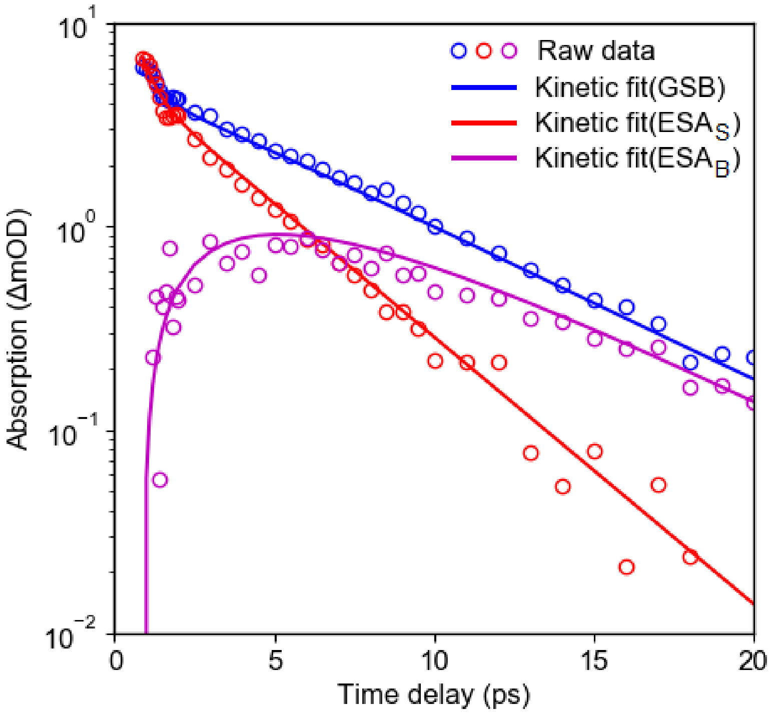

Figure 3.12 Kinetic fit using data from sample N2 at three different wavelengths corresponding to the maxima of each of the three features GSB, ESA$_S$ and ESA$_B$. The fit was created from rate equations according to the processes described in Figure 3.8.

Table 3.7 Time constants, corresponding to the processes shown in Figure 3.8, produced from kinetic fits of TVAS data from N2, N4 and S1.

Sample	τ_{S0} (ps)	τ_{SB} (ps)	τ_{B0} (ps)
N2	6.9 ± 0.2	6.4 ± 0.2	5.6 ± 0.4
N4	6.9 ± 0.7	5.6 ± 0.6	6.1 ± 1.1
S1	6.5 ± 0.5	5.7 ± 0.6	5.1 ± 1.0

3.8 Conclusions and future work

We have successfully used transient vibrational absorption spectroscopy to determine the lifetimes for decay or recovery of vibrational modes in the N_3VH^0 defect in diamond. Our results confer information about the mechanism for the decay of the excited stretch (v_S) mode. The observation of an excited state absorption at 2963 cm^{-1} confirms that the v_{2S} state lies at 6070 cm^{-1} in the IR absorption and quantifies the anharmonicity of the stretch mode. Calculations based on the Morse potential were made possible by knowing the extent of the anharmonicity of the stretch mode. This allowed us to estimate the oscillator strength for the C–H stretch mode in N_3VH^0, thereby relating FTIR peak intensity to defect concentration directly for this prominent defect, which is the most stable form of both nitrogen and hydrogen in diamond. Thus, we were able to deduce the concentration of N_3VH^0, in reasonable agreement with values derived from other methods. With regards to the vibrational dynamics, decay from v_S occurs through two separate pathways – a direct decay back down to the ground state, and an indirect relaxation via the excited two-bend (v_{2B}) mode of the C–H bond. These decays occur at different rates, producing an overall lifetime for the recovery of the ground-state that is an amalgamation of the two.

With regards to N_3VH^0, further study carried out on its other vibrational modes, particularly the v_B and v_{2B} modes at 1405 cm^{-1} and 2787 cm^{-1} respectively, and their response to excitation of the v_S mode, would add to the current picture for vibrational dynamics of the defect. A study of the latter feature in particular would test the proposed mechanism for relaxation via the v_{2B} mode. More broadly speaking, the experimental and theoretical methodology developed in this study can be applied to the IR-active vibrational modes of other atomic-scale defects, both in diamond and in other materials. This is demonstrated by an identical study of the stretch mode of another diamond defect in the following chapter. Hence, it is now possible to determine decay pathways, establish the energetic landscape of LVMs, and quantify defect concentrations for a wide suite of defects of interest in optical and electronic applications.

3.9 References

1. D. J. L. Coxon, M. Staniforth, B. G. Breeze, S. E. Greenough, J. P. Goss, M. Monti, J. Lloyd-Hughes, V. G. Stavros, M. E. Newton, *J. Phys. Chem. Lett.* **2020**, *11*, 6677–6683.

2. M. N. R. Ashfold, J. P. Goss, B. L. Green, P. W. May, M. E. Newton, C. V. Peaker, Nitrogen in Diamond. *Chem. Rev.* **2020**, *120*, 5745-5794.

3. K. Iakoubovskii, G. J. Adriaenssens, *Diam. Relat. Mater.* **2002**, *11*, 125–131.

4. C. Van Der Bogert, C. Smith, T. Hainschwang, S. McClure, *Gems Gemol.* **2009**, 45, 20-37.

5. B. Rondeau, E. Fritsch, M. Guiraud, J. P. Chalain, F. Notari, *Diam. Relat. Mater.* **2004**, *13*, 1658–1673.

6. S. C. Kohn, L. Speich, C. B. Smith, G. P. Bulanova, *Lithos* **2016**, *265*, 148–158.

7. I. Kiflawi, D. Fisher, H. Kanda, G. Sittas, *Diam. Relat. Mater.* **1996**, *5*, 1516–1518.

8. S. J. Charles, J. E. Butler, B. N. Feygelson, M. E. Newton, D. L. Carroll, J. W. Steeds, H. Darwish, C. S. Yan, H. K. Mao, R. J. Hemley, *Phys. Status Solidi A* **2004**, *201*, 2473–2485.

9. F. De Weerdt, I. N. Kupriyanov, *Diam. Relat. Mater.* **2002**, *11*, 714–715.

10. J. J. Charette, *Physica* **1959**, *25*, 1303–1312.

11. G. S. Woods, A. T. Collins, *J. Phys. Chem. Solids* **1983**, *44*, 471–475.

12. G. Davies, A. T. Collins, P. Spear, *Solid State Commun.* **1984**, *49*, 433–436.

13. F. De Weerdt, Y. N. Pal'yanov, A. T. Collins, *J. Phys. Condens. Matter* **2003**, *15*, 3163–3170.

14. J. P. Goss, P. R. Briddon, V. Hill, R. Jones, M. J. Rayson, *J. Phys. Condens. Matter* **2014**, *26*, 145801.

15. F. S. Gentile, S. Salustro, M. Causa, A. Erba, P. Carbonniere, R. Dovesi, *Phys. Chem. Chem. Phys.* **2017**, *19*, 22221–22229.

16. E. Fritsch, T. Hainschwang, L. Massi, B. Rondeau, *New Diam. Front. Carbon Technol.* **2007**, *17*, 63–89.

17. E. B. Wilson, J. C. Decius, P. C. Cross, *Molecular vibrations : the theory of infrared and Raman vibrational spectra*; Dover Publications: USA, **2003**.

18. G. Herzberg, *Molecular Spectra and Molecular Structure. II. Infrared and Raman Spectra of Polyatomic Molecules.* Van Nostrand: USA, **1990**.

19. J.-K. Wang, C.-S. Tsai, C.-E. Lin, J.-C. Lin. *J. Chem. Phys.* **2000**, *113*, 5041-5052.

20. M. Budde, G. Lüpke, C. Parks Cheney, N. H. Tolk, L. C. Feldman, *Phys. Rev. Lett.* **2000**, *85*, 1452–1455.

21. M. Budde, G. Lüpke, E. Chen, X. Zhang, N. H. Tolk, L. C. Feldman, E. Tarhan, A. K. Ramdas, M. Stavola, *Phys. Rev. Lett.* **2001**, *87*, 145501.

22. G. Lüpke, N. H. Tolk, L. C. Feldman, *J. Appl. Phys.* **2003**, *93*, 2317–2336.

23. J. L. Skinner, *Ann. Rev. Phys. Chem.* **1988**, *39*, 463-78.

24. E. Rosencher, B. Vinter, *Optoelectronics*; Cambridge University Press: UK, **2002**.

25. R. U. A. Khan, P. M. Martineau, B. L. Cann, M. E. Newton, D. J. Twitchen, *J. Phys. Condens. Matter* **2009**, *21*, 364214.

4 A study of the absorption feature at 3237 cm^{-1}

4.1 Background

The family of infrared (IR) absorption features corresponding to the N_3VH^0 defect, as discussed in Chapter 3, are often accompanied by a sharp feature at 3237 cm^{-1}. This feature was first observed by Charette, discovered alongside the 3107 cm^{-1} line [**1**]. It has subsequently been found in many type Ia and Ib natural diamonds, and in some high pressure, high temperature (HPHT) diamonds [**1-6**]. In each case, it does not appear to correlate with the lines belonging to the N_3VH^0 group of features, which were reported in Table 3.1 and Section 3.2. Therefore, it is presumed that the 3237 cm^{-1} line is not related to N_3VH^0 itself, but may similarly involve both hydrogen and nitrogen in its composition. There have been a number of proposals as to the identity of the defect responsible for the mode at 3237 cm^{-1}, but no concrete assignment has ever been made.

Based on its position in the IR spectrum, this feature has been assigned to the N–H stretch from an amide (–N(H)C=O) group [**2**], or the C–H stretch of an alkyne (–C≡CH) group [**3**]. However, no related modes have been located in the Fourier transform infrared (FTIR) spectrum of diamonds containing this feature. Subsequent studies were carried out by De Weerdt *et al.* on a series of hydrogen-rich HPHT diamond samples grown from ^{13}C, to examine isotopic shifting in IR features from defects [**4**]. Their work showed that the 3107 cm^{-1} mode, from N_3VH^0, shifts its position to 3098 cm^{-1} when a significant amount of ^{13}C is present. This identifies it as a C–H mode. By contrast, the 3237 cm^{-1} mode did not exhibit any ^{13}C isotopic shift. It thus appears likely that this mode originates from an N–H vibrational mode, though this has yet to be proven by ^{15}N isotopic substitution studies.

Fritsch *et al.* reported a correlation between the 3237 cm^{-1} feature and another feature observed in the IR spectrum at 4703 cm^{-1} [**7**]. They proposed that these two lines originated from the same defect, with the latter feature arising from a stretch mode plus a bend mode, v_{S+B}. They thus predicted the corresponding bend mode to lie in the range 1400-1500 cm^{-1}, although no mode in that region has yet been correlated with the one at 3237 cm^{-1}. This is due to the presence of several intense bands in this region in most diamond samples high in nitrogen and hydrogen.

The presence of at least two modes in similar positions to N_3VH^0 suggests some similarity between the two defects. Assuming that this mode arises from an N–H bond, one possibility would be the decoration of a B-nitrogen centre (N_4V^0) with a hydrogen atom, to form N_4VH^0. However, its formation is not energetically favourable. [**8**] Furthermore, high temperature annealing of diamond samples rich in nitrogen and hydrogen produces N_3VH^0 as the end product, as demonstrated in Section 2.4. In a recent computational study, Gu *et al.* suggested that interaction of a B-nitrogen centre with a platelet, an extended planar defect which often contains large amounts of aggregated nitrogen, may allow N_4VH^0 to form [**9**]. Of the two proposed models for this interaction, one predicted a stretch mode close to 3237 cm^{-1}. It therefore remains possible that the 3237 cm^{-1} mode is connected to the N_XVH family of defects.

Using the methodology developed in Chapter 3, we report the investigation of the vibrational dynamics of this defect following IR excitation of its X–H stretch mode (v_S = 3237 cm^{-1}). This allowed detection of the v_{2S} mode, a feature too weak to be observed via conventional FTIR spectroscopy. As in Chapter 3, obtaining this information allows for the determination of a concentration of this defect, allowing for a comparison to the N_3VH^0 concentration in each diamond sample. Additionally, the relaxation dynamics of this mode can be mapped out, allowing a direct comparison with the stretch mode associated with N_3VH^0 in terms of relaxation time, pathway(s) and anharmonicity. This information offers new insight into the properties of this defect, which may further assist in its identification.

4.2 Absorption in equilibrium

Two natural diamonds, N3 and N5 (see Section 2.4 for more details), were used to study the 3237 cm^{-1} mode. N3 was selected for this study because of its high intensity 3237 cm^{-1} features, and N5 as it differs in both origin and the type of nitrogen defects present compared to N3.

The FTIR spectrum of N3 is shown in Figure 4.1. As evident, the region 1000-1500 cm^{-1}, is largely populated by nitrogen-related modes. The maximum absorption coefficient measurable for this spectrometer on this sample was 50 cm^{-1}, due to both high sample thickness and large nitrogen concentration. As with sample N1 (see Section 2.4 and Figure 3.2 for more details), the majority of this signal can be ascribed to the B-nitrogen centre (N_4V^0) [**10**]. The high intensity of the υ_S = 3237 cm^{-1} mode in this sample implies a high concentration of its associated defect. This also allows the detection of the 4703 cm^{-1} feature, thought to be the υ_{S+B} mode of the same defect.

The FTIR spectrum of N5 is shown in Figure 4.2. In this sample, the observed signal in the 1000-1500 cm^{-1} region can be assigned to the A-nitrogen centre (N_2^0) [**11-12**]. The lower intensity 3237 cm^{-1} feature in this sample is reflected in the absence of a 4703 cm^{-1} feature, which is too weak to be detected.

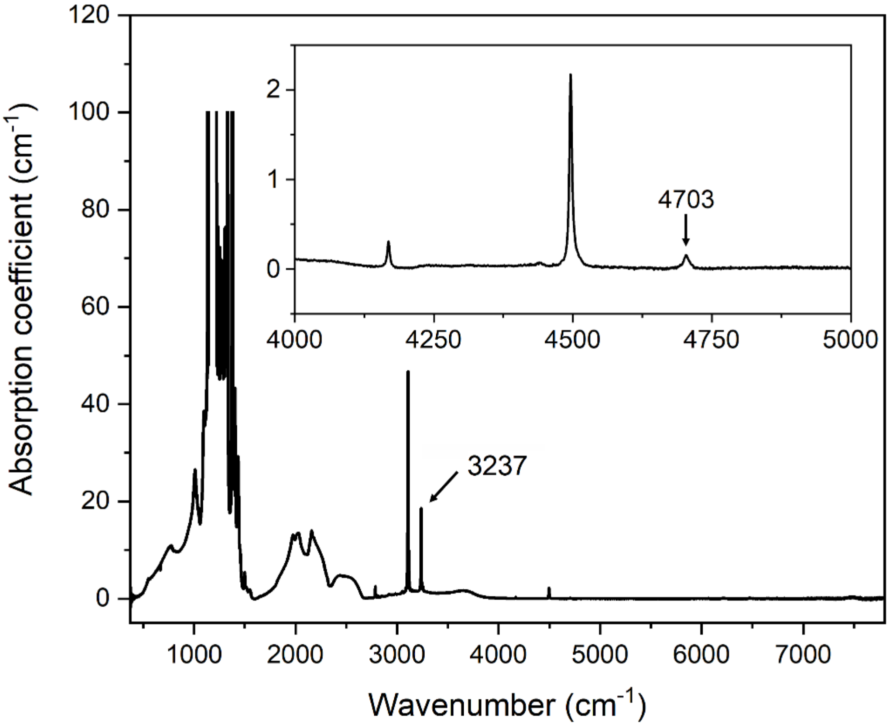

Figure 4.1 FTIR spectrum of natural diamond N3, including regions of saturated absorption.

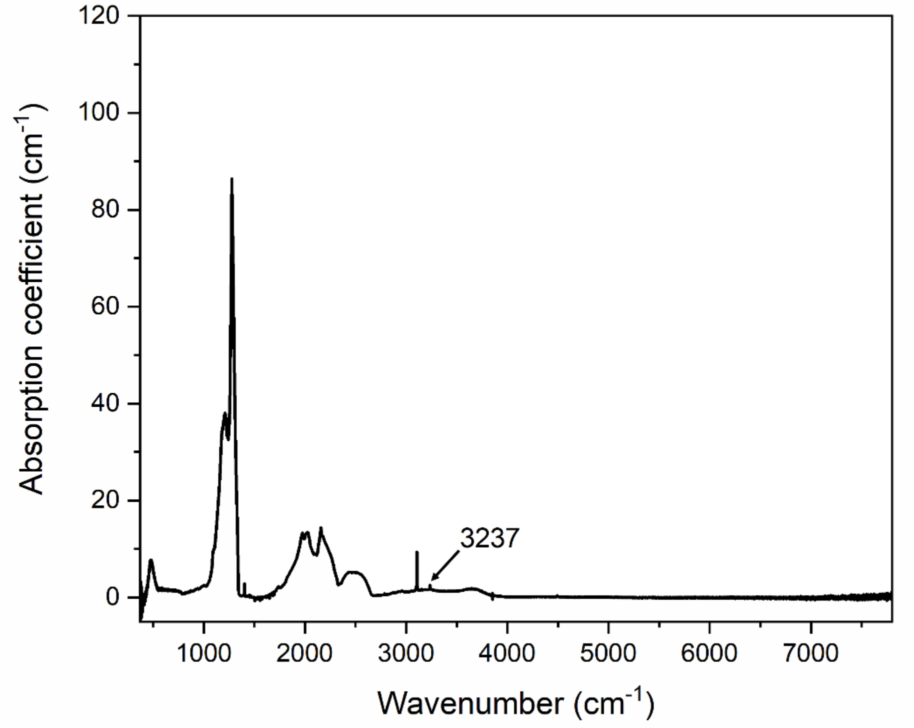

Figure 4.2 FTIR spectrum of natural diamond N5.

4.3 Transient absorption

Transient vibrational absorption spectroscopy (TVAS) was employed to investigate the excited state dynamics of the defect responsible for the 3237 cm^{-1} feature, upon IR photoexcitation. The photoexcitation pulse was resonant to the 3237 cm^{-1} (υ_S) local vibrational mode (LVM), with its spectral bandwidth narrowed by the pulse shaper to 250 cm^{-1} to avoid any overlap with the 3107 cm^{-1} LVM and thus excitation of vibrational states belonging to N_3VH^0. The broadband probe was tuned either resonantly to υ_S or set to probe other spectral ranges in the surrounding region (υ_{probe} = 2800-3300 cm^{-1}). The transient absorption spectra (TAS) from sample N3 are presented in Figure 4.3 at different pump-probe time delays, Δt.

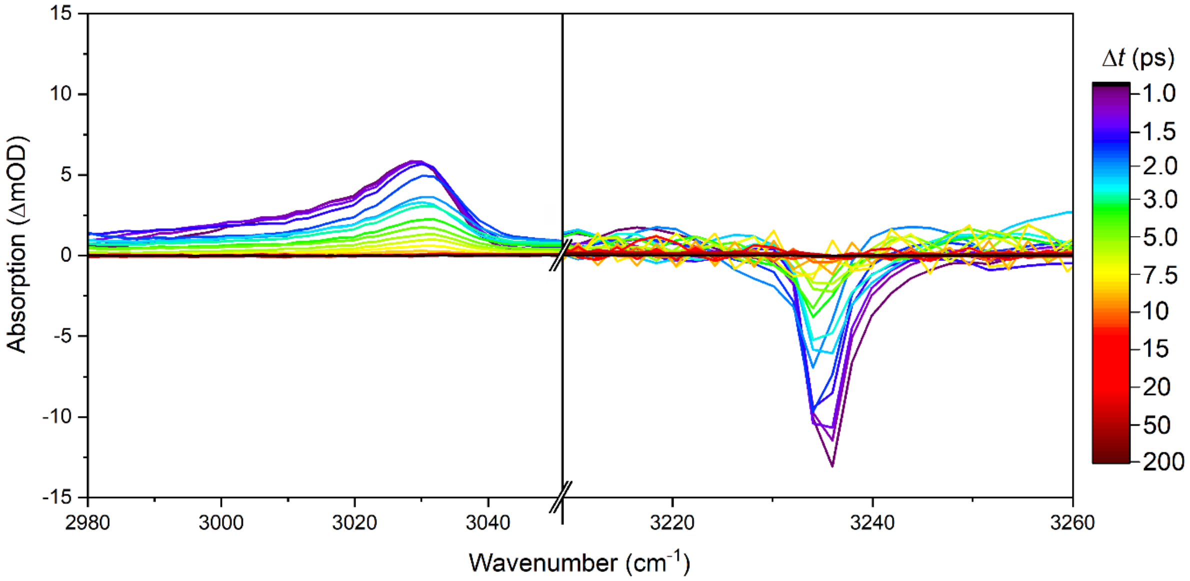

Figure 4.3 TVAS results for natural diamond N3. Transient absorption spectra for pump-probe delays 1 ps < Δt < 200 ps, for pump excitation centred at 3237 cm^{-1} and probed either around 3030 cm^{-1} (left) or 3237 cm^{-1} (right).

In the degenerate pump-probe spectrum ($\upsilon_{pump} = \upsilon_{probe}$ = 3237 cm^{-1}), shown in Figure 4.3 right, a ground state bleach (GSB) is observed. This indicates the expected reduction in the ground vibrational state population, N_0. A non-degenerate probe (Figure 4.3, left) revealed an excited state absorption (ESA) feature at 3029 cm^{-1}. This feature is analogous to ESA$_S$ in N$_3$VH^0 (see Section 3.3 and Figure 3.3), in that it corresponds to an absorption of the probe from υ_S to υ_{2S}, in an anharmonic potential energy function along this stretch mode. In this case, the extent of anharmonicity is increased; for N$_3$VH^0, the difference between its GSB and ESA$_S$ features is $2\omega x$ = 144 cm^{-1}, whereas for this defect, the difference between its GSB and ESA features is $2\omega x$ = 208 cm^{-1}. Furthermore, the $n = 2 \leftarrow n = 0$ transition is predicted to lie at 6266 cm^{-1} (= 3237 + 3029) cm^{-1}. This cannot be verified by FTIR spectroscopy, as a feature in this region has never been observed in diamonds found to contain this defect. However, the comparative studies on the analogous 3107 cm^{-1} mode in N$_3$VH^0 (Chapter 3) correctly determined the position of υ_{2S} at 6070 cm^{-1}. Thus, υ_{2S} for this defect is predicted to lie at 6266 cm^{-1}. Additionally, the absorption strength of the 6070 cm^{-1} υ_{2S} feature in N$_3$VH^0 is significantly lower than its corresponding υ_S feature at 3107 cm^{-1}, due to its small, electric-dipole-forbidden matrix element. The same being true for the 3237 cm^{-1} defect, we would expect its corresponding υ_{2S} feature to be below the signal-to-noise and thus undetectable in the FTIR at this concentration.

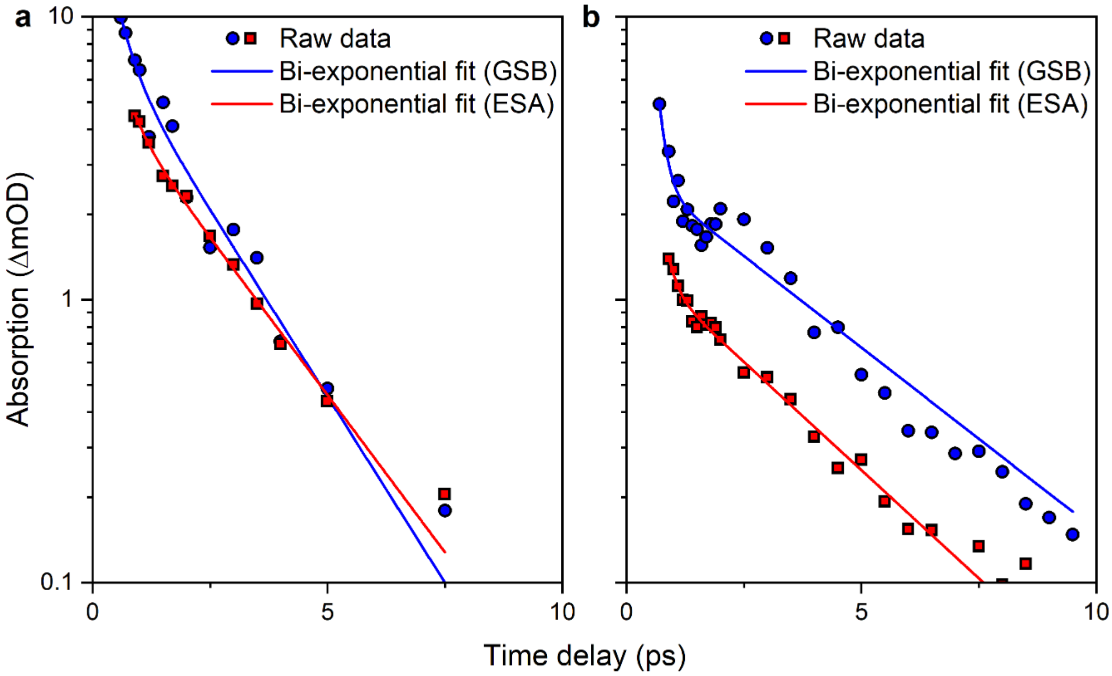

Figure 4.4 Transient fits of TVAS data for **a,** natural diamond N3 and **b,** natural diamond N5. The modulus of the absorption difference for GSB (blue circles) and the ESA (red squares) is measured at the wavenumber of their peak maxima, and bi-exponential fits (solid lines).

For the vibrational dynamics, Figure 4.4 reports the modulus of the absorption change for the GSB and ESA features versus pump-probe time-delay, for both the N3 and N5 diamonds. For consistency, a multi-component, bi-exponential decay was fit for both features, with associated time-constants τ_1, the fast transfer via other LVMs or the diamond lattice, and τ_2, relaxation via the modes of this LVM [**13**]. In contrast to the transients of the GSB and ESAs from the N_3VH^0 data (see Section 3.3), the dynamics observed from Figure 4.4 show that the decay lifetimes of the GSB and ESA features are within one standard error of each other. In other words, the rate at which $n = 1$ is depopulated, shown by the lifetime of the ESA, is roughly equal to the rate at which $n = 0$ recovers, shown by the lifetime of the GSB. This suggests a single decay channel from $n = 1$ to $n = 0$. The absence of any other features in the spectrum close to the GSB further corroborates this conclusion.

In contrast to the data in Chapter 3, the lifetime of population decay from $n = 1$ to $n = 0$ varies markedly between samples N3 and N5. The long ESA decay time (τ_2 = 1.9 ± 0.2 ps) in N3 is significantly shorter than the equivalent lifetime (τ_2 = 2.8 ± 0.1 ps) in N5, and the same is true for the recovery time of the GSB. Furthermore, the τ_1 lifetimes of the two samples also deviate from each other. This difference is unique to excitation of the 3237 cm^{-1} feature – the lifetimes of the GSB and ESA$_S$ features of N_3VH^0 show no significant deviation between samples (see Section 3.3). Without knowing the exact defect structure, it is not possible to exactly identify the cause of this difference. However, one significant difference between the two samples is the different types of defects contained within them. Whilst both samples have similar total nitrogen concentrations, the majority of the nitrogen present in N3 exists as B-nitrogen centres, N_4V^0, whereas in N5 the nitrogen content is largely attributed to A-nitrogen centres, N_2^0. It appears that the high quantity of B-nitrogen centres is mediating the faster relaxation seen in N3. This points to a link between the structure of a B-nitrogen centre and that of the defect being studied here. One possibility is the attachment of hydrogen to a B-nitrogen centre, forming N_4VH^0. The formation of such a defect is energetically unfavourable, though there may be some means of stabilising it through interaction with other defects [**8,9**].

Table 4.1 Decay lifetimes from transient fits of data from the natural samples N3 and N5. All measurements were taken at 298 K. The errors are standard errors, scaled by the square root of the reduced chi-squared value.

		$\omega(\mathrm{cm}^{-1})$	A_1	$\tau_1(\mathrm{ps})$	A_2	$\tau_2(\mathrm{ps})$
N3	GSB	3237	3.4 (± 2.8)	0.33 (± 0.31)	6.6 (± 2.9)	1.7 (± 0.6)
	ESA	3029	0.6 (± 0.4)	0.34 (± 0.24)	3.6 (± 0.4)	1.9 (± 0.2)
N5	GSB	3237	2.5 (± 0.3)	0.16 (± 0.04)	2.4 (± 0.2)	3.4 (± 0.4)
	ESA	3029	0.4 (± 0.1)	0.19 (± 0.05)	1.1 (± 0.1)	2.8 (± 0.1)

4.4 Relaxation mechanism

The following mechanism is proposed for the vibrational excitation of the 3237 cm^{-1} X–H stretch and its subsequent decay, schematically illustrated in Figure 4.5, which includes hypothetical vibrational energies for the v_B and v_{2B} modes, based on the difference between the known v_S = 3237 cm^{-1} and v_{S+B} = 4703 cm^{-1} modes. Pump excitation promotes some population of the LVM into v_S, creating a GSB at 3237 cm^{-1}. When subjected to probe light at 3029 cm^{-1}, this excited state the population in v_S can absorb the probe light, transferring a fraction of the defects to the v_{2S} state, and creating the ESA seen in Figure 4.3. v_{2S} is thus predicted to lie at 6266 cm^{-1}. In contrast to N_3VH^0, no other ESA features appear in the TVAS spectra, and nothing of note was found after a search in the near vicinity. In each individual sample, the lifetimes for the decay of the ESA are within error of the lifetimes of recovery of the GSB. It can thus be surmised that this system is a simpler one, involving a single-path relaxation process.

Multiple explanations are possible for the divergence in dynamics from N_3VH^0: (1) Since the transition from v_S to v_0 occurs at a faster rate than the equivalent path in N_3VH^0 (detailed in Figure 3.8), it may outcompete the rate of any relaxation into an intermediate state, such as a v_{2B} mode; (2) It may be that relaxation through the bend modes is a significantly faster process in this defect, and as such we do not see this as an additional decay path; (3) This defect may belong to a symmetry group in which such a coupling to bend modes is forbidden by a mismatch of symmetry character.

Of these hypotheses, the latter is the least feasible, as many overtones of vibrational modes contain several symmetry elements and are thus likely to have the required symmetry for population transfer. For example, if this defect were N_4VH^0, it would belong to the T_d point group, in which the two IR active modes have triply degenerate F_2 symmetry. Thus, both of the first overtones of the stretch and bend modes, v_{2S} and v_{2B}, would contain the symmetry elements $A_1 + E + F_2$. Additionally, the v_B mode having identical symmetry to v_S would hypothetically allow a transfer of population into this level, perhaps speeding up relaxation through this method. However, the overall process of population transfer to the bend modes, followed by a subsequent relaxation of these modes, would still be expected to produce an observable difference between decay of the ESA and recovery of the GSB. Thus, it can be surmised that the most likely explanation is that population transfer to bend modes is simply being outcompeted by fast direct relaxation of the stretch mode itself.

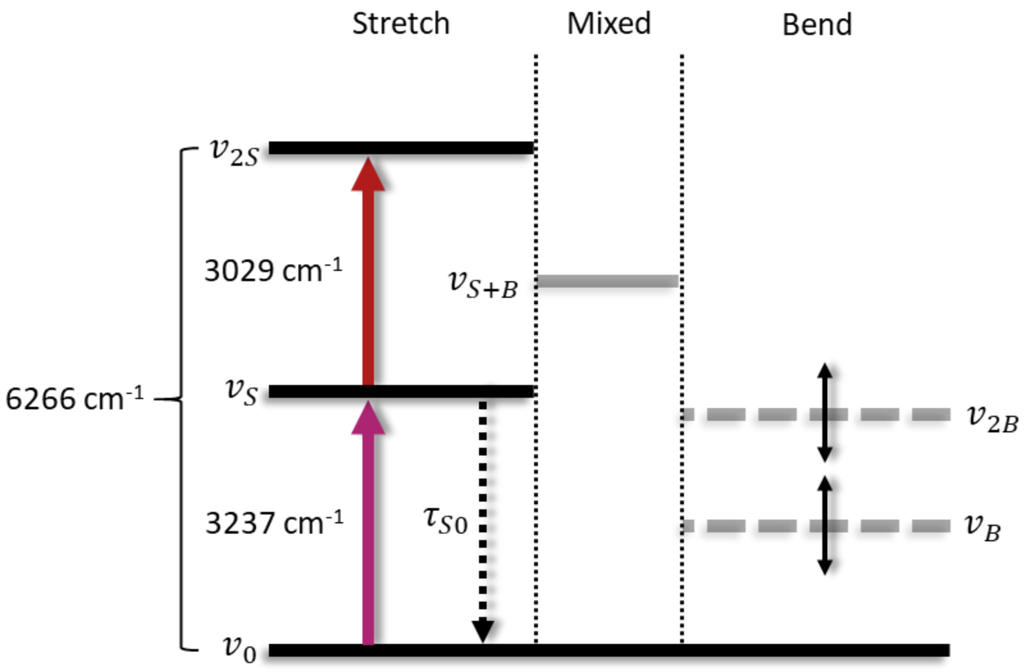

Figure 4.5 Energy level diagram of the known vibrational structure of the defect responsible for the 3237 cm^{-1} mode, including hypothetical positions for the bend and 2-bend modes, which are estimated based on the positions of the known vibrational modes. After the X–H stretch is photoexcited from v_0 to v_S, absorption of the probe pulse occurs at 3029 cm^{-1} from v_S to v_{2S}.

4.5 Relating FTIR linewidth to TVAS lifetime

As stated in Section 2.5, the total FTIR linewidth, Γ, of an individual absorption peak is defined:

$$\Gamma = \frac{1}{T_2} = \frac{1}{2\pi T_1} + \frac{1}{\pi T_2^*} + \Gamma_{\mathrm{in}} \tag{4.1}$$

where T_2 is the total dephasing lifetime, which includes contributions from the excited state lifetime for population relaxation, T_1, the lifetime for pure dephasing, T_2^*, and inhomogeneous broadening, Γ_{in}. These three components can be isolated as follows:

$$\Gamma = \Gamma_{Lorentz} + \Gamma_{\mathrm{in}} = \Gamma_{TVAS} + \frac{1}{\pi T_2^*} + \Gamma_{\mathrm{in}} \tag{4.2}$$

where $\Gamma_{Lorentz}$ is the Lorentzian component of the FTIR linewidth, including contributions from T_1 and T_2^*, and Γ_{TVAS} is the contribution to the linewidth from T_1 only, predicted using the TVAS data and Equations 2.7 and 2.8. Comparison of the observed FTIR linewidths, Γ, their Lorentzian components, $\Gamma_{Lorentz}$, and the linewidths determined from lifetimes measured using TVAS, Γ_{TVAS}, thus reveals the amount of pure dephasing and inhomogeneous broadening taking place in each sample. Good agreement is found between $\Gamma_{Lorentz}$ and Γ_{TVAS} for both N3 and N5 (Table 4.2). Therefore, the population relaxation rate accounts for the homogeneous linewidth in equilibrium, and the contribution from pure dephasing is negligible. This is to be expected, as the 3237 cm^{-1} stretch mode exhibits no temperature dependence in FTIR, and a feature containing significant contribution from pure dephasing would exhibit a temperature dependence [**14**]. Table 4.2 shows that, for both samples, the total FTIR linewidth, Γ, exceeds both $\Gamma_{Lorentz}$ and Γ_{TVAS}. We therefore surmise that both features contain inhomogeneous broadening. Further to our previous discussion in Section 3.5, results from a high concentration of additional, nitrogen-based defects in the 1000-2000 cm^{-1} region. In both samples N3 and N5, the concentration of nitrogen defects in diamond exceeds 1000 ppm, due to the presence of a high number of B-nitrogen centres and A-nitrogen centres, respectively.

Table 4.2 Linewidths of the 3237 cm^{-1} feature in each sample, determined from FTIR spectroscopy, compared to those calculated from the lifetimes obtained from transient absorption dynamics.

Sample	Γ (cm^{-1})	$\Gamma_{Lorentz}$ (cm^{-1})	Γ_{TVAS} (cm^{-1})
N3	3.9	3.1	3.1
N5	3.5	2.5	2.4

To analyse the transient absorption spectra in more detail, the time and frequency dependencies of the GSB and ESA features were investigated. Figure 4.6 shows the linewidth of the spectra of N3 and N5 at room temperature versus pump-probe time delay, while Figure 4.7 shows the time constants obtained using fits to "slices" of the transient absorption at different wavenumbers. For both the GSB and ESA features, the average FWHMs of each sample, shown in Figure 4.6, are within error of each other, as the difference between them is below the resolution of a data point in the transient absorption spectrum. The small difference between the average linewidth of the GSB feature (~5 cm^{-1}) and that of the 3237 cm^{-1} feature as it is measured in the FTIR (3.5-3.9 cm^{-1}) is due to a small amount of instrumental broadening in the TVAS detector, which has a lower spectral resolution (2 cm^{-1}) than that of the FTIR spectrometer (0.25 cm^{-1}). The average FWHM of the 3237 cm^{-1} GSB feature in both N3 and N5 is below that of the 3107 cm^{-1} GSB feature in sample N2, where inhomogeneous broadening is significant, and above that of the same feature in sample S1, where there is no inhomogeneous broadening (see Section 3.5 for this data of samples N2 and S1). It is thus surmised that the GSB linewidths obtained directly from the transient absorption spectra are therefore a reflection of the linewidth including inhomogeneous broadening. As reported for N_3VH^0 (see Section 3.5), the ESA feature has a much broader linewidth; recall that this is a consequence of the linewidth of the ESA containing contributions from the relaxation of both the v_{2S} and v_S levels, as opposed to the GSB which only contains contributions from the relaxation of the v_S level. However, in contrast to the ESA of N_3VH^0, the shape of the ESA feature here is distinctly asymmetric and includes a long tail towards lower wavenumbers, something which is currently unexplained. It is possible that asymmetry is due to inhomogeneous broadening towards lower wavenumbers. The data in Figure 4.7 does appear to show a difference in the lifetimes of the two ESA features, which are broader. The errors in the data from the GSBs is too large to show a significant difference across the wavenumber slices.

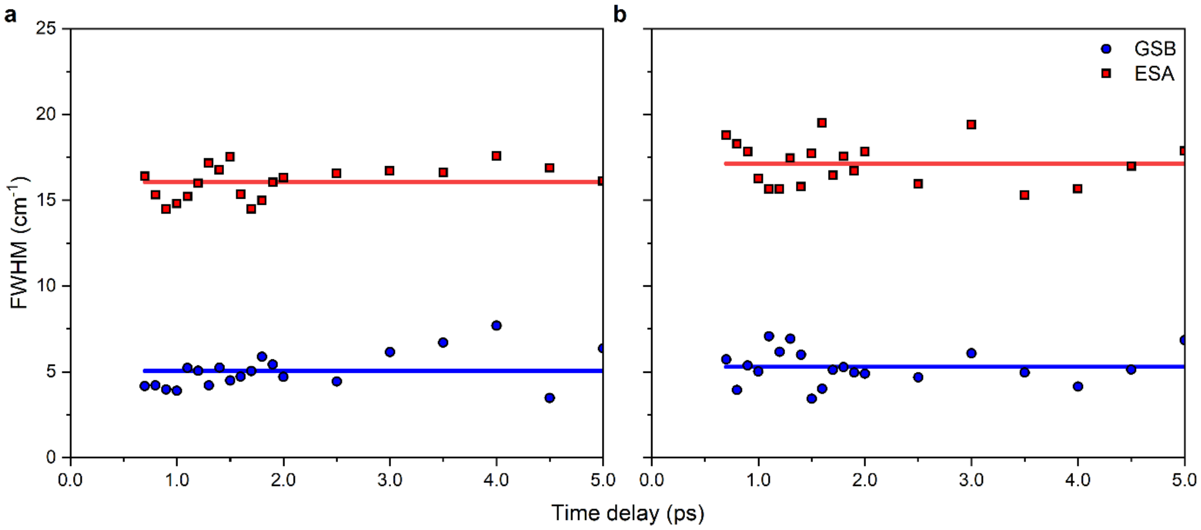

Figure 4.6 Full-width at half-maximum (FWHM) of the GSB (circles) and ESA (squares) features in the transient absorption spectra of **a,** sample N3, and **b,** sample N5, at room temperature. The solid lines represent the overall FWHM in each case.

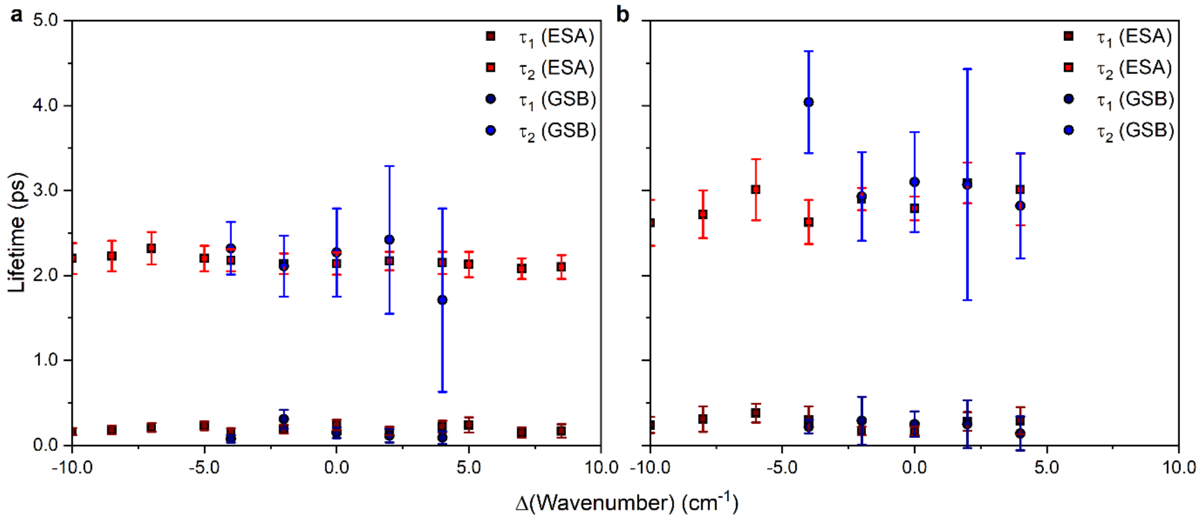

Figure 4.7 Lifetimes τ_1 and τ_2, and their standard errors, obtained from biexponential fits to the transient absorption at different wavenumbers relative to the centers of the GSB and ESA features, for: **a,** sample N3 and **b,** sample N5.

4.6 Determination of concentration from Morse potential

Two assumptions must be made for the concentration of this defect to be estimated from the absorption coefficient of the 3237 cm^{-1} feature in the FTIR. (1) We assume that there is no geometrical factor to account for, which must be assumed as there is no known defect structure; (2) For the purposes of calculating a reduced mass (see Section 2.6), we assume that the bond is between a hydrogen atom and a nitrogen atom. With this mind, the concentration of this defect can be estimated. Such a determination allows for a direction comparison with the content of N_3VH^0 and may open an avenue for using nitrogen assays to estimate the number of nitrogen atoms present in this defect. The energy spacings, 3237 cm^{-1} and 3029 cm^{-1}, directly obtained from TVAS allow simulation of the Morse potential to approximate the anharmonic potential energy, $V(r)$, of the stretch mode along the direction of the N–H bond, according to the following equation:

$$V(r) = D_e(1 - e^{-a(r-r_e)})^2 \tag{4.3}$$

where D_e is the depth of the potential well, a is the inverse width of the well, r is the distance between the two atoms involved in the bonding of the vibrational mode, and r_e is the equilibrium position. The individual vibrational energy states inside the potential energy well are determined by solving the Schrödinger equation for each state, further details of which are included in Section 2.6. Figure 4.8 shows the computed anharmonic potential energy well, including the individual vibrational states.

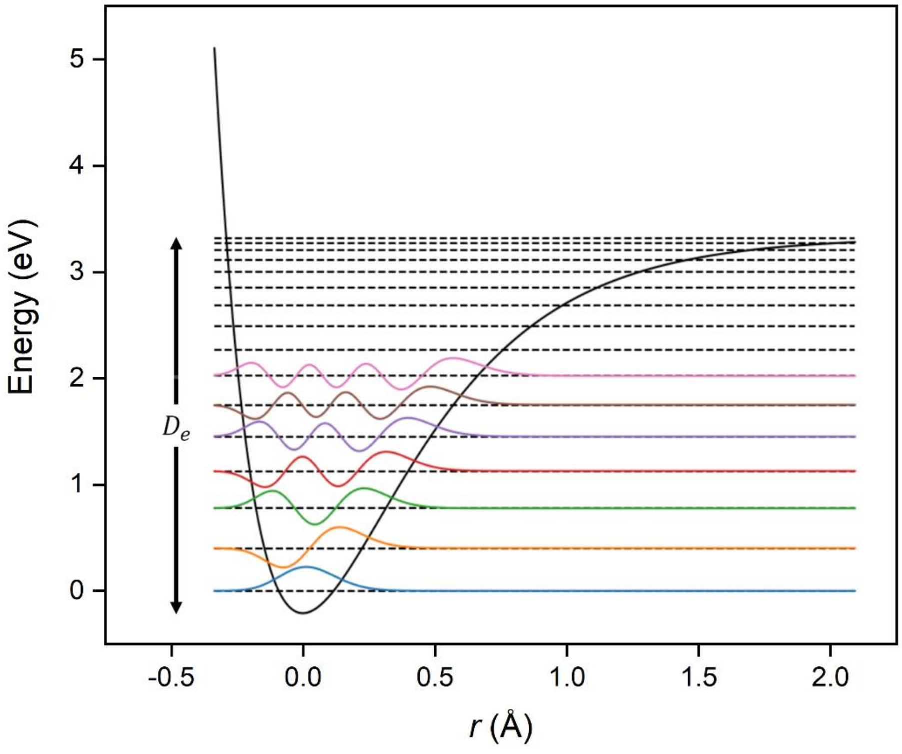

Figure 4.8 Anharmonic Morse potential energy well of the N–H stretch as a function of r, the distortion from equilibrium geometry, showing the vibrational structure.

From our simulation, we determined the following parameters for the Morse potential: well depth $D_e = 3.54\ \mathrm{eV}$ and inverse width $a = 2.41\ \times 10^{10}\ \mathrm{m}^{-1}$. The reduced well depth compared to N_3VH^0 correlates with the greater anharmonicity of this mode, as the vibrational states are closer together in a more anharmonic potential. The Morse potential allows the matrix elements D_{ij}, and hence the absorption coefficient, to be calculated directly with the defect concentration as the only free parameter. Through this method, we predict dimensionless matrix elements of $\langle\psi_1|x|\psi_0\rangle = 0.176$ for the $v_S \leftarrow v_0$ transition and $\langle\psi_2|x|\psi_1\rangle = 0.253$ for the $v_{2S} \leftarrow v_S$ transition. These cannot be directly compared to the values of the matrix elements for the 3107 cm^{-1} feature (see Section 3.6 for details), due to the unknown geometrical factor in the case of this defect. However, we can compare the ratios of the matrix elements for the transitions $v_S \leftarrow v_0$ and $v_{2S} \leftarrow v_S$, which for both cases are roughly 1:1.4. Substituting these matrix elements into Equation 2.22, we determine the ratio of the amplitude of the ESA ($\Delta\alpha_{12}$) and GSB ($\Delta\alpha_{01}$) features: the Morse potential model predicts $\frac{\Delta\alpha_{12}}{\Delta\alpha_{01}} = -1.03$. The experimental transient absorption spectra of N3 yield $\frac{\Delta\alpha_{12}}{\Delta\alpha_{01}} = -0.45$. This discrepancy is likely due to the vastly increased linewidth of the ESA feature over the GSB, even when compared to the analogous features in N_3VH^0, where the experimental and theoretical amplitude ratios do match (see Section 3.5).

By using the measured FTIR absorption and the matrix elements from the Morse potential model we can predict the defect concentration of any sample where the 3237 cm^{-1} line is present, assuming optical absorption occurs between two quantum states with a Lorentzian lineshape. The defect concentration can thus be related to the integrated area of its 3237 cm^{-1} feature by using the following calibration factor: $[3237](\mathrm{ppb}) = (27 \pm 4) \times I_{3237}(\mathrm{cm}^{-2})$. The results in Table 4.3 show concentrations of the 3237 cm^{-1} defect, assuming no geometrical factor, as compared to those of N_3VH^0 in the same sample.

Table 4.3 Concentrations of the 3237 cm^{-1} defect, determined using the Morse potential model, compared to the N_3VH^0 concentration measured for the same sample.

Sample	$[\mathbf{3237}]_{Morse}(\mathbf{ppm})$	$[\mathbf{N_3VH^0}]_{Morse}(\mathbf{ppm})$
N1	2.8 ± 0.4	21.8 ± 2.0
N3	2.9 ± 0.4	22.9 ± 2.1
N5	0.1 ± 0.1	1.1 ± 0.1

It can be observed in these samples that when the N_3VH^0 concentration is higher, so too is the concentration of the 3237 cm^{-1} defect. It is therefore possible that there is a relationship between the two defects. However, the ratio of the two defect concentrations is not constant for these three samples, and the two defects have been shown not to correlate in the past [**2**]. We thus surmise that the 3237 cm^{-1} feature does not arise from N_3VH^0, but from a similar defect.

4.7 Conclusions and future work

Transient vibrational absorption spectroscopy was employed to determine the lifetime of processes relating to the 3237 cm^{-1} stretch mode (v_S) found in many diamond samples. The discovery of an excited state absorption at 3029 cm^{-1} reveals that the v_{2S} state of this defect lies at 6266 cm^{-1} in the IR absorption spectrum, and indicates a strong anharmonicity in this mode, greater than that observed for the N_3VH^0 defect. This determination will aid future computational studies seeking to formally identify the structure of the defect. Calculations based on the Morse potential allow a calibration between the concentration of this defect and the intensity of its X–H stretch mode, subject to its directionality with respect to the (100) face of the diamond: $[3237](\mathrm{ppb}) = (27 \pm 4) \times I_{3237}(\mathrm{cm}^{-2})$.

With regards to the vibrational dynamics, decay from v_S is dominated by a single pathway – a direct decay back down to the ground state. The contrasting dynamics between this vibrational mode and that of the 3107 cm^{-1} stretch mode is likely reflected by the different structure and thus symmetry character of the two defects responsible for the modes. The variation in excitation lifetime between the two samples used in this study (~1.8 ps for N3 and ~3.0 ps for N5) is speculated to arise from the widely different defect populations present in each. It is suggested that the presence of B-nitrogen centres better mediates vibrational transfer than A-nitrogen centres, though this is by no means a certainty. Further study of this defect using magnetometry and computational studies are required for a formal identification of its structure.

4.8 References

1. J. J. Charette, *Physica* **1959**, *25*, 1303–1312.

2. G. S. Woods, A. T. Collins, *J. Phys. Chem. Solids* **1983**, *44*, 471–475.

3. K. Iakoubovskii, G. J. Adriaenssens, *Diam. Relat. Mater.* **2002**, *11*, 125–131.

4. F. De Weerdt, Y. N. Pal'yanov, A. T. Collins, *J. Phys. Condens. Matter* **2003**, *15*, 3163–3170.

5. B. Rondeau, E. Fritsch, M. Guiraud, J. P. Chalain, F. Notari, *Diam. Relat. Mater.* **2004**, *13*, 1658–1673.

6. C. Van Der Bogert, C. Smith, T. Hainschwang, S. McClure, *Gems Gemol.* **2009**, 45, 20-37.

7. E. Fritsch, T. Hainschwang, L. Massi, B. Rondeau, *New Diam. Front. Carbon Technol.* **2007**, *17*, 63–89.

8. C. V. Peaker, *First Principles Study of Point Defects in Diamond,* Ph.D. Thesis, University of Newcastle, UK, **2018**.

9. T. Gu, S. Ritterbex, T. Tsuchiya, W. Wang, *Diam. Relat. Mater.* **2020**, *108*, 107957.

10. S. R. Boyd, I. Kiflawi, G. S. Woods, *Philos. Mag. B* **1995**, *72*, 351-361.

11. I. Kiflawi, A. E. Mayer, P. M. Spear, J. A. Van Wyk, G. S. Woods, *Philos. Mag. B* **1994**, *69*, 1141-1147.

12. S. R. Boyd, I. Kiflawi, G. S. Woods, *Philos. Mag. B* **1994**, *69*, 1149-1153.

13. F. S. Gentile, S. Salustro, M. Causa, A. Erba, P. Carbonniere, R. Dovesi, *Phys. Chem. Chem. Phys.* **2017**, *19*, 22221–22229.

14. J. L. Skinner, *Ann. Rev. Phys. Chem.* **1988**, *39*, 463-78.

5 The effect of ultraviolet excitation on hydrogen defects in diamond

5.1 Background

Unlike the infrared (IR), transient absorption spectroscopy has been employed in the past to excite electronic states in diamond using light in the ultraviolet (UV) or visible (Vis) range. There are existing reports in the literature of experiments detecting the promotion of free carriers into the diamond conduction band using UV light of a higher energy than the diamond band gap. Additionally, some studies have excited electronic states pertaining to specific defect centres in diamond. We summarise the previously reported UV/Vis pump and IR probe studies of diamond and its defects in the remainder of this section.

Popelář *et al.* conducted a study of transient vibrational absorption spectroscopy (TVAS) applied to type IIa diamond, which contained a negligible presence of defects (< 5 ppb nitrogen concentration) [**1**]. Under UV excitation (λ_{pump} = 200 nm), the incident photons had sufficient energy to induce the excitation of free carriers from the diamond valence band into its conduction band. Absorption of light in the IR range (ω_{probe} = 1250-3125 cm^{-1}) caused these free carriers to produce a broad horizontal absorption across the spectrum, known as a free carrier absorption (FCA) background. Popelář *et al.* reported a two-component FCA background decay. Time constants τ_1 = 38 ps and τ_2 = 1800 ps were recorded when the probe was set to a wavenumber of 1250 cm^{-1}.

Ultrafast pump-probe experiments exciting in the UV range have also been carried out on specific defect sites in diamond. Ulbricht *et al.* have published studies on the relaxation dynamics of the single substitutional nitrogen centre, N_S^0 [**2**] and the nitrogen-vacancy centre, NV^- [**3,4**]. Under excitation in the visible range (λ_{pump} = 400 nm) and detection using a probe in the IR range (ω_{probe} = 1320-1360 cm^{-1}), Ulbricht *et al.* were able to induce and observe charge transfer in N_S^0 [**2**]. The pump beam induced excitation of electrons from N_S^0 into the diamond conduction band, creating free electrons and N_S^+ defects, the latter of which manifested as an absorption feature at 1332 cm^{-1}. A second absorption feature at 1349 cm^{-1} was also observed. This feature was confirmed by theoretical simulations to arise due to the formation of N_S^- defects, produced by recombination of the now free electrons with persisting N_S^0 defects. Employing transient absorption detection in the IR range thus enabled the detection of the negative charge state of single substitutional nitrogen, N_S^-, for the first time. They did not report a specific lifetime for the neutralisation of these charge states; however, it was stated that this process is completed after 10 ns.

Subsequently, Ulbricht *et al.* used transient absorption experiments exciting in the visible range (λ_{pump} = 610-640 nm) and probing in both the visible (λ_{probe} = 580-700 nm) and IR (ω_{probe} = 9615 cm^{-1}) ranges to observe dynamics related to electronic states of the NV^- centre [**3,4**]. By comparing the spectra that arise from excitation of its zero- and one-phonon lines, they were able to indirectly measure a fast relaxation time (< 60 fs) for the first excited vibrational state of the electronically excited NV^- centre. However, they were unable to explain the mechanism behind it. By probing in the IR range, they were able to measure the lifetime of an electronic transition associated with NV^- to be 100 ps. Thus, it has been shown that excitation in the UV/Vis range, and probing in the IR range, can offer insight into the lifetimes for charge transfer, relaxation from excited defect states, and, indirectly, the lifetime for relaxation of vibrational states of specific defects.

At present, there are no examples of studies akin to those by Ulbricht *et al.* on hydrogen-related defects, such as N_3VH^0. However, whilst no electronic states of N_3VH^0 have been identified by experiment, predictions of its electronic band structure have been made using computational models [**5,6**]. Two N_3VH^0 states were predicted to lie close to the diamond valence band. The lower of these states, assigned to A_1 symmetry character, included electronic density from the three lone pairs and the C–H stretch in N_3VH^0. A slightly higher degenerate electronic state, assigned to E symmetry character, is more associated with the nitrogen lone pairs. Finally, the excited electronic states were predicted to exist at an energy state slightly lower than the diamond conduction band. It is therefore feasible that excitation using light of energy just below the diamond band gap could induce electronic excitation into these bands. The gap for excitation of N_3VH^0 was predicted by Gentile *et al.* to be roughly 240 nm [**6**].

In this chapter, we investigate the effect of UV excitation on our diamond samples. We look generally at the excitation and relaxation of free carriers in samples containing low (~50 ppm) and high (> 2000 ppm) concentrations of nitrogen, enabling a comparison of the lifetime for the relaxation of free carriers against the results reported by Popelář *et al.* for high purity diamond. Thus, the effect of defects on the lifetime for free carrier relaxation can be studied. We also focus on the specific defect features already studied in Chapters 3 and 4, these being the N_3VH^0 defect and the unknown defect responsible for the local vibrational mode (LVM) at 3237 cm^{-1}. Studying the excitation and decay of the electronic states associated with these defects allows us to further our understanding of their energy states. Additionally, monitoring the decay of the electronic states opens the possibility of exploring higher overtones of the vibrational modes of these defects. We thus obtain a more complete picture of the vibronic structure and dynamics of a defect system by exciting in the UV, in addition to the IR. Our existing knowledge of the vibrational dynamics, reported in Chapters 3 and 4, will aid our understanding of the data accrued in this chapter.

5.2 Absorption in equilibrium

To observe the effect of a significant defect concentration on the absorption of diamond in the UV/Vis region, we took steady-state UV/Vis spectra of three natural diamonds, N1, N2 and N3, all of which originated from the Argyle mine. N1 and N2 both contain > 2000 ppm of nitrogen, most of which can be attributed to the B-nitrogen centre, N_4V^0. In N1, the total nitrogen concentration is significantly lower, at roughly 50 ppm. Section 2.4 provides further details on these samples. The UV/Vis spectra are shown in Figure 5.1.

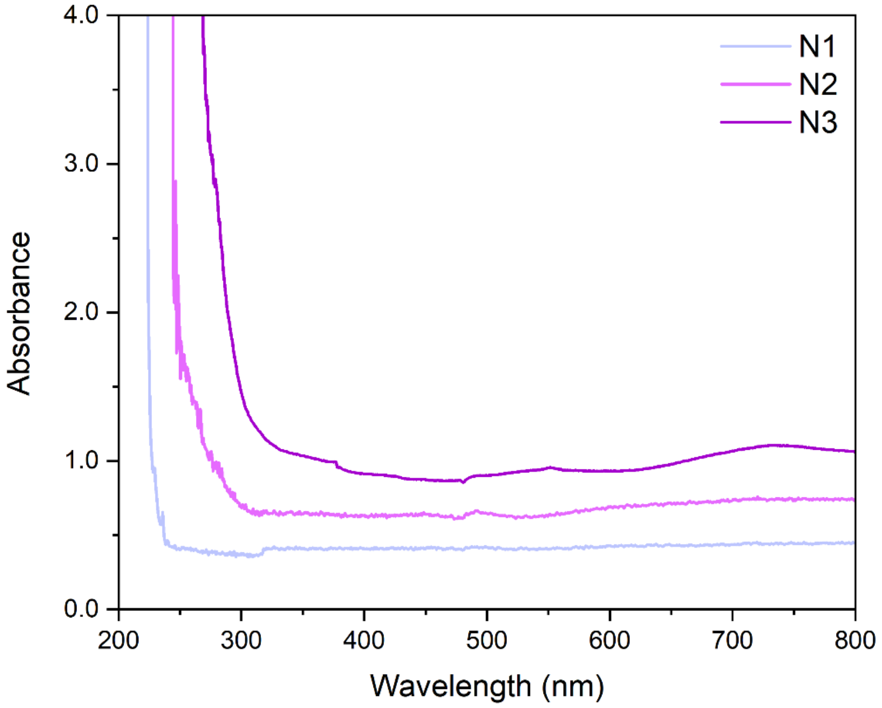

Figure 5.1 UV/Vis absorbance spectrum of violet natural diamonds N1, N2 and N3, showing the effect of diamond thickness and defect concentration on overall absorbance.

Irrespective of its defect concentration, a diamond sample absorbs strongly enough to saturate the spectrum at short wavelengths, $\lambda < 225$ nm, where the energy of the incoming photons exceeds the diamond band gap. This is observed most clearly in diamonds with relatively low nitrogen concentration, such as N1 (~50 ppm), where there is a sharp change in absorption. Excitation at wavelengths shorter than the 225 nm threshold induces the promotion of free carriers into the conduction band, as observed by Popelář *et al.* in their work [**1**]. Any extra absorption seen at longer wavelengths, $\lambda > 225$ nm, is due to a significant population of defects creating states inside the band gap. It can be observed from our UV/Vis data for N2 and N3 that there is now an absorption ramp, which has broadened out into longer wavelengths. This is due to a large population of defects that have either: (1) created empty states below the conduction band edge, allowing electrons to be excited from the valence band into these states; (2) broadened out the valence band to a higher energy; (3) created filled states above the valence band edge. Absorption ramps such as those in the data for N2 and N3 are commonly reported in the UV/Vis spectra of diamonds with a high proportion of single substitutional nitrogen, where the extra electrons from nitrogen replacing carbon manifest as deep donor levels close to the valence band [**7**]. Crucially, the shift to an absorption ramp means that excitation at wavelengths in the range 225 nm $< \lambda <$ 300 nm can now promote carriers into the conduction band.

5.3 Transient absorption

Using TVAS, we detect the differences in IR absorption created following UV photoexcitation (as opposed to the IR excitation used in Chapters 3 and 4). In Section 5.3.1., we extract the FCA background from both N1 and N2 and compare our observations to those previously observed in high purity diamond [**1**]. Sections 5.3.2. through to 5.3.4. focus on the effect of UV excitation on the features studied in Chapters 3 and 4, those being the two stretch modes at 3107 cm^{-1} and 3237 cm^{-1}, and their associated vibrational overtones.

5.3.1 Free carrier absorption

Before focusing on specific defect features, we look for the free carrier absorption (FCA) background. Under excitation at 240 nm, the probe was scanned across the IR (υ_{probe} = 1300-3300 cm^{-1}). To facilitate this broad sweep, a lower-resolution diffraction grating (6.0 µm blaze, 100 lines mm^{-1}) was used, producing a resolution of 7 cm^{-1} at a wavenumber of 3200 cm^{-1}, compared to 2 cm^{-1} for the higher-resolution grating reported in Section 2.3. Using a lower-resolution diffraction grating decreased the overall scan time but did not allow us to zone in on specific features. A section of the UV pump, IR probe transient absorption spectra of samples N1 and N2 are presented in Figure 5.2 at different pump-probe time delays, Δt, in the range 3000-3200 cm^{-1}. The broad horizontal absorption, which persists across the entire IR region being swept, is the same as the FCA reported by Popelář *et al.* in their work [**1**]. A feature at ~3107 cm^{-1} can be seen in the N2 data in Figure 5.2b and is discussed in detail in the following section, where higher resolution scans allowed for its line shape to be resolved.

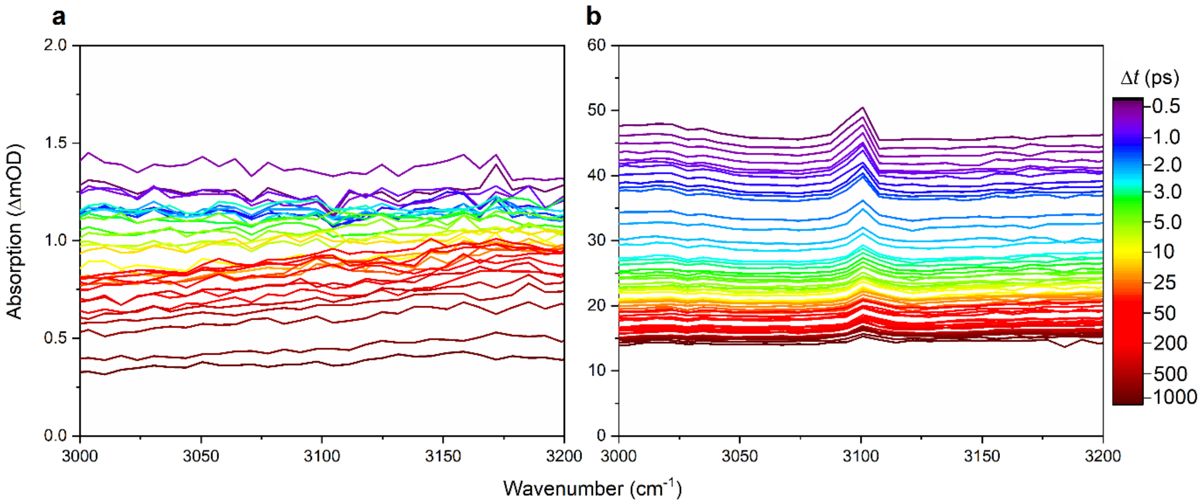

Figure 5.2 TVAS results for natural diamond samples N1 and N2. Transient absorption spectra for pump-probe delays 1 ps < Δt < 1250 ps, for pump excitation centred at 240 nm and probed in the range 3000-3200 cm^{-1}.

Taking an average of each data point in the range of 3150-3200 cm^{-1} produced the transients shown in Figure 5.3. For sample N1, we extract two time constants for free carrier relaxation: $\tau_1 = 3.3 \pm 0.6$ ps and $\tau_2 = 1750 \pm 80$ ps. τ_2 is comparable to the long relaxation time extracted by Popelář *et al.* in their measurements (pumping at 200 nm and probing at 1250 cm^{-1}) and is consistent with the slow component of free carrier recombination [**1**]. However, τ_1 is much shorter here (c.f. the 38 ps reported by Popelář *et al.*). This difference could be due to several factors, including: (1) The lower temperature of their measurements (250 K, whereas our experiments were carried out at room temperature); (2) The higher pump fluence used in our experiments (1.22 mJ cm^{-2}, as opposed to 0.34 and 0.5 mJ cm^{-2} reported by Popelář *et al.*); (3) The presence of a small concentration (~50 ppm) of nitrogen defects in N1, as opposed to the type IIa diamond used in their work, with nitrogen concentration < 5 ppb. Qualitatively, we observe the same two-component decay for free carriers in N1 as in type IIa diamond.

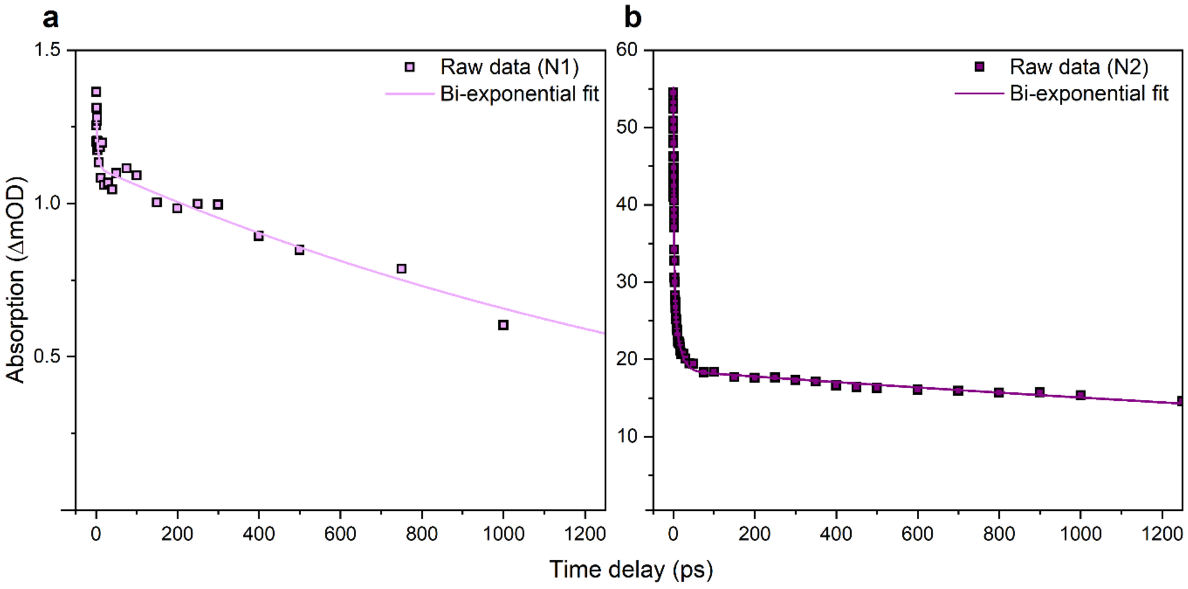

Figure 5.3 Transient fits of TVAS data for **a,** natural diamond sample N1 and **b,** natural diamond sample N2. The absorption differencefor both transients is measured as an average of data in the wavenumber range 3150-3200 cm^{-1} (squares). Solid lines represent the multi-exponential fits of each data set.

For N2, we extract two time constants: $\tau_1 = 3.8 \pm 0.1$ ps and $\tau_2 = 4300 \pm 100$ ps. Here, τ_1, the short component of the decay, is within error of the value recorded for N1. However, we observe that τ_2, the long component of decay, is significantly greater than its analogous component in both N1 and in the sample studied by Popelář *et al* [**1**].

We speculate that the increased relaxation time of N2 is due to the high concentration of defects in this sample. These produce defect states inside the diamond band gap, which act as traps according to the Shockley-Read-Hall model [**8**], hindering the relaxation of free carriers back down to the valence band. This results in the longer lifetime observed in sample N2. Figure 5.4 illustrates the mechanisms taking place in the system upon excitation with UV light.

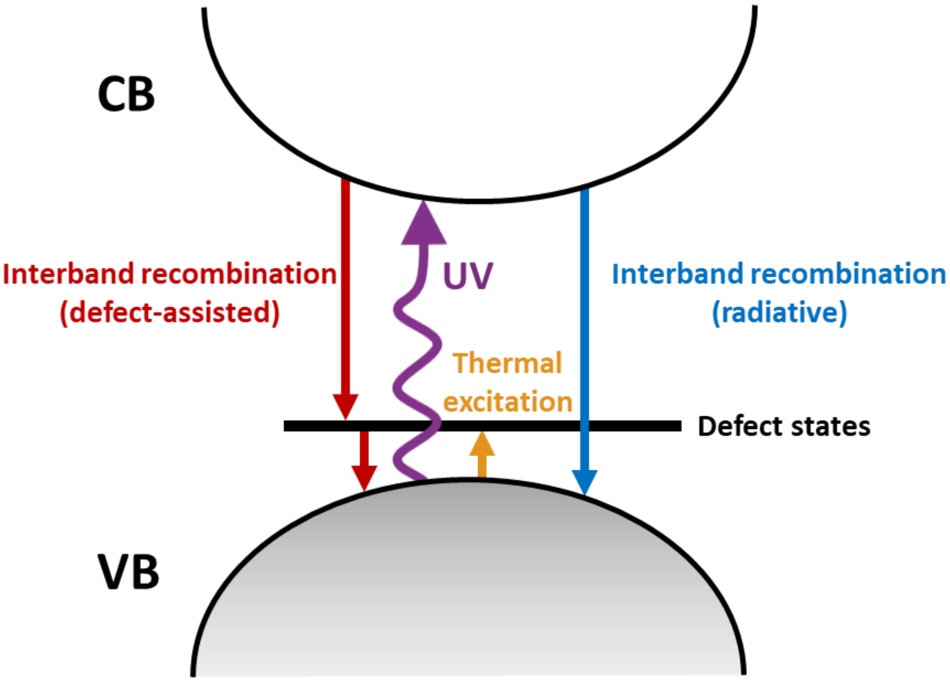

Figure 5.4 Schematic showing the various processes taking place when UV light is shone on the diamond sample. Free carriers absorb in the UV and are promoted into the diamond conduction band (CB). They relax back down to the valence band (VB) by one of two methods; either via radiative recombination, or recombination mediated by defect states, the latter of which being the slower process.

5.3.2 Fabry-Pérot oscillations

In the high-resolution spectra around the 3107 cm^{-1} and 3237 cm^{-1} absorption features (see Figures 5.8 and 5.11), there are observed oscillating fringes. These are known as Fabry-Pérot oscillations, and arise due to a change in the diamond refractive index in regions penetrated by the UV pump beam. The incident pump alters the reflectivity of the sample surface, thus creating the spikes observed across the spectrum. Similar behaviour has previously been reported in the spectra of other crystalline materials [**9-11**]. Due to the low-resolution grating used in the previous section, the Fabry-Pérot oscillations averaged out across each pixel and were not observed.

The Fabry-Pérot oscillations disappear at later times (Δt > 50 ps) once the effect of excitation becomes diminished by the diffusion of the excited free carriers. Figure 5.6a shows the UV pump intensity profile, which is exponentially dependent on the thickness of the diamond, z, and the penetration depth, δ, according to:

$$I(z) \propto e^{-z/\delta} \tag{5.1}$$

Since the promotion of free carriers can only occur in regions that absorb UV light and become excited, the initial free carrier profile in a diamond, shown in Figure 5.6b, matches the intensity profile of the pump. As the free electrons and holes diffuse away from the surface, from regions of high to low free carrier concentration, the free carrier profile levels off. The surface concentration decreases rapidly, on a timescale faster than electron-hole recombination. This causes the refractive index to return to its equilibrium level.

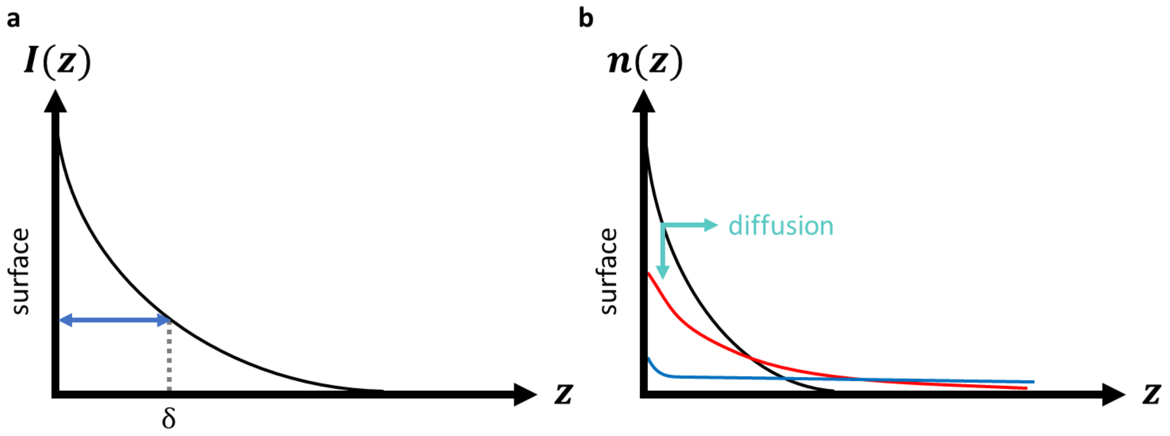

Figure 5.6 Profile plots of **a,** The intensity $I(z)$ of the UV pump incident on the surface of a diamond sample. **b,** The free carrier concentration $n(z)$ of a diamond sample immediately (black line), at short times (red line) and at long times (blue line) after excitation.

Figure 5.7 demonstrates how the reflectivity changes at times after UV excitation. Initially, the free carriers are concentrated at the surface and reflect a larger proportion of both incoming IR light, and light that is reflected back through the diamond. This effect is diminished at late times, when the free carriers have diffused throughout the diamond and the reflectivity at the surface more closely resembles the situation when the pump is turned off.

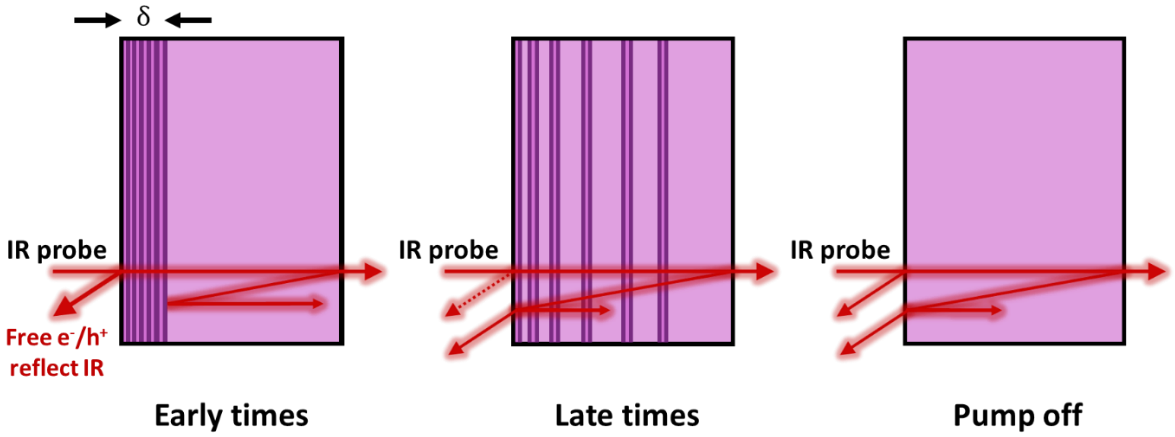

Figure 5.7 Illustration of the change in reflectivity at the diamond surface in response to UV pump excitation, at early and late times, in comparison to the reflectivity when the pump is off.

5.3.3 The 3107 cm^{-1} stretch mode

Transient absorption measurements were taken in the region of the 3107 cm^{-1} stretch mode using the high-resolution grating from the IR pump, IR probe experiments (3.5 µm blaze, 300 lines mm^{-1} resolution). Subtraction of the FCA background and subsequent smoothing, using a Savitzky–Golay filter with a 5-point window [**12**], produced the spectra shown in Figure 5.8.

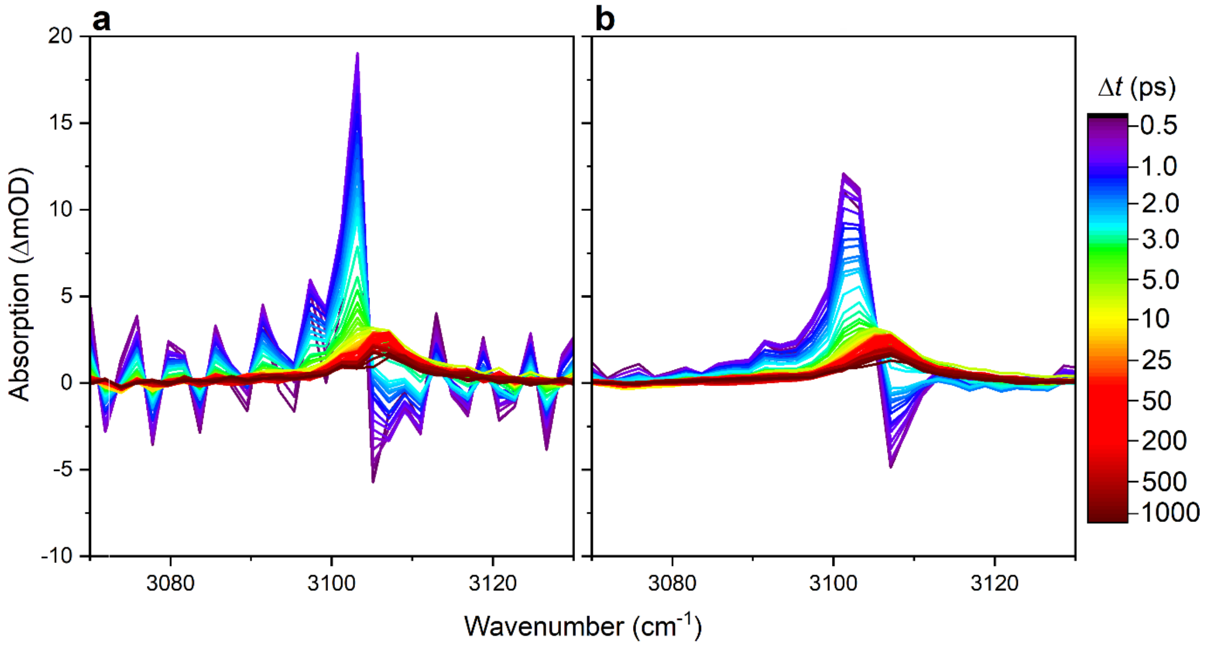

Figure 5.8 TVAS results for natural diamond N2, after subtraction of the FCA background, **a,** before and **b,** after smoothing. Transient absorption spectra for pump-probe delays 0 ps $< \Delta t < 1000$ ps, for pump excitation centred at 240 nm and probed around 3107 cm^{-1}.

An S-shaped feature is observed, indicating a redshift in the peak position of the C–H stretch mode from 3107 cm^{-1} to 3102 cm^{-1}. At early time delays, 1 ps $< \Delta t <$ 5 ps, the feature loses its S-shape and reverts to a positive feature. At time delays $\Delta t >$ 5 ps, the feature shifts once more, returning to its original peak position of 3107 cm^{-1}. This feature persists at time delays beyond those accessible given the length of the delay stage used in this experiment.

In terms of the dynamics, Figure 5.9 reports the absorption change recorded at 3102 cm^{-1} and 3107 cm^{-1}, against the time delay. The transient for the latter clearly shows a three-component decay, with an initial lifetime reflecting the disappearance of the S-shape and blueshift back to 3107 cm^{-1}, and a two-component decay of the subsequent feature. A three-component decay may also be fit to the transient at 3102 cm^{-1}. The data from these fits are recorded in Table 5.1, alongside the fit of the FCA relaxation in N2. In both cases, τ_1 (~1.2 ps) and τ_2 (~15 ps) are significantly faster than τ_3 (> 2000 ps), which, for the transient of 3107 cm^{-1}, exceeds the longest time delay allowed by the experimental setup. τ_1 is the time constant for blueshift of the feature back to 3107 cm^{-1}, whilst τ_2 and τ_3 are related to the subsequent relaxation of the mode itself. τ_3 is of the same order as the long component of the FCA relaxation. As such, it is likely related to the trapping of free carriers that are relaxing back to the valence band.

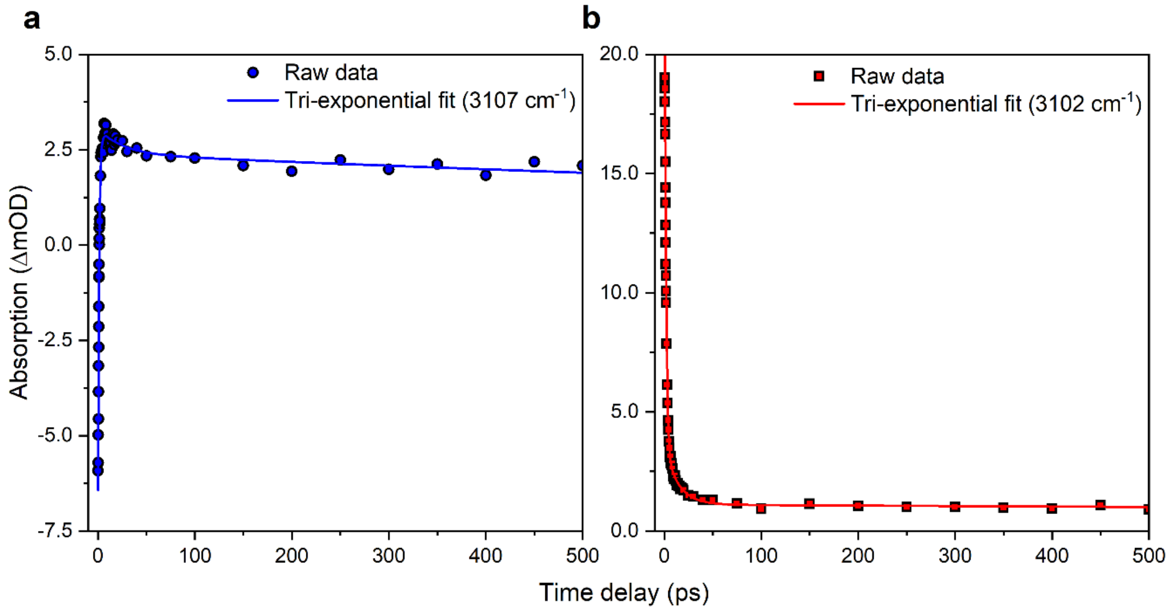

Figure 5.9 TVAS for natural diamond sample N2, using unfiltered data. **a,** Absorption difference at 3107 cm^{-1} (blue circles), measured at the wavenumber of its peak maximum, and a tri-exponential fit (solid line). **b,** Absorption difference at 3102 cm^{-1} (red squares), measured at the wavenumber of its peak maximum, and a tri-exponential fit (solid line).

Table 5.1 Decay lifetimes from transient fits of data around 3107 cm^{-1} from N2, at a temperature of 298 K, compared to the lifetimes of FCA decay. All errors are standard errors, scaled by the square root of the reduced chi-squared value.

$\omega(\mathrm{cm}^{-1})$	A_1	$\tau_1(\mathrm{ps})$	A_2	$\tau_2(\mathrm{ps})$	A_3	$\tau_3(\mathrm{ps})$
FCA	32.3 (± 0.2)	3.8 (± 0.1)	18.9 (± 0.1)	4300 (± 100)	N/A	N/A
3102	16.5 (± 0.3)	1.4 (± 0.1)	2.4 (± 0.3)	14.0 (± 2.9)	1.1 (± 0.1)	> 2000
3107	-9.2 (± 0.1)	1.1 (± 0.1)	0.6 (± 0.1)	19.9 (± 8.9)	2.4 (± 0.1)	2100 (± 300)

The following explanation, schematically illustrated in Figure 5.10, is proposed to explain the S-shaped feature and its dynamics. The C–H stretch mode is largely promoted to the vibrational ground state of its first electronically excited state (e_1, v_0). Excitation into this level changes the electronic structure of the mode. This causes the vibrational mode to redshift, resulting in both the S-shape and the shift in peak wavenumber to v_S = 3102 cm^{-1}. The initial lifetime, τ_1 ~1.3 ps, represents the lifetime for electronic state decay, from e_1 to e_0. The second lifetime, τ_2 ~15 ps, is assigned to the vibrational relaxation of the ground electronic state. τ_2 is higher than the vibrational relaxation lifetimes of N_3VH^0, as reported in Section 3.3. However, these lifetimes were solely recorded for population excited into the first overtone, v_1. The value of 15 ps is consistent with relaxation from (e_1, v_0) into vibrational overtones of the electronic ground state, (e_0, $v_{\geq 1}$) – a vibronic transition. Evidence of population of these higher vibrational states is garnered from the presence of a group of ESA features in the wavenumber range 2880-3080 cm^{-1}, discussed in Section 5.3.5. The long time constant, τ_3 > 2000 ps, is related to the relaxation free carriers. During their relaxation from the conduction band back down to the valence band, they become trapped in the defect states that exist in the band gap. One such state being the N_3VH^0 stretch mode, this explanation accounts for the remaining population at time delays beyond our experimental capability.

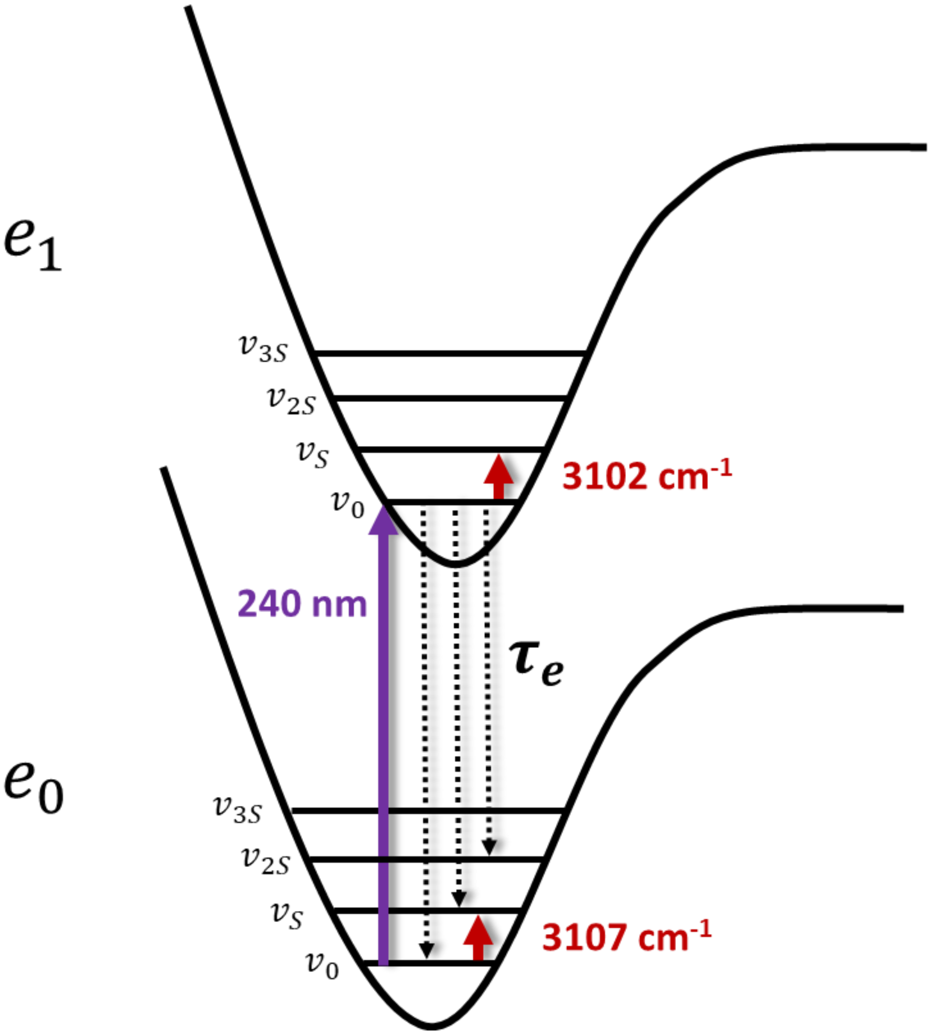

Figure 5.10 Schematic of the anharmonic potential wells of the ground and first excited electronic states of N_3VH^0, explaining the observed dynamics.

5.3.4 The 3237 cm^{-1} stretch mode

Further measurements were taken with the probe shifted to the 3237 cm^{-1} stretch mode, the focus of our study in Chapter 4. Using the same experimental setup reported in Section 5.3.3, and after subtraction of the FCA background and smoothing, the spectra shown in Figure 5.11 were obtained.

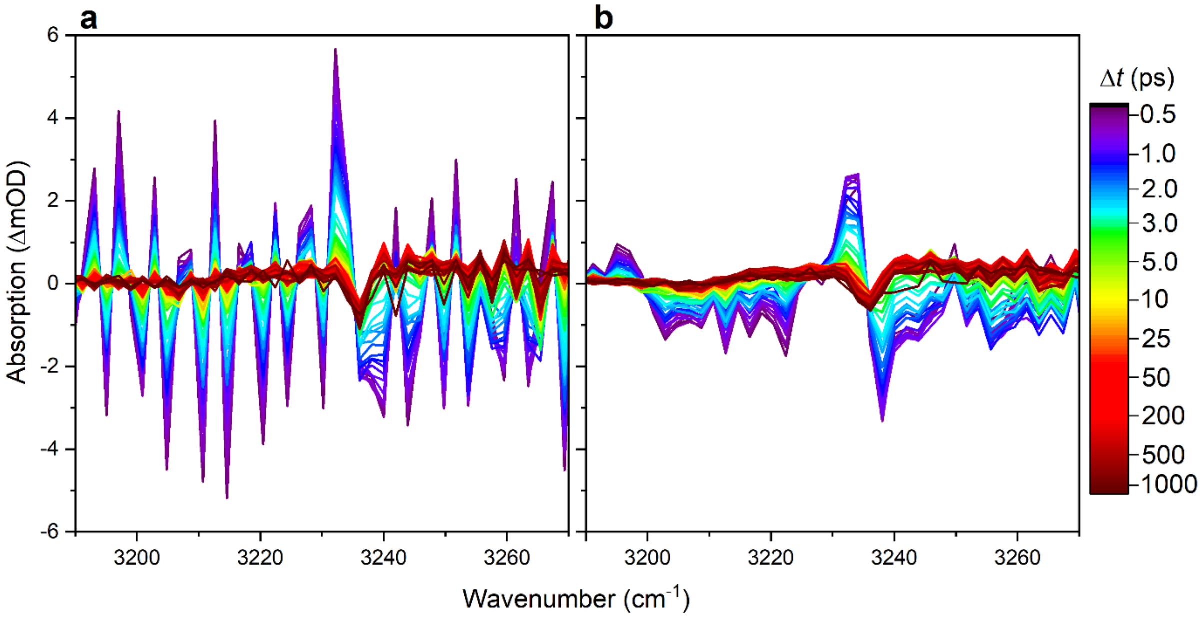

Figure 5.11 TVAS results for natural diamond sample N2, after subtraction of the broad absorption background, **a,** without and **b,** with a Savitzky–Golay smoothing filter. Transient absorption spectra for pump-probe delays 0 ps < Δt < 1000 ps, for pump excitation centred at 240 nm and probed in the region around 3237 cm^{-1}.

Another S-shape feature is observed initially, indicating that the peak of the feature has redshifted to 3233 cm^{-1}. At late times, the peak of the feature has shifted back to 3237 cm^{-1}. This suggests that electronic excitation also occurs in this system. However, in this case, the prevailing feature beyond our experimental capability is a negative feature.

Figure 5.12 reports the absorption change recorded at 3233 cm^{-1} and 3237 cm^{-1}, against the time delay. The data from these fits is recorded in Table 5.2, alongside the fit of the FCA relaxation in N2. Similar τ_1 (~1.4 ps) and τ_2 (~10 ps) time constants to those in Table 5.1 are reported for the decay of the peak at 3233 cm^{-1}. Additionally, both transients contain a long component of relaxation, indicating that there is a possibility that free carriers are being trapped by the states of this defect.

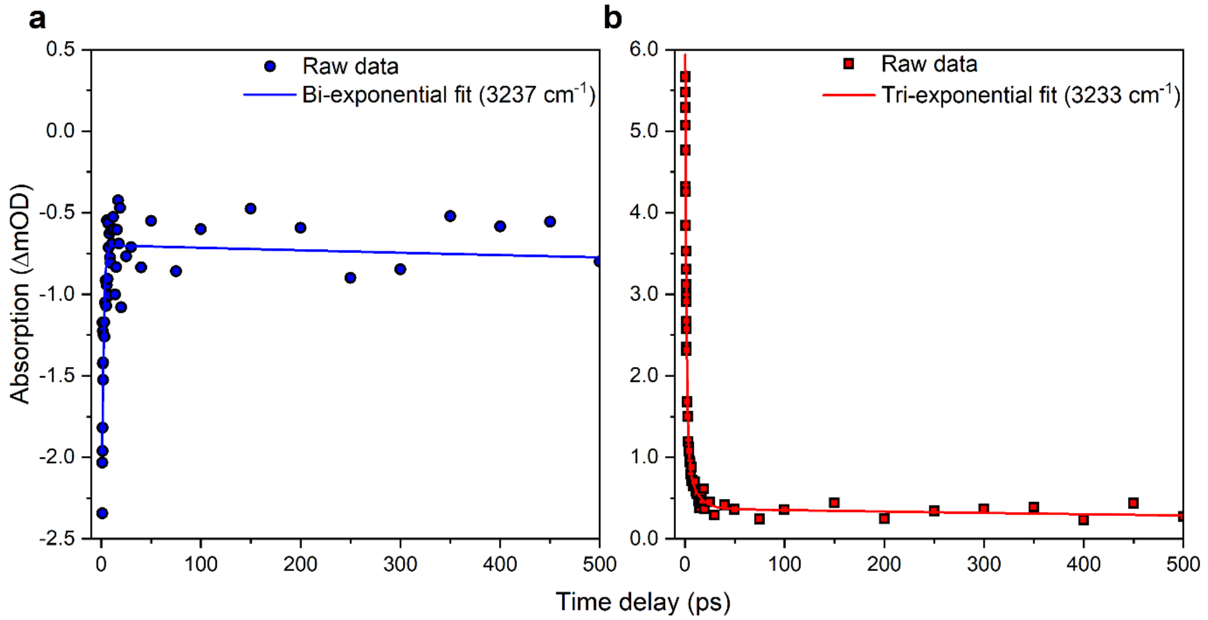

Figure 5.12 TVAS for natural diamond N2, using unfiltered data. **a,** Absorption difference at 3237 cm^{-1} (blue circles), measured at the wavenumber of their peak maxima, and a bi-exponential fit (solid line). **b,** Absorption differenceat 3233 cm^{-1} (red squares), measured at the wavenumber of its peak maximum, and a tri-exponential fit (solid line).

Table 5.2 Decay lifetimes from transient fits of data around 3237 cm^{-1} from N2, at a temperature of 298 K, compared to the lifetimes of FCA decay. All errors are standard errors, scaled by the square root of the reduced chi-squared value.

$\omega(\mathrm{cm}^{-1})$	A_1	$\tau_1(\mathrm{ps})$	A_2	$\tau_2(\mathrm{ps})$	A_3	$\tau_3(\mathrm{ps})$
FCA	32.3 (± 0.2)	3.8 (± 0.1)	18.9 (± 0.1)	4300 (± 100)	N/A	N/A
3233	4.9 (± 0.2)	1.3 (± 0.1)	0.7 (± 0.1)	9.5 (± 3.0)	0.4 (± 0.1)	1900 (± 900)
3237	-2.6 (± 0.1)	1.6 (± 0.1)	0.5 (± 0.1)	>3000	N/A	N/A

Parallels may be drawn between these spectra and those in Figure 5.8. The primary difference between this data and that taken for the N_3VH^0 C–H stretch mode is the prevailing negative feature at late times, in contrast to the positive feature observed in Figure 5.8. One explanation for this prevailing bleach is that the 3237 cm^{-1} mode is coupled to another mode, in which it becomes trapped as it relaxes back to its electronic ground state. Further study is needed to identify this mode, if it does exist. The difference between a prevailing absorption feature at 3107 cm^{-1} and a prevailing bleach at 3237 cm^{-1} suggests either a stark difference between the electronic charge or the structure of the two defects, else it could indicate a relationship between the two where population of 3237 cm^{-1} has been transferred to 3107 cm^{-1}.

5.3.5 The vibrational overtones of 3107 cm^{-1} and 3237 cm^{-1}

Movement of the IR probe to the region of 2880-3080 cm^{-1} revealed several features after subtraction of the FCA background. The spectrum in this region is shown in Figure 5.13. For this scan, the low-resolution grating was used. As such, the Fabry-Pérot oscillations were averaged out, and no smoothing filter was required to treat this data.

Four distinct ESA features can be seen in the spectrum, including those at 2963 cm^{-1} and 3029 cm^{-1}, which were reported in Sections 3.3 and 4.3 respectively. Two new features are reported at 2914 cm^{-1} and 2950 cm^{-1}. Transients of each of these features are shown in Figure 5.14, and Table 5.3 records the values of bi-exponential fits of the data. The τ_1 lifetimes of the features at 3107 cm^{-1} and 3237 cm^{-1} are within error of those previously reported for diamonds rich in B-nitrogen centres in Sections 3.3 and 4.3. Their long τ_2 lifetimes indicate that these states also take part in the trapping of free carriers.

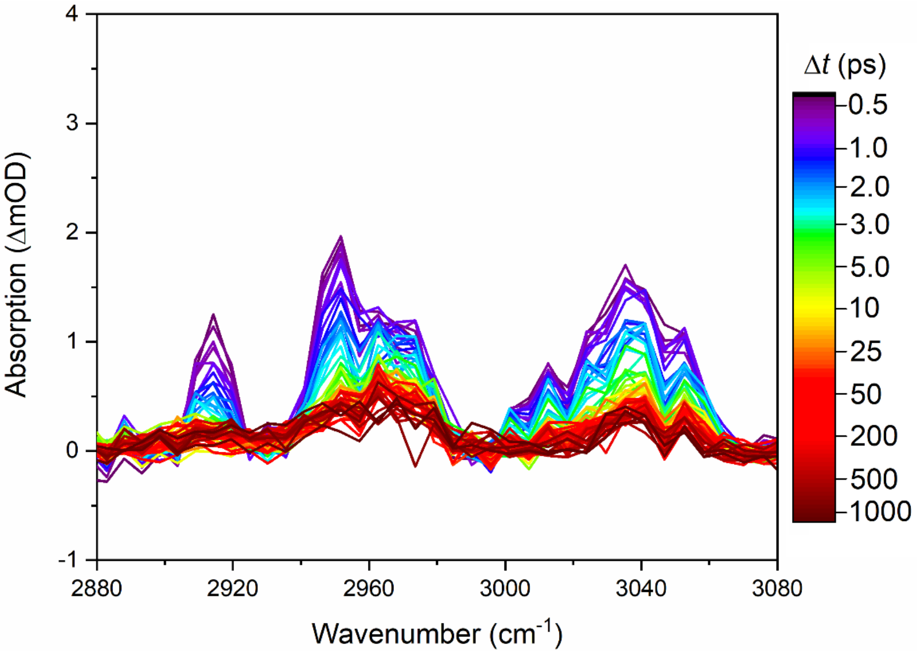

Figure 5.13 TVAS results for diamond sample N2, after subtraction of the broad absorption background, without the use of a smoothing filter. Transient absorption spectra for pump-probe delays 0 ps $< \Delta t <$ 1000 ps, for pump excitation centred at 240 nm and probed in the region around 2900-3100 cm^{-1}.

Both of these features display a fast relaxation and a complete decay at short lifetimes. Here, the entire signal decays after 30 ps, in contrast to the other features that persevere at times >1000 ps. Whilst the feature at 2950 cm^{-1} does not appear to undergo complete decay from our measurements, this is because it is sitting atop the ESA for the C–H stretch mode of N_3VH^0, which does not decay completely here.

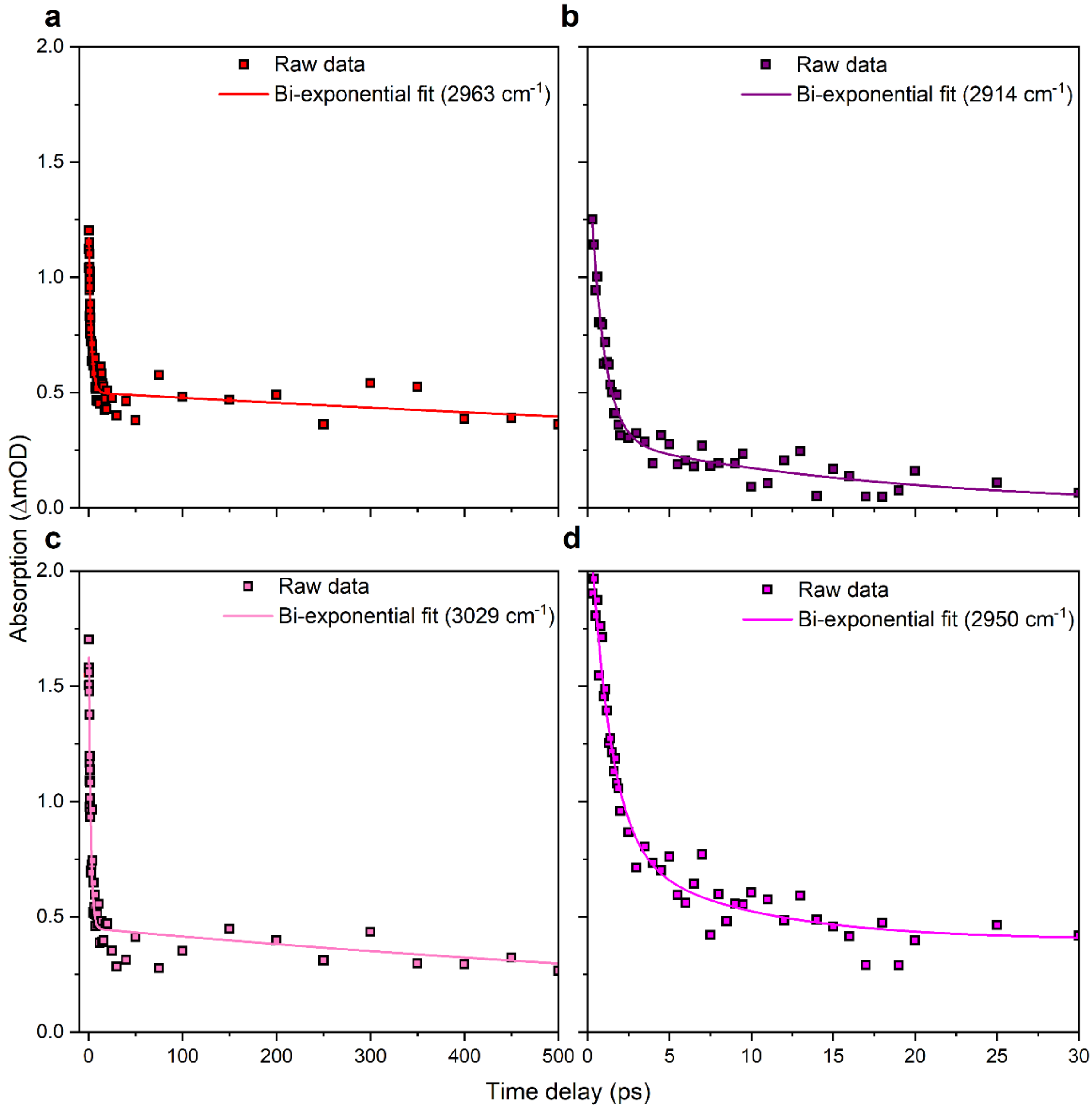

Figure 5.14 TVAS for natural diamond N2, using unfiltered data. **a,** Absorption difference at 2963 cm^{-1} (red squares), measured at the wavenumber of their peak maxima, and a bi-exponential fit (solid line). **b,** Absorption difference at 2914 cm^{-1} (purple squares), measured at the wavenumber of their peak maxima, and a bi-exponential fit (solid line). **c,** Absorption difference at 3029 cm^{-1} (peach squares), measured at the wavenumber of their peak maxima, and a bi-exponential fit (solid line). **d,** Absorption difference at 2950 cm^{-1} (pink squares), measured at the wavenumber of their peak maxima, and a bi-exponential fit (solid line).

Table 5.3 Decay lifetimes from transient fits of unfiltered data in the range 3100-3300 cm^{-1} from N2, at a temperature of 298 K. All errors are standard errors, scaled by the square root of the reduced chi-squared value.

$\boldsymbol{\omega}(\mathbf{cm^{-1}})$	A_1	$\boldsymbol{\tau_1}(\mathbf{ps})$	A_2	$\boldsymbol{\tau_2}(\mathbf{ps})$
2914	0.9 (± 0.1)	0.8 (± 0.1)	0.3 (± 0.1)	18.1 (± 4.4)
2950	1.3 (± 0.1)	1.3 (± 0.2)	0.4 (± 0.2)	14.9 (± 4.5)
2963	0.6 (± 0.1)	2.7 (± 0.3)	0.5 (± 0.1)	2100 (± 800)
3029	1.2 (± 0.1)	2.0 (± 0.2)	0.5 (± 0.2)	1200 (± 500)

Due to the similarity in wavenumber of these two features to the ESA at 2963 cm^{-1}, we speculate that they arise due to the excitation of a combination mode to a level where it includes an additional excited stretch mode. One strong possibility is the transition $v_{2S+B} \leftarrow v_{S+2B}$, as the wavenumber difference between the feature at 2950 cm^{-1} and v_{2S} = 2963 cm^{-1} is 13 cm^{-1}, which closely matches the difference of 17 cm^{-1} between v_S = 3107 cm^{-1} and the 3090 cm^{-1} transition from $v_{S+2B} \leftarrow v_{2B}$. Other possibilities for this feature, or for the 2914 cm^{-1} feature, are the transitions $v_{2S+B} \leftarrow v_{S+B}$ or $v_{S+3B} \leftarrow v_{3B}$. Peaks corresponding to the transitions from the ground state to v_{2S+B}, v_{2S+2B} and v_{S+3B} have not been observed in FTIR spectra, likely due to the intensity of these absorptions being sufficiently low that they exist below the noise floor. Thus, a firm assignment of these two transitions at 2914 cm^{-1} and 2950 cm^{-1} is not possible.

5.4 Conclusions and future work

This work has expanded upon past work involving the UV excitation of diamond and its defects. The effect of the presence of defect states on the relaxation of free carriers is demonstrated, with the longer relaxation time in high defect concentration diamonds explained by the trapping of these free carriers in defect states existing inside the diamond band gap. Additionally, we have investigated the behaviour of specific defect sites when under electronic excitation. A relaxation lifetime for the electronically excited C–H stretch mode at 3107 cm^{-1} was determined to be ~1.3 ps. For the analogous stretch mode at 3237 cm^{-1}, a relaxation lifetime of ~1.4 ps was determined. Additionally, a slower relaxation component in both cases could be attributed to relaxation from modes that had experienced vibrational excitation in addition to electronic, these modes being limited by the time required for relaxation to their vibrational ground state. Finally, several features are observed in the region 2880-3080 cm^{-1}. Whilst these features cannot be given specific assignments, they do indicate relaxation from the electronically excited state occurs into the higher vibrational states of the electronic ground state.

There is great potential for expansion on the work presented in this chapter. High-resolution TVAS measurements on more known features belonging to both defects, such as those found at 1405 cm^{-1}, 2787 cm^{-1}, 4169 cm^{-1} and 4703 cm^{-1}, could shed more light on the mechanisms for both electronic and vibrational relaxation taking place. Additionally, a more conclusive assignment of the features at 2915 cm^{-1} and 2950 cm^{-1} could be achieved through two different ways: (1) UV pump – IR probe TVAS experiments on diamond samples that do not include the feature at 3237 cm^{-1}, to ensure that the two features can be attributed with certainty to the N_3VH^0 defect; (2) IR pump – IR probe TVAS experiments, pumping population into v_B, v_{2B},

v_{3B} or v_{S+2B}, and subsequently probing around 2800-3100 cm^{-1} would offer a route to assigning the peaks at 2914 cm^{-1} and 2950 cm^{-1} to specific transitions.

Additionally, moving the IR probe to other regions of the spectrum would enable the identification of other features, potentially including the v3s mode of both defects, which would further quantify their anharmonicity and refine the Morse potential model of the two stretch modes. In particular, the identification of further transitions associated with the 3237 cm^{-1} system would offer more information for future computational models looking to assign a defect complex to it.

5.5 References

1. T. Popelář, F. Trojánek, M. Kozák, P. Malý, *Diam. Relat. Mater.* **2017**, *71*, 13-19.
2. R. Ulbricht, S. T. van der Post, J. P. Goss, P. R. Briddon, R. Jones, R. U. A. Khan, M. Bonn, *Phys. Rev. B*, **2011**, *84*, 165202.
3. R. Ulbricht, S. Dong, A. Gali, S. Meng, Z.-H. Loh, *Phys. Rev. B* **2018**, *97*, 220302.
4. R. Ulbricht, Z.-H. Loh, *Phys. Rev. B* **2018**, *98*, 094309.
5. J. P. Goss, P. R. Briddon, V. Hill, R. Jones, M. J. Rayson, *J. Phys. Condens. Matter* **2014**, *26*, 145801.
6. F. S. Gentile, S. Salustro, M. Causa, A. Erba, P. Carbonniere, R. Dovesi, *Phys. Chem. Chem. Phys.* **2017**, *19*, 22221–22229.
7. R. U. A. Khan, P. M. Martineau, B. L. Cann, M. E. Newton, D. J. Twitchen, *J. Phys. Condens. Matter* **2009**, *21*, 364214.
8. W. Shockley, W. T. Read, *Phys. Rev.* **1952**, *87*, 835–842
9. M. I. Nathan, A. B. Fowler, G. Burns, *Phys. Rev. Lett.* **1963**, *11*, 152-154.
10. R. Le Toullec, N. Piccioli, and J.C. Chervin, *Phys. Rev. B* **1980**, *22*, 6162-6170.

11. T. Webert, H. Stolzt, W. von der Ostent, M. Heukenj, K. Heime, *Semicond. Sci. Technol.* **1995**, *10*, 1113-1116.

12. A. Savitzky, M. J. E. Golay, *Anal. Chem.* **1964**, *36*, 1627–1639.

6 Summary and outlook

Through this work, we have reported our study on the excitation and decay dynamics of local vibrational modes (LVMs) associated with hydrogen in diamond. Specifically, we have looked at the absorption features found at 3107 cm^{-1} and 3237 cm^{-1}, and their responses to both infrared (IR) and ultraviolet (UV) excitation. Table 6.1 summarises the findings in this research by reporting the key differences between the two features in terms of their relaxation dynamics, potential energy surfaces and concentration.

Table 6.1 A summary of the differences between the features at 3107 cm^{-1} and 3237 cm^{-1}.

Property	**3107 cm^{-1} (N_3VH^0)**	**3237 cm^{-1}**
Position of v_{2S}	6070 cm^{-1}	6266 cm^{-1}
Relaxation path	3-level system	2-level system
τ_{GSB}	~6 ps	~1.8 ps or ~3 ps
τ_{ESA}	~3.5 ps	~1.8 ps or ~3 ps
Sample variance of τ	None	Faster relaxation when B-nitrogen centres are present
$2\omega x$	144 cm^{-1}	208 cm^{-1}
Calibration factor (ppb)	$(110 \pm 10) \times I_{3107}(\text{cm}^{-2})$	$(27 \pm 4) \times I_{3237}(\text{cm}^{-2})$
Matrix elements (assuming no directionality)	$\langle\psi_1\|x\|\psi_0\rangle = 0.150$ for $v_S \leftarrow v_0$ $\langle\psi_2\|x\|\psi_1\rangle = 0.215$ for $v_{2S} \leftarrow v_S$	$\langle\psi_1\|x\|\psi_0\rangle = 0.176$ for $v_S \leftarrow v_0$ $\langle\psi_2\|x\|\psi_1\rangle = 0.253$ for $v_{2S} \leftarrow v_S$
UV-induced shift	5 cm^{-1}	4 cm^{-1}

In Chapter 3, we reported our IR pump, IR probe study of the 3107 cm^{-1} stretch mode belonging to N_3VH^0. Our key findings included the position of the first overtone of the stretch mode (6070 cm^{-1}), the excited-state lifetime of the mode (~6 ps), the method of vibrational relaxation (both directly and indirectly via coupling to the bend modes), and an equation calibrating the integrated area of the 3107 cm^{-1} feature in FTIR to the concentration of the N_3VH^0 defect in the diamond. Furthermore, the studies reported in this chapter are the first case of IR pump, IR probe TVAS applied to diamond defects. This work paves the way for analogous studies on other defects to determine similar findings to those reported in the chapter.

In Chapter 4, we repeated our IR pump, IR probe studies, this time on the 3237 cm^{-1} stretch mode which often appears alongside 3107 cm^{-1}, but is not assigned to any particular defect. Our key findings included the position of the first overtone of the stretch mode (6266 cm^{-1}), the variation in excited-state lifetime depending on the diamond type of the sample (~3 ps in IaA, ~1.8 ps in IaB), the method of vibrational relaxation (direct, with no observed coupling to bend modes), and an equation calibrating the integrated area of the 3107 cm^{-1} feature in FTIR to the concentration of its associated defect in diamond. Additionally, this work demonstrates that the IR pump, IR probe studies carried out are applicable to the whole suite of diamond defects that manifest absorption features in the IR.

In Chapter 5, we carried out UV pump, IR probe studies on the 3107 cm^{-1} and 3237 cm^{-1} stretch modes investigated in Chapters 3 and 4. Our key findings included the excited-state lifetimes of the electronically excited stretch modes (~1.3 ps and ~1.4 ps respectively), shifted positions of the stretch modes after electronic excitation (3102 cm^{-1} and 3233 cm^{-1} respectively), and the discovery of additional transitions at 2914 cm^{-1} and 2950 cm^{-1}, associated with further excitation of the stretches of higher combination modes. Additionally, we studied the effect of defect states on the lifetime for free carrier relaxation, reporting a longer lifetime of recombination for a sample containing a high defect concentration (4300 ps) over one of a low defect concentration (1750 ps).

The studies reported in this thesis have opened up the possibility of using ultrafast spectroscopy to carry out comparative measurements on the whole suite of diamond defects that manifest in the IR. It has become possible to use a combined approach of steady-state and ultrafast spectroscopy, together with theoretical simulations, to determine the relaxation dynamics of both vibrational and electronic states of defects in diamond, and the position of their vibrational overtones. This data can then be used to establish the energetic landscape of their LVMs. Additionally, a new approach has been found for the quantification of defects in diamond based on their IR absorption features. In the future, it will be possible to apply this method to other diamond defects with less intense features in the IR, such as NVH^-, which manifests at 3123 cm^{-1}, and $N{:}H\text{-}C^0$, which manifests at 3324 cm^{-1}. NVH^- in particular would be a great candidate for study, as a calibration of its concentration is already in use. As such, it presents an excellent opportunity to further confirm the method applied in this thesis for determination of defect concentration.

With regards to the defects studied in this thesis, further study of samples containing the absorption feature at 3237 cm^{-1} would further establish its potential connection to B-nitrogen centres, whilst IR pump, IR probe studies probing the other absorption features ascribed to these two defects (such as the 1405 cm^{-1} and 2787 cm^{-1} bend modes of N_3VH^0) would improve the picture of the dynamics taking place in both systems. IR excitation into the v_{2S} modes of both defects would allow the $v_{3S} \leftarrow v_{2S}$ transition to be probed directly, solidifying the position of v_{3S}, improving the picture of anharmonicity of both stretch modes, and thus allowing a better model of the Morse potential to be produced. Additionally, future UV pump studies of samples containing only the 3107 cm^{-1} feature would firmly establish which of the higher vibrational overtones are linked to N_3VH^0, and which are linked to other defects.


Transient
Population
Ultrafast
Argyle
Pump
Picosecond
Transmission
Emission
Lifetime
Optical
Dynamics
Probe
Photon
CVD
Lifetime
Feature
Symmetry
Probe
UV/Vis
Voigt
Hydrogen
Excited state
FTIR
TVAS
Time-resolved
Acoustic
Pulse
Quantification
Nitrogen
Laser
Defect
Concentration
Time
Pulse
Transient
Decay
Phonon
Photon
Synthetic
Infrared
Stretch
Phonon
Bend
Transmission
TVAS
Feature
Time
Natural
Absorption
Vibration
Diamond
Wavenumber
Time constant
Dephasing
Symmetry
Ground state
Spectroscopy
Infrared
Stretch
Ultraviolet
Visible
Decay
Pump
Resolution
Defect
Model
Diamond
CVD
Transition
Resolution
Optical
Laser
Vibration
Ground state
CVD
Spectroscopy
Natural
Cryogenic
Bend
Spectrum
FTIR
Argyle
Emission